# Influence of strain on electronic and transport properties of defects in 2D materials

**by Mohammad Bahmani**

University of Bremen

April 2022

# Influence of strain on electronic and transport properties of defects in 2D materials

Thesis presented for the degree of

**Doctor of Philosophy in Physics**
**(Dr. rer. nat.)**

by

**Mohammad Bahmani**

| | |
|---|---|
| First Reviewer: | Prof. Dr. Thomas Frauenheim |
| Second Reviewer: | Dr. Agnieszka Beata Kuc |
| Date of the Colloquium: | 26. April 2023 |

Bremen Center for Computational Materials Science
Department of Physics and Electrical Engineering
University of Bremen

Bremen, April 2022

*Dedicated to*

my most beautiful dream, *Fatemeh*,

my mom, brother, sister,

and the memory of my father and brother.

# Abstract

Theoretical as well as experimental studies have shown potential applications of two-dimensional (2D) materials in various fields of science and technology, for example field-effect transistors (FET), spin- and valleytronics, optoelectronic, topological insulators, and flexible devices. These devices, fabricated from monolayers (MLs) of one or two elements, are inexpensive, inherently flexible, and amenable to industrial scale processing because of emergent growth techniques. Among all 2D materials, transition metal dichalcogenides (TMDs) monolayers are under intense investigations since they offer unprecedented opportunities in tuning electronic, optical, and transport properties through strain, dielectric screening, stacking confinement, photoluminescence, and crystal defects.

Monolayers of Group-6 TMDs form two stable structural configurations, namely a semiconducting phase (H-phase) with a direct bandgap and a semimetallic phase (T-phase). These monolayers can undergo strong elastic deformations, up to about 10%, without any bond breaking. Although, MLs TMDs are highly robust to external mechanical fields, their electronic structure is sensitive to compressive and tensile strain. Besides, intrinsic point defects are always present in their synthetic samples. Hence, it is important to understand both effects on the electronic and optical properties of such monolayers. Moreover, the coexistence of 2H- and 1T-phase of MLs $MoS_2$ have further pushed their strong potential for applications in the next generation of electronic devices based on the 2D lateral heterojunctions. Here, the interfaces of two phases are often imperfect and may contain numerous vacancies, which also have considerable effects on the their properties.

In this work, we investigate the electronic structure, energetic, and optical properties of defective MLs TMDs, subject to various strain situations, using density functional theory (DFT) simulations. Our results indicate that strain leads to strong modifications of the defect levels inside the bandgap, e.g. splitting their degeneracy up to an amount of 450 meV. We show that a type of shear strain lowers the formation energy of all the point defects. According to the outcomes, presence of vacancy complexes leads to absorption with larger dipole matrix elements in comparison to

the case of simple transition metal vacancies.

The other objective of this thesis is to explore the charge transport properties of the 1T/2H-$MoS_2$ heterojunctions in the existence of point defects, by means of non-equilibrium Green function (NEGF) approach. While vacancies in semiconducting $MoS_2$ act as scattering centers, their presence at the interface improves the flow of the charge carriers. The transmission enhancement was explained by changes in the electronic densities at the T-H interfaces, which open new transport channels for electron conduction.

# Declaration

The work in this thesis is based on research carried out at the Bremen Center for Computational Materials Science (BCCMS), the Department of Physics and Electrical Engineering, Bremen University, Bremen, Germany. No part of this thesis has been submitted elsewhere for any other degree or qualification and it is all my own work unless referenced to the contrary in the text.

**Copyright © 2022 by Mohammad Bahmani**.
"The copyright of this thesis rests with the author. No quotations from it should be published without the author's prior written consent and information derived from it should be acknowledged".

# Acknowledgements

I would like to use the this page to thank the numerous people who made this work possible.

First, I would like to thank my supervisor, Prof. Dr. Thomas Frauenheim, for giving me an opportunity to work at the Bremen Center for Computational Material Science (BCCMS) group at the Bremen University. His support is very important for me to accomplish the objectives in this thesis and finish my PhD studies.

My sincere and special thanks to Dr. Michael Lorke, Dr. Mahdi Ghorbani-Asl, and Dr. Agnieszka Beata Kuc, without their help, endless patience and motivation, it was not possible to successfully complete this thesis and publish the results.

I would like to thank Dr. Bálint Aradi, Dr. Christof Köhler, Meisam Farzalipour Tabriz, Mahdi Faghihnasiri, Prof. Dr. Peter Deák, Prof. Dr. Tim Wehling, and Dr. Gabriele Penazzi, for many great scientific and technical discussions. I also wish to express my sincere thanks to Sandra Smit, our wonderful secretary at the BCCMS, who has always answered my thousand questions about the life in germany and the local regulations as well as helped me with PhD-related paperwork.

Here is the place to send my appreciation to Dr. Miguel Pruneda, Prof. Dr. Pablo Ordejón, Dr. Nick Papior, for vast and informative discussion about functionality and capabilities of SIESTA and TranSIESTA.

I am grateful to all my friends in Bremen, my colleagues at BCCMS, and people who have helped me out during my doctoral studies.

And lastly, but most importantly, I want to thank my family and in particular my beloved wife and best friend, Fatemeh, for her love, support and encouragement, which defines me as a scientist and as a person. Thank you for taking care of me

all the time.

Furthermore, financial support from the German Academic Exchange Service (DAAD) and PiP Program at the Physics and Electrical Engineering Department of the Bremen University, is greatly acknowledged.

# Contents

**Abstract** v

**Declaration** vii

**Acknowledgements** viii

**Contents** x

**Contents** x

**List of Abbreviations** xi

**List of Publications** xiii

**List of Conference Contributions** xiv

**List of Figures** xvi

**List of Figures** xvi

**List of Tables** xvii

**List of tables** xvii

**1 Introduction** 1

1.1 2D Materials . . . . . . . . . . . . . . . . . . . . 1

1.2 Transition Metal Dichalcogenides . . . . . . . . . . . . . . . . 2

1.3 Synthesis and Defects in TMDs . . . . . . . . . . . . . . . . 5

1.4 Strain: Importance & Techniques to Induce . . . . . . . . . . 7
1.5 Outline of Thesis . . . . . . . . . . . . . . . . . . . . 9

**2 Theory and Methods 12**

2.1 Density Functional Theory . . . . . . . . . . . . . . . . 12
2.1.1 The generic quantum mechanical problem . . . . . . . . 13
2.1.2 Hohenberg and Kohn Theorems . . . . . . . . . . . . 15
2.1.3 Kohn-Sham equations . . . . . . . . . . . . . . . . 16
2.1.4 Exchange-Correlation functionals . . . . . . . . . . . 17
2.1.5 SIESTA: Localized basis set . . . . . . . . . . . . . 19
2.2 Quantum Theory of Electron Transport . . . . . . . . . . . . 22
2.2.1 Landauer-Büttiker formalism . . . . . . . . . . . . . 23
2.2.2 NEGF techniques: TranSIESTA . . . . . . . . . . . . 26
2.2.3 Self-energies of the semi-infinite electrodes . . . . . . . . 29
2.2.4 Transmission and conductance . . . . . . . . . . . . 32
2.3 Mechanical Deformations . . . . . . . . . . . . . . . . . 33
2.4 Formation Energy Calculation . . . . . . . . . . . . . . . 34

**3 $MoS_2$ Monolayers Subject to Mechanical Deformations 37**

3.1 Computational Details . . . . . . . . . . . . . . . . . . 38
3.2 $MoS_2$ unitcell: Bulk & Monolayer . . . . . . . . . . . . . . 39
3.3 Monolayer of $MoS_2$ with Vacancies . . . . . . . . . . . . . 43
3.3.1 Energy of formation . . . . . . . . . . . . . . . . . 45
3.3.2 Defect levels: Position and orbital characteristics . . . . . 47
3.4 Strain Engineering of the Properties . . . . . . . . . . . . . 48
3.4.1 Energetics . . . . . . . . . . . . . . . . . . . . . 49
3.4.2 Electronics: Sulfur vacancies . . . . . . . . . . . . . 50
3.4.3 Electronics: $V_{Mo}$ and vacancy complexes . . . . . . . . . 53
3.5 Conclusions . . . . . . . . . . . . . . . . . . . . . . 56

**4 Optical Response from Defective TMDs under Strain 58**

4.1 Computational Details . . . . . . . . . . . . . . . . . . 59

4.2 Electronic Structure . . . . . . . . . . . . . . . . . . . . . 63

4.3 Optical Properties . . . . . . . . . . . . . . . . . . . . . 64

4.4 Conclusions . . . . . . . . . . . . . . . . . . . . . 72

**5 Devices Based on 2D Lateral Heterojunctions 74**

5.1 Computational Details . . . . . . . . . . . . . . . . . . . . . 76

5.2 1T-2H Interface . . . . . . . . . . . . . . . . . . . . . 77

5.3 Schematic of 1T/2H-$MoS_2$ Devices . . . . . . . . . . . . . 79

5.4 Transport Through Lateral Heterojunctions . . . . . . . . . . 82

5.4.1 Sulfur vacancies . . . . . . . . . . . . . . . . . . . 82

5.4.2 Molybdenum vacancies and vacancy complexes . . . . . 84

5.4.3 Antisites . . . . . . . . . . . . . . . . . . . 86

5.5 Conclusions . . . . . . . . . . . . . . . . . . . . . 89

**6 Concluding Remarks 92**

6.1 Summary . . . . . . . . . . . . . . . . . . . . . 92

6.2 Outlook . . . . . . . . . . . . . . . . . . . . . 94

**Appendix 132**

**A Defective $MoS_2$ Monolayers under strain 132**

A.1 $V_S$ vacancy . . . . . . . . . . . . . . . . . . . . . 132

A.2 Orbital Characteristics . . . . . . . . . . . . . . . . . . . . . 133

A.3 Geometry modifications for MLs $MoS_2$ with $V_{Mo}$ . . . . . . . . 137

A.4 $V_{Mo+3S}$ and $V_{Mo+6S}$ vacancies . . . . . . . . . . . . . . . 138

A.5 Input parameters for the self-generated pseudopotentials . . . . 139

**B 1T/2H $MoS_2$ Based Lateral Heterojunctions 141**

B.1 Structure of the devices containing point defects . . . . . . . . 142

B.2 Vector Current - $V_{Mo}$ . . . . . . . . . . . . . . . . . . 143

B.3 Local Density of States (LDOS) projected on atoms and orbitals . 144

B.4 Calculated BandGap vs. other methods . . . . . . . . . . . . 145

B.5 Projected Local Density of States (PLDOS) . . . . . . . . . . 146

# List of Abbreviations

**2D:** Two-Dimensional

**3D:** Three-Dimensional

**TMDs:** Transition Metal Dichalcogenides

**FETs:** Field-Effect Transistors

**PL:** Photoluminescence

**MLs:** Monolayers

**CVD:** Chemical Vapor Deposition

**AFM** Atomic Force Microscope

**DFT:** Density Functional Theory

**NEGF:** Non-Equilibrium Green's Functions

**LDOS:** local density of states

**PLDOS** Projected Local Density of States

**LDA:** Local Density Approximation

**GGA:** Generalized Gradient Approximation

**PBE:** Perdew Burke Ernzerhof

**SIESTA:** Spanish Initiative for Electronic Simulations with Thousands of Atoms

**LCAO:** linear Combination of Localized Atomic Orbitals

**GFs:** Green's Functions

**DLs:** Defect Levels

**PBC:** Periodic Boundary Conditions

**DZP:** Double $\zeta$ Polarized

**CG:** Conjugate Gradients

**BZ:** Brillouin Zone

**SOC:** Spin-Orbit Coupling

**SCF:** Self-Consistent Field

**VBM:** Valence Band Maximum

**CBM:** Conduction Band Minimum

**LEDs:** Light-Emitting Diodes

**MEMS:** Microelectromechanical Systems

**DDTs:** Defect-Defect Transitions

# List of Publications

**Published in peer-reviewed journals**

- M. Bahmani, M. Faghihnasiri, M. Lorke, A. B. Kuc, T. Frauenheim, *"Electronic Properties of Defective $MoS_2$ Monolayers Subject to Mechanical Deformations: A FirstPrinciples Approach*", Phys. Status Solidi B, 2020, 1900541, DOI: 10.1002/pssb.201900541
- M. Bahmani, M. Lorke, M. Faghihnasiri, T. Frauenheim, *"Reversible tuning the optical properties of defective TMDs monolayers"*, Phys. Status Solidi B, 2021, 2000524, DOI: 10.1002/pssb.202000524
- M. Bahmani, M. Ghorbani-Asl, T. Frauenheim, *"Effect of Interfacial Defects on the Electronic Properties of $MoS_2$ Based Lateral T-H Heterophase Junctions"*, RSC Adv., 2021, 11, 37995-38002, DOI: 10.1039/D1RA06010D

# List of Conference Contributions

1. Poster: *"Optics and Electronics of ML $MoS_2$ with Point Defects under Strain"*
   M. Bahmani, M. Lorke, M. Faghihnasiri, T. Frauenheim,
   CECAM Workshop: "Correlated electron physics beyond the Hubbard model",
   Bremen, Germany (2019)

2. Poster: *"Optics and Electronics of ML $MoS_2$ with Point Defects under Strain"*
   M. Bahmani, M. Lorke, M. Faghihnasiri, T. Frauenheim,
   CECAM Workshop: "Thinking outside of the box - beyond machine learning for quantum chemistry", Bremen, Germany (2019)

3. Poster: *"Supercell of single-layer $MoS_2$ with point Defects under strain"*
   M. Bahmani, M. Faghihnasiri, T. Frauenheim,
   Flatlands beyond graphene, Leipzig, Germany (2018)

4. Poster: *"Strain on $MoS_2$ Sheets with Defects from First Principles"*
   M. Bahmani, M. Faghihnasiri, T. Frauenheim,
   CAMD Summer School: "Electronic Structure Theory and Materials Design",
   Helsingr, Denmark (2018)

5. Poster: *"Strain on $MoS_2$ Sheets with Defects from First Principles"*
   M. Bahmani, M. Faghihnasiri, T. Frauenheim,
   CECAM Workshop: "Crystal defects for qubits, single photon emitters and nanosensors", Bremen, Germany (2018)

6. Poster: *"Strain on $MoS_2$ Sheets with Defects from First Principles"*
   M. Bahmani, M. Faghihnasiri, T. Frauenheim,

CECAM Workshop: "Reliable and quantitative prediction of defect properties in Ga-based semiconductors", Bremen, Germany (2018)

7. Poster: *"Strain on $MoS_2$ Sheets with Defects from First Principles"*
   M. Bahmani, M. Faghihnasiri, T. Frauenheim,
   Proceedings of the 7th International Conference on Nanostructures (ICNS7)
   27 Feb - 1 Mar 2018, Tehran, Iran

8. Talk: *"Strain on molybdenum disulfide sheets with defects from first principles"*
   M. Bahmani, M. Faghihnasiri, T. Frauenheim,
   DPG Spring Meeting of the Condensed Matter Section (SKM) together with the EPS, Berlin, Germany (2018)

9. Talk: *"Continually tuning the band gap of monolayer $MoS_2$ via mechanical strain"*
   M. Bahmani, M. Faghihnasiri, T. Frauenheim,
   DPG Spring Meeting of the Condensed Matter Section (SKM) together with the EPS, Berlin, Germany (2018)

# List of Figures


1.1 TMDs in periodic table . . . . . . . . . . . . . . . . . . . 2

1.2 Schematic representation of the atomic structure of TMDs. . . . 3

1.3 Different phases of TMDs crystals. . . . . . . . . . . . . . 5

2.1 Schematic representation of a typical system when studying atomic scale transport problems . . . . . . . . . . . . . . . . . 22

2.2 Schematic representation of electron transport in ballistic and diffusive regimes . . . . . . . . . . . . . . . . . . . . . . . 23

2.3 Schematic representation of conductance through an one-dimensional sample connected to reservoirs and illustration of the corresponding transport channels . . . . . . . . . . . . . . . . . . 24

2.4 Schematic representation of strain situations used in the present work. 33

3.1 Band structure and orbital characteristics of bulk $MoS_2$. . . . . 41

3.2 Band structure and orbital characteristics of monolayer $MoS_2$. . . 42

3.3 The change in the band gap of pristine MLs $MoS_2$ under various strain cases. . . . . . . . . . . . . . . . . . . . . . . . 43

3.4 Geometries of MLs $MoS_2$ with point vacancies and vacancy complexes 44

3.5 Displacement maps of atoms in the MLs $MoS_2$ surrounding the defects 45

3.6 Calculated formation energies of different sulfur- and molybdenum-based vacancies in MLs $MoS_2$ . . . . . . . . . . . . . . 46

3.7 Calculated band structures of the MLs $MoS_2$ with sulfur vacancies . 47

3.8 Calculated band structures of the MLs $MoS_2$ with molybdenum vacancies . . . . . . . . . . . . . . . . . . . . . . . . 48

3.9 The evolution of the formation energy of point defects in L $MoS_2$ as function of four different strain. . . . . . . . . . . . . . . . . 50
3.10 Evolution of the DLs of the MLs $MoS_2$ with $V_{2S-top}$ defects under various compression and tension . . . . . . . . . . . . . . . 51
3.11 Evolution of the DLs of the MLs $MoS_2$ with $V_{2S-par}$ defects under various compression and tension . . . . . . . . . . . . . . . 51
3.12 Evolution of the DLs of the MLs $MoS_2$ with $V_{Mo}$ defects under various compression and tension. . . . . . . . . . . . . . . . . . . 54
3.13 The change in the charge density of the MLs $MoS_2$ with $V_{Mo}$ under compressive and tensile strain in Y-direction. . . . . . . . . . . 56

4.1 A monolayer of $MoS_2$ ($WSe_2$) containing vacancy complexes . . . 61
4.2 Schematic view of various uniaxial strain types . . . . . . . . 62
4.3 Schematic of the electronic structure of the defective MLs $MoS_2$ (MLs $WSe_2$) 64
4.4 The absorption spectra for MLs $MoS_2$ with $V_{Mo}$ under various compression and tension . . . . . . . . . . . . . . . . . . . . . . 65
4.5 The change in the charge density of the $MoS_2$ monolayers containing $V_{Mo}$ under strain . . . . . . . . . . . . . . . . . . . . . . . 67
4.6 The absorption spectra for MLs $WSe_2$ with $V_W$ under various compression and tension . . . . . . . . . . . . . . . . . . . . . . 68
4.7 The absorption spectra for MLs $MoS_2$ with $V_{Mo+3S}$ under various compression and tension . . . . . . . . . . . . . . . . . . . 70
4.8 The absorption spectra for MLs $WSe_2$ with $V_{W+3Se}$ under various compression and tension . . . . . . . . . . . . . . . . . . . 71

5.1 Band structures are plotted for Semiconductor (2H) and metallic (1T) phases of $MoS_2$ monolayers. . . . . . . . . . . . . . . . . . . 78
5.2 Schematic of a device based on metallic (1T) and Semiconductor (2H) phases of $MoS_2$ monolayers. . . . . . . . . . . . . . . . . . . 79
5.3 Schematic of the T-H heterophase junction of $MoS_2$ monolayer with and without defects. . . . . . . . . . . . . . . . . . . . . . . 80

5.4 Displacement map of the defective structures. Sum of displacements in the three axis are calculated. . . . . . . . . . . . . . . . . 81
5.5 LDOS at the left interface for devices without defects (Perfect) and with sulfur vacancies at two Biases . . . . . . . . . . . . . 83
5.6 Transmission spectra are plotted for T-H heterophase junction of $MoS_2$ monolayer containing various sulfur vacancies at both interfaces 84
5.7 LDOS at the left interface for devices without defects (Perfect) and with molybdenum vacancies at two Biases . . . . . . . . . . 86
5.8 Transmission spectra and IV curves are plotted for T-H heterophase junction of $MoS_2$ monolayer containing molybdenum vacancy, $V_{Mo}$, and vacancy complexes . . . . . . . . . . . . . . . . . . . 87
5.9 Difference in the conductance through perfect systems and device with $V_{Mo}$ as function of the device's area at different bias voltages . 88
5.10 LDOS at the left interface for devices without defects (Perfect) and with substitutions at two Biases . . . . . . . . . . . . . . . 88
5.11 Transmission spectra and IV curves are plotted for T-H heterophase junction of $MoS_2$ monolayer containing various substitutions . . . 90

A.1 Evolution of the band edges along with the DLs of the $MoS_2$ ML with $V_S$ under various strain situations. . . . . . . . . . . . . . . 133
A.2 Orbital characteristics of unoccupied deep DLs of $V_S$ in ML $MoS_2$ at zero strain and as function of various compression and stretching. . 134
A.3 Orbital characteristics of unoccupied deep DLs of $V_{2S-top}$ in Ml $MoS_2$ at zero strain and as function of various compression and stretching. 135
A.4 Orbital characteristics of unoccupied deep DLs of $V_{2S-par}$ in Ml $MoS_2$ at zero strain and as function of various compression and stretching. 136
A.5 Orbital characteristics of unoccupied deep DLs of $V_{Mo}$ in Ml $MoS_2$ at zero strain and as function of various compression and stretching. . 137
A.6 The change in the position of the atoms surrounding $V_{Mo}$ in ML $MoS_2$, as different strain are applied. . . . . . . . . . . . . . . . 138

A.7 Evolution of the band edges along with the DLs of ML $MoS_2$ with $V_{Mo+3S}$ under various strain types. . . . . . . . . . . . . . . . 139
A.8 Evolution of the band edges along with the DLs of ML $MoS_2$ with $V_{Mo+6S}$ under various strain types. . . . . . . . . . . . . . . . 139

B.1 Schematic of the device based on metallic (1T) and Semiconductor (2H) phases of $MoS_2$ monolayers and the defect positions at the interfaces. . . . . . . . . . . . . . . . . . . . . . . . . 142
B.2 Vector currents for devices with perfect interfaces and where $V_{Mo}$ are present at both interfaces. . . . . . . . . . . . . . . . . . . . 143
B.3 Density of States projected on atoms and orbitals for devices containing $V_{2S-par}$, $V_{Mo}$, and $2S - top_{Mo}$ at both interfaces. . . . . . . . 144
B.4 Projected Local Density of States for devices with perfect interfaces and where $V_{Mo}$ are present at both interfaces. . . . . . . . . . 146

# List of Tables

3.1 Calculated and experimental lattice parameters for monolayer and bulk $MoS_2$. . . . . . . . . . . . . . . . . . . . . . 40

B.1 Band gaps of 2H-$MoS_2$ monolayer calculated at different levels of theory 145

# Chapter 1

# Introduction

## 1.1 2D Materials

Two-dimensional (2D) materials are a set of layered materials with weak Van der Waals interactions between layers, which exhibit novel properties and applications, different from their bulk counterparts [1–3]. The intrinsic high surface to volume ratio, due to their heights of a few atoms, endows them to be a potential basis for surface-related applications including supercapacitors, catalysis, sensors and opto-electronics [4–7]. Since their electronic structure ranges from semimetallic to semi-conductors and finally to insulators, they present a promising landscape of materials as building blocks to manufacture various electronic and optoelectronic devices [1,3,8,9]. Besides, the thickness of these single-layers is in the range of atomic length and the in-plane covalent bonds are strong, which in turn, leads to optical transparency, excellent mechanical strength, and flexibility [10,11]. Since the electrons are restricted to move in such ultrathin region, in particular for single-layers, this confinement facilitates the compelling electronic properties of these 2D materials [12,13]. As a result, they are ideal for the fundamental study in condensed matter physics as well as electronic and optoelectronic devices [1,9,10,14,15]. Besides, several solution-based techniques, i.e. spin coating, inkjet printing, drop casting, vacuum filtration, spray-and coating, have been developed to fabricate freestanding ultrathin 2D materials with high-quality, which make them even more interesting

for practical applications [15, 16]. The last but not the least, this high exposure of surface atoms allows for manipulation of the properties by means of element doping, dielectric screening, photoluminescence, surface functionalization, and above all defect, strain, and phase engineering [2,3,13,17,18]. All in all, more than ten years after the experimental demonstration of graphene in 2004, studying fundamental physical phenomena and the development of effective device architectures are now pushing 2D materials rapidly toward novel technological applications in the next-generation devices [1, 2, 8, 9]. Ever since, many other 2D materials have been synthesized, such as transition metal-dichalcogenides (TMDs), hexagonal boron-nitride (h-BN), and black phosphorous or phosphorene [1–3, 19].

## 1.2 Transition Metal Dichalcogenides

In the structure of TMDs, metal atoms (M) mostly comes from group IV, V, and VI, while chalcogen atoms (X) are namely S, Se, and Te (see Figure 1.1). Following the

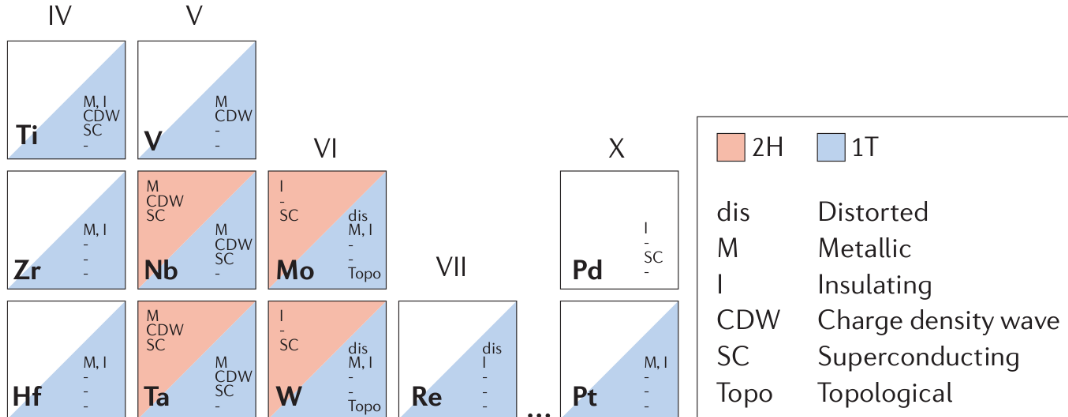


Figure 1.1: (Color online) Part of the periodic table with known layered TMDs is shown [20]. Their structural and electronic phases are also summarized.

synthesis of the molybdenum disulfide ($MoS_2$) monolayer (ML), the first top-gated field-effect transistor (FET) based on 2D materials was built [21–23]. Thenceforth, single-layers of Group-6 transition metal dichalcogenides have become the subject of many investigations as a productive ground for harvesting fundamental science and emergent applications [3, 4, 7, 17]. Bulk structure contains infinite layers stacking

on top of each other and held by Van der Waals forces. This family of materials, with the general chemical formula of $MX_2$, are constructed of a triple $X$–$M$–$X$ layer, where the transition metal, $M$ (i.e. Mo,W,Ta,Nb,Ni), is covalently bonded to six chalcogen atoms, $X$ (i.e. S,Se,Te). The schematic representation of the bulk crystal, and monolayer structure as well as their lattice paramters are shown in Figure 1.2 [20, 24, 25]. In the bulk structure, $c$ is the layer–layer distance. The

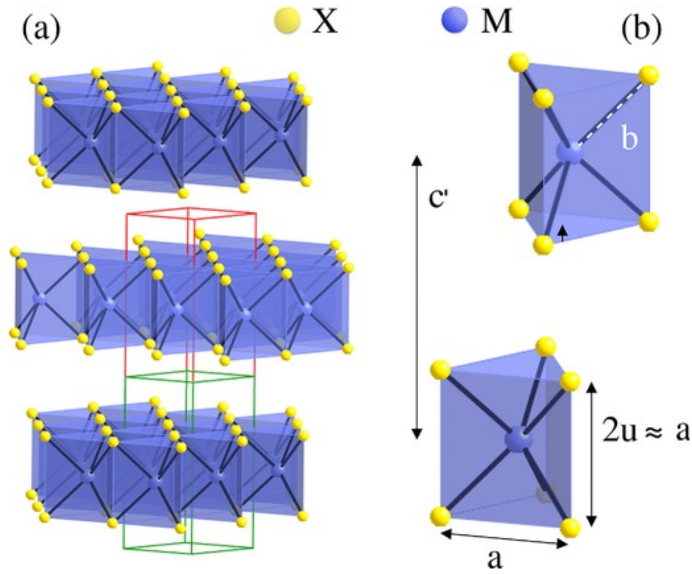


Figure 1.2: (Color online) a) Schematic of the atomic structure of $MX_2$ is shown. Two layers of $MX_2$ per unit cell, each being built up from a trigonal prism co-ordination unit, make the bulk compound. The unit cell of a $MX_2$ monolayer is represented with the small green rectangle. Doubling this layer, it is extended (red rectangle) to the bulk crystal. (b) The trigonal prisms for the two layers in the bulk compound are shown in details as well as the lattice constants and the definition of the structural angles [25].

distance between in-plane nearest neighbors, i.e. $M$–$M$ and $X$–$X$, is denoted with $a$. $b$ is the distance between $M$ and $X$ in a unitcell and the distance between the $M$ and $X$ planes is labeled by $u$. The measured $b$ and $u$ for the $MX_2$ are very close to the $\sqrt{7/12}a$ and $a/2$, respectively, which are the ideal values for a perfect trigonal prism structure [25–27].

Consider these four TMDs compounds: $MoS_2$, molybdenum diselenide ($MoSe_2$), tungsten disulfide ($WS_2$), and tungsten diselenide ($WSe_2$), two of which will be studied in this thesis. Semiconducting 2D TMDs have direct band gaps of typi-

cally from 1 to 2 $eV$ [25, 28]. Hybridization of the $d_{xy}$, $d_{x^2-y^2}$, and $d_{z^2}$ orbitals of the transition metals $M$, and all the $P$ orbitals of the chalcogen atoms $X$ form the orbital characteristics of the valance and the conduction bands. One of the unique features of the such semiconductors is that their band structure undergoes an indirect-direct bandgap transition, when the layers are reduced from bulk structure to a single-layer [3, 21]. This tunable bandgap in 2D TMDs when combined with a strong photoluminescence (PL) and large exciton binding energy, make them highly promising for application in a variety of optoelectronic devices, such as photodetectors, photo-transistors, light-emitting diodes, and solar cells [6, 11, 29, 30]. Further features of such monolayers (MLs) are broad range of mobility, high on/off ratio, and extreme thinness which allows more efficient control over switching and help to reduce short-channel effects and power dissipations [29, 30].

Beside this semiconducting 2H phase with hexagonal symmetry, some members of the TMDs are observed to form a metastable crystal polytype with semimetalic properties [18,31–33]. This is called the 1T phase and have octahedral geometry with the tetragonal symmetry. Figure 1.3 shows the structure of these two phases as well as a high-resolution transmission electron microscope image of their atomically thin boundary [34, 35]. Hence, depending on the arrangement of the chalcogen atoms, monolayer TMDs appear in many distinct phases. For example, 2H phase of $MoS_2$ can be transformed to the metallic structure by gliding one of the $S$ planes to the center of the hexagonal rings [31, 33]. Techniques such as electron-beam irradiation [36], annealing [37], applying strain [31, 38], or electron doping [39, 40], can trigger the reversible transition from 2H to 1T phase in $MoS_2$ crystal. The coexistence of the semiconducting and semimetalic phases of $MoS_2$ has also been observed and characterized [32–34, 41–43]. Such bi-phase homogeneous hybrid systems has paved the way for the application of the in-plane metal–semiconductor heterostructures in the new generation 2D electronic devices [34, 41–43]. In fact, sub-10 nm channel-length transistors were fabricated using semiconducting and metallic phases of MoS2 [43]. Based on the edges between 1T and 1H phases, different interfaces can be arranged, i.e. armchair and zigzag [33, 44, 45]. It was reported that the armchair

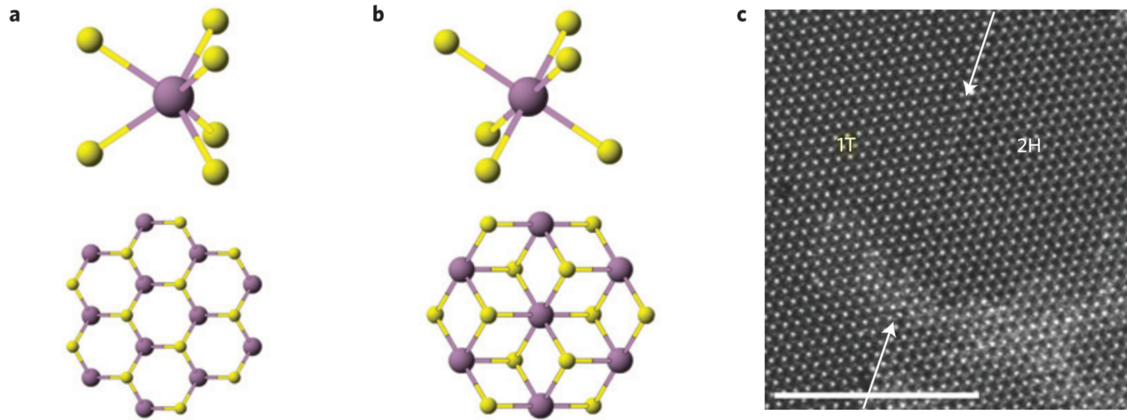


Figure 1.3: (Color online) a,b) Crystal structure of the 2H and 1T phases of TMDs monolayers are shown respectively. The trigonal prismatic (a) and octahedral (b) coordinates are represented in the upper diagram. In the lower panel, the top (c-axis) view of the corresponding MLs TMDs are displayed. The atom colors are similar to Fig. 1.2, namely purple for metals and yellow for chalcogens. (c) High-resolution transmission electron microscope image of their interface (indicated with arrows) for the case of $MoS_2$ monolayers [34].

interfaces are most stable against buckling [33,45]. Besides, connecting the armchair edges of 1T and 1H phases are energetically more favorable than zigzag interfaces [33, 44]. In another study, the conductivity of the armchair edges have been found to be higher than that of the zigzag interfaces which stems from the presence of the metallic Mo zigzag chains along the transport direction [45]. Therefore, armchair interfaces are used in the present study to construct phase-engineered devices of $MoS_2$ monolayers. Their electronic and transport properties are further studied as point defects are present in the semiconducting region.

## 1.3 Synthesis and Defects in TMDs

Developing conventional and novel applications based on the atomically thin 2D TMDs rely on the quality and scalability of their production as well as the ability to control the synthesis processes [3, 24, 46–49]. High quality single crystal samples, with efficient electronic behavior and suitable for fundamental characterization, can be produced using the mechanical exfoliation. [3, 22, 50, 51]. Nonetheless, systematic

control of thickness and size of nanosheets is vety challenging or even unfeasible in the mechanical exfoliation approach. On the other hand, Solution-based exfoliation techniques allow synthesizing large quantity of the 2D materials as well as composite and hybrid structures [15, 16, 52]. Moreover, freestanding ultrathin TMDs can be fabricated via such liquid-phase preparations of the monolayers, i.e. spin coating, inkjet printing, drop casting, vacuum filtration, spray-and coating, making them even more interesting for practical applications [15, 16]. In terms of scalability, however, the exfoliation approaches perform inadequately. Direct synthesis techniques, e.g. epitaxial growth, physical, metalorganic, and in particular chemical vapor deposition (CVD), can be used for large-scale fabrication of the 2D materials [48,49,53–56]. The crystal quality and uniformity of the samples synthesized via the CVD method is a drawback of the technique which can be improved through adjusting its parameters [48, 57, 58].

As a result of thermal equilibrium and the kinetics of processing, all the synthetic samples contain structural defects which showed significant effects on their electrical, optical, vibrational, magnetic, and chemical properties [17,59–67]. Moreover, structural defects and impurities can be introduced deliberately, e.g., at the post growth stage, by chemical and plasma treatment [68–71], vacuum annealing [60, 72–74], ion bombardment [47, 60, 75–77], or electron irradiation [12, 61, 78–80].

These defects have advantages and disadvantages based on the desired application. For example, depending on the concentration of the defects, performance of $MoS_2$-based FETs may differ by several orders of magnitude [23, 55, 81]. In another study, the presence of sulfur vacancy in MLs $WS_2$ induces mid-gap states into their band structure which, in turn, leads to an absorption in the near infrared wavelength region [82].

On the other hand, some studies imply that the vacancy creation can extend the application of $MoS_2$ nanosheets [47, 83–86], e.g., as single-photon emitters, due to localized states of the isolated defects [47, 85]. In a recent study, molybdenum (Mo) vacancies were generated site-selectively to write optically active defect states in MLs TMDs [47]. The mid-gap localized levels have also been observed to improve the

photoresponsivity of $MoS_2$ monolayers by trapping the photo-excited charge carriers, leading to a growth of the photocurrent in photodetectors [87–89]. Furthermore, intrinsic defects such as S and Mo vacancies, may improve the contact resistance and the carrier transport efficiency of devices depending on the electrode's elements [65, 90–93]. It has been shown that active sites for hydrogen adsorbtion onto the MLs $MoS_2$ can be introduced when vacancies are present inside the nanosheets [94, 95]. This increases the hydrogen evolution reaction on these defective surfaces, hence, improving their catalytic properties.

## 1.4 Strain: Importance & Techniques to Induce

Semiconducting 2D materials exhibit high resilience towards mechanical deformations in comparison to the conventional three-dimensional (3D) semiconductors [50, 96, 97]. While, for example, silicon tends to crack under 1.5% tensile strain, $MoS_2$ MLs can withstand about 10% tensile strain [98, 99]. This capability is attributed to the lack of dangling bonds and their high crystallinity, allowing for a high degree of flexibility [50, 97]. However, the electronic structure of the 2D materials, in particular TMDs monolayers, is very sensitive to the applied strain [100]. In the case of MLs $MoS_2$, about 1.5% uniaxial tensile strain results in the direct-to-indirect bandgap transition, while at around $10 - 15\%$ of biaxial tensile strain the structure undergoes a semiconductor-to-metal transition [99, 100]. As a large biaxial strain is applied to $MoS_2$ monolayer, its bandgap can be reversibly and continuously tuned up to 500 meV [101]. Integrating onto microelectromechanical systems (MEMS), strain of more than 1.3% has been applied to MLs $MoS_2$, which lays the ground for novel applications of 2D TMDs in flexible LEDs and field-effect transistors (FETs) [102]. Thus, mechanical deformations offer rapid and reversible tuning of the bandgaps in 2D TMDs of Group-6. This also offers a controllable way to modify the electronic and optoelectronic properties of semiconducting 2D materials. These strain-engineered properties lead to new potential applications for MLs TMDs, such as piezoelectricity in $MoS_2$, broad-spectrum solar energy funnel, and flexible transparent phototransistors [10, 11, 16, 103, 104]. It was also observed

that biaxial strain can tune the properties of photodetector devices based on $MoS_2$ monolayers [11].

Different techniques have been proposed in experimental setups to apply mechanical deformations to the 2D materials [50, 99, 105–112]. Atomically thin semiconductors can be synthesized on top of a substrate which has a different thermal expansion coefficient. Such thermal expansion mismatch can be used to induce uniform biaxial tensile strains by varying the temperature of the sample [105]. With some modifications to this method, even more complex straining patterns can also be applied [106]. Homogeneous biaxial and uniaxial strains can be applied by growing a piezoelectric material underneath the monolayers as substrate [107]. This allows for a control compressing or stretching the structure via simply changing the applied voltage to the piezoelectric material. Another approach to apply homogeneous deformations is to deposite the 2D materials on top of flexible substrates [108, 109]. Bending the substrate, the tensile strain is transformed to the monolayers via the topmost surface of the substrate. The slippage is a drawback in the application of this technique which can be resolved by the metal strips as clamping points, having been evaporated onto the monolayers [108]. Elongating an elastic substrate can also be used to apply uniaxial strains to the samples [110].

To apply the inhomogeneous deformations, the 2D materials can be transferred onto elastomeric substrates to simulate the phenomena known as buckling-induced rippling or wrinkling [111, 112]. Besides, researchers have investigated the stiffness and breaking strength of monolayers via nanoindentation experiments [50, 96]. In this method, the tip of an atomic force microscope (AFM) is used to apply very large strains, up to the breaking point, onto the freely suspended monolayers. Such extreme deformations revealed the particular mechanical properties of the 2D materials, which is close to those predicted for the ideal brittle materials [50, 113]. As the breaking stress value for 2D $MoS_2$ has been measured, it showed an amount up to 1/8 of the Young's modulus, getting closer to the ideal value of 1/9 [50, 96, 113, 114]. In an ideal structure, the intrinsic strength of the atomic bonds is presumed to be mainly responsible for the fracture point, while the presence of defects has negligible

effects.

## 1.5 Outline of Thesis

The essential objective of this project is to investigate the strain and defect engineering of the electronic and optical properties of the 2D materials, particularly MLs TMDs. We also see how the presence of crystalline defects at the interface of lateral heterojunctions modifies the transport properties of phase-engineered 2D devices. The exploitation of these phenomena may allow building blocks for novel applications. This thesis is organized as follows.

Chapter 2 covers an introduction to the Hohenberg and Kohn theorems and the approximations required to derive the density functional theory (DFT). A brief overview of the applied approximations as well as the exchange and correlation functionals used in this thesis is also given. A short description of the SIESTA method is provided. Then, the quantum theory of the electron transport within the framework of the non-equilibrium Green's function (NEGF) is presented along with the formula to compute the transmissions and I-V curves. The types of strain studied in this project is also explained. In the last section of this chapter, the formalism and approach to calculate the formation energies are introduced.

In Chapter 3, the pristine TMDs monolayers is investigated and the results from the method of choice are validated against the previous studies. Then, the electronic and energetic properties of the $MoS_2$ monolayers containing point vacancies are scrutinized. These defects have been observed in experiments and can be introduced via the post-growth techniques in a control process. Furthermore, different properties of the defective 2D structures are investigated subject to the mechanical deformations. The modifications of the localized defect states under strain are explained via analyzing the characteristics of the orbitals involved in those states.

Following the method in the last chapter, in chapter 4, we further analyze the optical properties of $MoS_2$ and $WSe_2$ monolayers, containing metal vacancies and vacancy complexes, as function of applied strain. Here, absorption spectra are computed within the linear response regime. These findings are of great interest in

understanding and expanding the potential applications of MLs TMDs in optoelectronic and flexible devices. Besides, they provide a hypothesis that in ion-irradiation processes, single photons are emitted from vacancy complexes rather than simple transition metal vacancies. The analyses in this part of the thesis are based on the orbital characteristics as well as the outcomes of the previous chapter.

In chapter 5, the coexistence of semiconducting (2H phase) and metallic (1T phase) phases of $MoS_2$ monolayers is studied. This would help with pushing their strong potential for applications in the next generation of electronic devices based on the 2D lateral heterojunctions. In particular, the role of interfacial defects on the electrical properties of such devices are investigated. The first-principles simulations and NEGF techniques are used to compute the local density of states (LDOS), transmission curves, and IV characteristics of perfect and defective devices under a various range of bias.

Finally, chapter 6 brings together a comprehensive overview of the outcomes of the conducted research and concludes the remarks presented in the last three chapters. An outlook to further expand the present studies are also provided.

# Chapter 2

# Theory and Methods

With the objective to explore the physics and chemistry of various materials, e.g. atoms, molecules, and condensed structures, an effective approach is proposed as electronic structure calculations. To study the quantum mechanical description of electrons in such materials, without introducing system-dependent parameters, an accurate computational scheme is presented via ab-initio methods, namely the mean-field theory: density functional theory [27, 115]. In this chapter, the fundamental concepts and theoretical methodology for the electronic structure calculations in the present study are briefly introduced. We will present the details of the basic underlying techniques used throughout this thesis in Section 2.1. Then, given the theory of quantum transport, a brief overview of the non-equilibrium Green function techniques will be presented in Section 2.2.

## 2.1 Density Functional Theory

As of the past several decades, the production of ever more complex computer codes and an enormous increase in the computational resources have equipped the physicists with the DFT codes as a common approach to scrutinize complex systems. A more detailed introduction to the method, important aspects of the condensed matter theory, available extensions to the DFT, and exact mathematical formulations can be found in literature [27, 115–117]. As a parameter free method and predic-

tive capabilities, the DFT is one the most frequently used methods to describe the ground states of complex physical systems in a wide variety of environments.

### 2.1.1 The generic quantum mechanical problem

When using quantum mechanics to study the materials, the general purpose is to find the solution of the time independent Schrdinger equation

$$\mathbf{H}\Psi(\mathbf{r},\mathbf{R}) = E\Psi(\mathbf{r},\mathbf{R}). \tag{2.1.1}$$

Here $\Psi$ is the time-independent many-electron wave function for interacting electrons, in which $\mathbf{r} = \{r_1, r_2, ...\}$ and $\mathbf{R} = \{R_1, R_2, ...\}$ are electron and nuclei positions, respectively. Omitting relativistic effects, the Hamiltonian $\mathbf{H}$ for such system is written as a sum of terms originating from different levels of interaction,

$$\mathbf{H} = \mathbf{T}_e + \mathbf{T}_n + \mathbf{V}_{n-n} + \mathbf{V}_{e-e} + \mathbf{V}_{e-n} \tag{2.1.2}$$

where subscript $e$ and $n$ denotes electron and nuclei, respectively. Thus, kinetic energies of $\mathbf{T}_e$ and $\mathbf{T}_n$ are the contributions from electrons and nuclei, respectively. The other terms are the pairwise interaction between the particles as nuclei-nuclei interaction $\mathbf{V}_{n-n}$, electron-electron interaction $\mathbf{V}_{e-e}$, electron-nuclei interaction $\mathbf{V}_{e-n}$. These terms can be written as

$$\begin{gathered}
\mathbf{T}_e = -\sum_i^{N_e} \frac{\hbar^2}{2m_i}\nabla_i \quad ; \quad \mathbf{T}_n = -\sum_\alpha^{N_n} \frac{\hbar^2}{2m_\alpha}\nabla_\alpha \\
\mathbf{V}_{n-n} = -\frac{1}{2}\sum_\alpha^{N_n}\sum_\beta^{N_n} \frac{e^2}{|\mathbf{R}_\alpha - \mathbf{R}_\beta|} \quad ; \quad \mathbf{V}_{e-n} = -\frac{1}{2}\sum_i^{N_e}\sum_\alpha^{N_n} \frac{e^2}{|\mathbf{r}_i - \mathbf{R}_\beta|} \\
\mathbf{V}_{e-e} = -\frac{1}{2}\sum_i^{N_e}\sum_j^{N_e} \frac{e^2}{|\mathbf{r}_i - \mathbf{r}_j|}
\end{gathered} \tag{2.1.3}$$

with $i$, $j$ denoting electronic indices and $\alpha$, $\beta$ nuclei indices. In order to remove the double counting terms in the potentials expansions, the 1/2 is added. Since the number of electrons and nuclei, $N_e$ and $N_n$, in a material is very large, it is common

practice to use an adiabatic approximation proposed by Born and Oppenheimer [117]. In this scheme, the electron and nuclei dynamics are considered decoupled due to their large mass difference so that electrons see the atoms in a static configuration and move within a translational invariant static nuclei potential. This allows us to separate the complex wavefunction of the system to two parts, the electronic wavefunction $\psi(\mathbf{r}, \mathbf{R})$ and the lattice wavefunction $\chi(\mathbf{R})$, as

$$\Psi(\mathbf{r}, \mathbf{R}) = \psi(\mathbf{r}, \mathbf{R})\chi(\mathbf{R}). \tag{2.1.4}$$

Note that $\psi$ is still a function of the atomic coordinates as a result of the environment [1]. As a result, the Schrdinger equation for electrons can be written as

$$\mathbf{H}_e\psi(\mathbf{r}, \mathbf{R}) = E\psi(\mathbf{r}, \mathbf{R}), \tag{2.1.5}$$

with the below electronic Hamiltonian

$$\mathbf{H}_e = \mathbf{T}_e + \mathbf{V}_{e-e} + \mathbf{V}_{e-n}. \tag{2.1.6}$$

Several theories have been proposed to solve this multi-variate equations, such as the Hartree method which describes the many-electron wavefucntions as a product of one-electron orbitals, while in the Hartree-Fock approach, these wavefunctions are extended to a Slater determinant of spin orbitals [118, 119]. However, all the electronic variables, including spatial and spin, are interacting in the system, leading to drastic raises in the computational complexity with exponential scaling to the number of atoms.

Addressing the problem from a different perspective, density functional theory is formulated based on a simpler variable, the electron density rather than the exact wavefunctions, as the name implies. One benefit of this approach lay on the fact that the density only depends on three variables.

[1] In principle, $\chi$ also depends on the electronic positions, $\mathbf{r}$, however, this explicit dependency can be omitted in an adiabatic approximation with an average density of electrons.

### 2.1.2 Hohenberg and Kohn Theorems

In 1964, Hohenberg and Kohn proposed the initial theorems of DFT [120], and formulated them with two statements:

> ***Theorem 1:*** *The external potential is a unique functional of the electron density, $\rho(\mathbf{r})$, in the ground state, and therefore the total energy is also a functional of the ground state electron density, $E[\rho(\mathbf{r})]$.*
>
> ***Theorem 2:*** *Given a system with the electronic density, the ground state energy, $E_0$, corresponds to the global minimum of the total energy functional, and the density $\rho_0(\mathbf{r})$, which minimize $E[\rho(\mathbf{r})]$, is the exact ground state density.*

Accordingly, the wavefunction $\psi$ and thus all the properties of a given system at its ground state are determined by the electron density, $\rho(\mathbf{r})$. The associated total energy as a function of this trial density can be written as

$$E[\rho(\mathbf{r})] = F[\rho(\mathbf{r})] + V_{ext}(\mathbf{r}), \tag{2.1.7}$$

with $V_{ext}(\mathbf{r})$ as the external potential and $F[\rho(\mathbf{r})]$ describing an unknown, but a universal functional defined via $\rho(\mathbf{r})$. Hence, the external potential and the number of electrons are sufficient to define the Hamiltonian. In the rest of this thesis, $\rho(\mathbf{r})$ is replaced by $\rho$, unless otherwise stated. The universal functional is written as

$$F[\rho] = T[\rho] + E_{ee}[\rho] \tag{2.1.8}$$

where $T[\rho]$ is the kinetic energy functional and $E_{ee}[\rho]$ is the electron-electron interaction energy. The $E_{ee}[\rho]$ is usually split up to two terms, $E_H[\rho]$ being classical Coulomb (Hartree) energy and a non-classical part denoted as $E_Q[\rho]$. Finally, to formulate the second theorem, the total energy evaluated at an arbitrary density $\rho$ is larger than the the ground state energy obtained at the ground state density $\rho_0$, more intuitively

$$E[\rho] > E[\rho_0]. \tag{2.1.9}$$

### 2.1.3 Kohn-Sham equations

Although the Hohenberg and Kohn theorems have undoubtedly simplified the problem at hand, it is not clear what is the proper expression for the functional $F[\rho]$ as well as how to find the ground state density. In order to overcome such drawbacks, Kohn and Sham suggested to replace the interacting system with an auxiliary non-interacting reference system [121]. Thereupon, rewriting the universal functional, the relation for the Kohn-Sham total energy is reformed as

$$E_{KS}[\rho] = T_0[\rho] + V_{ext}(\mathbf{r}) + E_H[\rho] + E_{XC}[\rho]. \tag{2.1.10}$$

Here, $T_0[\rho]$ is the kinetic energy of the single-particle system and given by

$$T_0[\rho] = -\frac{\hbar^2}{2m_e}\sum_{i=1}^{N_e}\int d\mathbf{r}|\nabla\psi_i|^2, \tag{2.1.11}$$

where $\psi_i$ is the single-particle wavefunctions of the non-interacting system, known as Kohn-Sham orbitals. It should be noted that regardless of the throughout usage, their physical interpretation has been debated [122]. The third term, $E_H[\rho]$, is a classical term describing the Coulomb repulsion, called the Hartree energy

$$E_H[\rho] = \frac{1}{2}\int d^3\mathbf{r}d^3\mathbf{r}'\frac{\rho\rho'}{|\mathbf{r}-\mathbf{r}'|}, \tag{2.1.12}$$

and the exchange-correlation functional $E_{XC}[\rho]$, containing the many-body effects contributions to the kinetic and potential energies, thus all exchange and correlation energies, can be expanded as

$$E_{XC}[\rho] = T[\rho] - T_0[\rho] + E_{ee}[\rho] - E_H[\rho]. \tag{2.1.13}$$

To fulfill the condition in Eq. (2.1.9) and thus find the ground state density, we rely on the variation principle under the constraint of constant particle number $N_e$. Consequently, the Euler-Lagrange formalism is applied to minimize the Kohn-Sham total energy. This enables us to write down the Kohn-Sham equations which are

the one-electron Schrdinger equations for an effective potential $V_{eff}$ written as

$$\left[-\frac{1}{2}\nabla^2 + V_{eff}\right]\psi_i = \varepsilon_i\psi_i, \qquad (2.1.14)$$

with the effective potential having terms corresponding to the Hartree, external potential, and the exchange-correlation energies. It is obvious from these set of equations that the Kohn-Sham equations is a set of closed equations where the effective potential is a function of density which itself is calculated from $\psi_i$. Hence, an iterative approach is needed to solve them. An extended description of the DFT methodology can be found in the literature [27, 115, 123].

It should be pointed out that all the unknown variables in Eq. (2.1.1) is now moved to a single unknown in Eq. (2.1.14), the exchange-correlation functional. Thus, if we had known the exact form of the exchange-correlation functional was known, the exact many-body ground state energy and density could be found by solving the independent particle system. There has been on-going attempts to find the true form of this functional [124]. However, it is still possible to make approximations, each having their own weaknesses and strengths (see Section 2.1.4) [115, 116].

### 2.1.4 Exchange-Correlation functionals

We have realized that the performance of the DFT method significantly depends on the choice of the exchange-correlation functional. Over the years several approximations to the functionals have been suggested. Among them, there are two widely used approximations, the local density approximation (LDA) and the generalized gradient approximation (GGA) [121, 125, 126].

In the LDA a completely local exchange-correlation potential is assumed so that the electrons of a given system are treated as an homogeneous electron gas

$$E_{XC}^{LDA}[\rho] = \int d^3\mathbf{r}\varepsilon_{XC}^{hom}[\rho], \qquad (2.1.15)$$

where $\varepsilon_{XC}^{hom}$ is the exchange-correlation energy per electron inside the homogeneous gas. It can be divided into the exchange part $\varepsilon_X^{hom}$ is known analytically and given

by the Dirac exchange formula for the homogeneous electron gas [127]

$$\varepsilon_X^{hom} = -\frac{3e^2}{4\pi}(3\pi^2\rho)^{1/3}, \tag{2.1.16}$$

and correlation part $\varepsilon_C^{hom}$ which is not easy to drive. In practice, the interpolated expressions for the $\varepsilon_C^{hom}$ is provided fitting to Quantum Monte-Carlo methods [125,128,129]. The LDA suffers from a major deficiency, namely self-interaction, which leads to overestimation of the cohesive properties, thus giving too small lattice constants and bond lengths. As a result, this assumption of a uniform electron density, not being the case for most atomic and molecular systems, causes underestimation of the exchange energy while the correlation energy is overestimated [130].

These shortcomings stimulated efforts to develop the GGA method which is a considerable improvement upon every aspect of the LDA, but not the self-interaction error. Here, the electron density as well as its gradient are taken into account to better describe varying electron densities [129, 131–133]. Hence, this semi-local exchange-correlation potential has the following general form

$$E_{XC}^{GGA}[\rho, \nabla\rho] = \int d^3\mathbf{r}\rho\varepsilon_{XC}^{hom}[\rho, \nabla\rho]. \tag{2.1.17}$$

To name a few of the numerous proposed formulations of $E_{XC}^{GGA}$, there are PW91 [129], LYP [133], B88 [132] and in particular PBE [126], named after Perdew, Burke and Ernzerhof, which is commonly used in solid-state physics. The cohesive and structural properties of solids and molecules have been described with good accuracy, proving the reliability of the results produced via the PBE functional. Due to the fact that throughout this thesis, the exchange and correlation interactions are described by the PBE functional within the GGA approximation, a more detailed explanation of this functional is presented. Within the GGA approximation, the exchange and the correlation parts are separated, just as in LDA. On this account, the exchange part in PBE has the following form

$$E_X^{PBE}[\rho, \nabla\rho] = \int d^3\mathbf{r}\rho\varepsilon_X^{LDA}[\rho]F_X^{PBE}[s], \tag{2.1.18}$$

where the PBE exchange enhancement factor $F_X^{PBE}[s]$ can be written as

$$F_X^{PBE}[s] = 1 + \kappa - \frac{\kappa}{1 + \frac{\mu s^2}{\kappa}}, \tag{2.1.19}$$

with $s = |\nabla\rho|/2k_F\rho$ being a dimensionless gradient term, Fermi k-point $k_F$, $\kappa = 0.804$, and $\mu = 0.219$. The correlation part reads

$$E_C^{PBE}[\rho_\uparrow, \rho_\downarrow] = \int d^3\mathbf{r}\rho \left[\varepsilon_C^{hom}(\mathbf{r}_s, \zeta) + H(\mathbf{r}_s, \zeta, t)\right], \tag{2.1.20}$$

where $\rho_{\uparrow/\downarrow}$ is the density of the electrons with up/down spin. The term $\varepsilon_C^{hom}$ is the correlation of the homogeneous electron gas, $\mathbf{r}_s = (k_F/\pi)(4/9)^{(1/3)}$ is the local Seitz radius, $\zeta = (\rho_\uparrow - \rho_\downarrow)/\rho$ the relative spin polarization, and $t = |\nabla\rho|/(2gk_s\rho)$ is a dimensionless gradient term. The analytical expression for H is chosen as

$$H = \frac{e^2}{a_0}\gamma\Phi^3 ln\left[1 + \frac{\beta}{\gamma}t^2\left(\frac{1 + At^2}{1 + At^2 + A^2t^4}\right)\right] \tag{2.1.21}$$

with

$$A(r_s, \zeta) = \frac{\beta}{\gamma}\frac{1}{e^{\varepsilon_C^{hom}/\gamma\Phi^3} - 1}\ ,\ \Phi(\zeta) = \frac{1}{2}\left[(1+\zeta)^{2/3} + (1-\zeta)^{2/3}\right]\ ,\ \gamma = \frac{1 - ln(2)}{\pi^2}.$$

### 2.1.5 SIESTA: Localized basis set

SIESTA (Spanish Initiative for Electronic Simulations with Thousands of Atoms), being both a method and its computer program implementation, solves the Kohn-Sham equations 2.1.14 among many other DFT codes [134]. Here, a short introduction of the method is outlined. The underlying methodology are described in details in the original paper as well as the code's manual on the development website [134, 135].

The core electrons are treated as an effective potential using norm-conserving pseudopotentials so that the basis set only contains the valence electrons. Replacing the core electrons by their effective potentials is a common approach in numerous popular DFT codes [136–140]. As a consequence, the computational and storage requirements are drastically scaled down. A linear combination of localized atomic

orbitals (LCAO) is used to construct the basis set

$$\phi_{\alpha lmn}(\mathbf{r}) = \phi_{\alpha ln}(\mathbf{r} - \mathbf{r}_\alpha) Y_{lm}\left(\frac{\mathbf{r} - \mathbf{r}_\alpha}{|\mathbf{r} - \mathbf{r}_\alpha|}\right), \tag{2.1.22}$$

with $\alpha$ being an atomic index. $l$ and $m$ are the angular momentum index. $n$ is the multiple basis index for orbitals with dissimilar radial dependency while their angular momentums are the same. These identical orbitals are referred to as multiple-$\zeta$ basis functions[2]. The corresponding spherical harmonics $Y_{lm}$ is a collection of orthogonal polynomials. The free atoms in vacuum demands the choice of the basis orbitals which are confined on the atom with a decaying tail into the vacuum. Accordingly, the range of the atomic orbitals are limited via such natural decay and the overlap between the atomic orbitals. This results in the creation of a sparse Hamiltonian with non-zero elements only at the overlap sites. The sparse Hamiltonian makes it possible to perform a natural partitioning of the elements and also order-N calculations due to the fast internal data structures of a sparse matrix. In addition, the use of the LCAO orbitals offers several ways to control the accuracy by means of enlarging the orbitals radius, adding further $\zeta$ orbitals, for the same angular momentum with differing radial dependence, or include the deformation induced by bond formation via adding the polarization orbitals to the expansion of the Kohn-Sham orbitals. Seeing from other way around, the accuracy does not depend on a simple parameter rather a multitude of parameters making the choice of the LCAO orbitals for the basis set a complex problem.

Due to the fact that the LCAO orbitals is a non-orthogonal basis set, the overlap matrix is non-zero

$$\mathbf{S}_{\mu\nu} =< \phi_\nu | \phi_\mu > . \tag{2.1.23}$$

The complex indices for the $\phi$ orbitals have been replaced by single Greek letters for simplicity. The dual basis of the basis orbitals is defined via such overlap matrix as $|\phi^\nu >= |\phi_\mu > \mathbf{S}^{-1}_{\mu\nu}$, so that $< \phi^\nu | \phi_\mu >= \delta^\nu_\mu$ and the overlap matrix is Hermitian.

[2]The multiple-$\zeta$ basis functions are called as single-$\zeta$, double-$\zeta$, etc.

Following up, the expansion of the Kohn-Sham orbitals in terms of atomic orbitals can be written as

$$\psi_i(\mathbf{r}) = \sum_{\mu} \phi_\mu(\mathbf{r}) c_{\mu i}, \tag{2.1.24}$$

$$c_{\mu i} =< \phi^\mu|\psi_i >= \mathbf{S}^{-1}_{\mu\nu} < \phi_\mu|\psi_i > . \tag{2.1.25}$$

Here the coefficients $c_{\nu i}$ are the generalized eigenvector of $\mathbf{H}$ and $\mathbf{S}$ in the non-orthogonal Kohn-Sham eigenvalue problem

$$\sum_{\nu} \mathbf{H}_{\mu\nu} c_{\nu i} = \varepsilon_i \sum_{\nu} \mathbf{S}_{\mu\nu} c_{\nu i}. \tag{2.1.26}$$

The calculation of the density accordingly changes slightly

$$\rho = f_i \sum_i |\psi_i(\mathbf{r})|^2 = f_i \sum_i \sum_{\nu\mu} c^\star_{\nu i} \phi^\star_\nu(\mathbf{r}) \phi_\mu(\mathbf{r}) c_{\mu i}, \tag{2.1.27}$$

$$\int d\mathbf{r}\rho = N = f_i \sum_i \sum_{\nu\mu} c^\star_{\nu i} \mathbf{S}_{\nu\mu} c_{\mu i}, \tag{2.1.28}$$

from which the density matrix is defined as

$$\rho_{\nu\mu} \equiv f_i \sum_i c^\star_{\nu i} c_{\mu i}, \tag{2.1.29}$$

leading to the matrix expression of the density integral Eq. 2.1.28 written as

$$\int d\mathbf{r}\rho = N = Tr[\rho\mathbf{S}]. \tag{2.1.30}$$

In these equations, $f_i$ is the distribution normalized factor so that the total density is equal to $N$. Seen in the Eq. 2.1.30, the density matrix is also a sparse matrix for the reason that the only remaining elements in the density matrix are those corresponding to the non-zero elements in the sparse overlap matrix. From the indexed density of the atomic orbitals, it is possible to obtain the Mulliken populations, conveniently dividing the charge amongst atoms, [141]. The fully assignment of the charges to the explicit atoms is generally challenging. There are many ways

to divide the atomic charges proposed by various schemes [142, 143].

## 2.2 Quantum Theory of Electron Transport

The need to a complete quantum mechanical description of electronic transport has been imposed by the new paradigm in the state-of-the-art technology of nanoelectronics. When modeling the atomic scale devices, it is essential to introduce terms like wave functions and transmission probabilities to the treatment. Figure 2.1 displays the schematic representation of a typical system, which we call it *"device"*, when studying atomic scale transport problems. It is constructed of a central (active) region connected to left and right electrodes. The channel is a material with a gap in the electronic structure. The metallic electrodes allow for charge carriers to flow from reservoirs through the device.

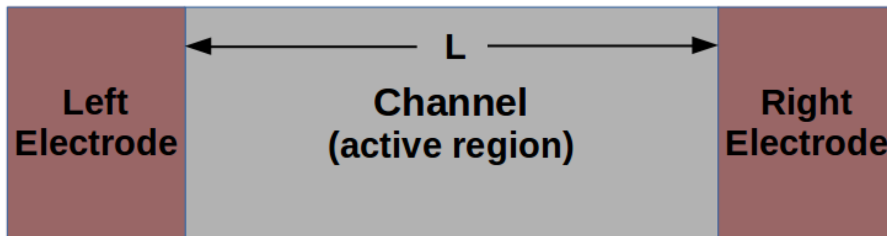


Figure 2.1: (Color online) Schematic representation of a typical system when studying atomic scale transport problems.

At this point, three important characteristic lengths have to be introduced to better follow the discussion of the electronic transport in such materials; 1) the de Broglie wavelength of an electron at the Fermi energy, called the Fermi wavelength $\lambda_F$, 2) the average distance pawed by an electron while maintaining its initial phase, called phase-relaxation length $L_\phi$, and 3) the distance an electron travels until its initial momentum is destroyed, called mean free path $L_m$. The electron-electron or the electron-phonon interactions, inelastic scattering mechanisms, can reduce the $L_\phi$. Besides, the mean free path is limited by the scattering effects originated from impurities and disorders in the crystal. All being said, there are two distinguished regimes of the electronic transport, named *Ballistic* and *Diffusive* transport. as

shown in Fig. 2.2. In the ballistic regime, the mean free path of electrons $L_m$ is

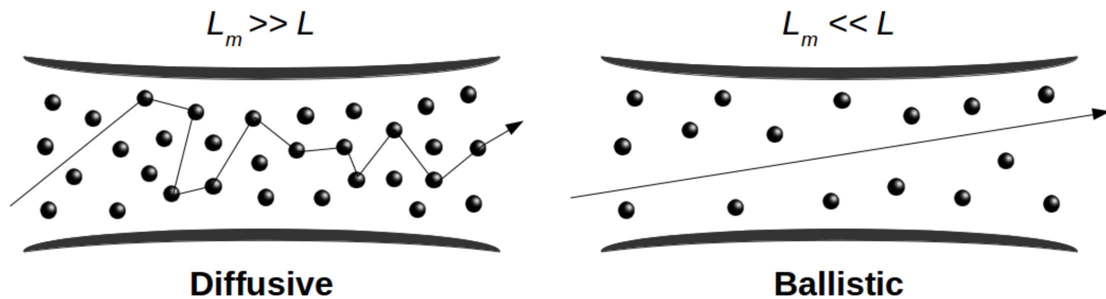


Figure 2.2: Schematic representation of electron transport in **left)** ballistic and **right)** diffusive regimes.

larger than the length of the channel $L$ (see Fig. 2.1), sometimes also called the active region, meaning the electrons move thorough this region without losing their energy. The transport is in the second regime when the $L_m$ is much smaller than the channel length, so that the scattering centers lead to elastic interactions with the electrons within their path.

In this thesis, the inelastic scattering effects, e.g. electron-phonon interactions are neglected. We also assume that the length of the active channel is less than the phase-breaking mean free path ($L_\phi$). Thus, the coherent quantum transport mechanisms are described via the Landauer-Büttiker formalism [144, 145].

## 2.2.1 Landauer-Büttiker formalism

As of the efforts to include the quantum effects in studying the transport properties of the mesoscopic electronic devices, Landauer proposed an approach to address the electrical conductivity through such nanostructure systems [144]. Here, the conductance of the device is associated with the quantum mechanical probabilities of the one-electron wavefunction passing through an arbitrary scattering medium. In this formalism, the temperature is considered low so that the phonons are not the main source of scattering. Moreover, the electrode are at the thermal equilibrium but can be at different electrochemical potentials $\mu_i$, where $i$ is the electrode's number. The motion of the electrons injected from reservoirs are only scattered in the channel

region, while dissipation processes can only take place in the electrodes. A schematic of such process is shown in Figure 2.3(a). The incoming wavefunctions enter a

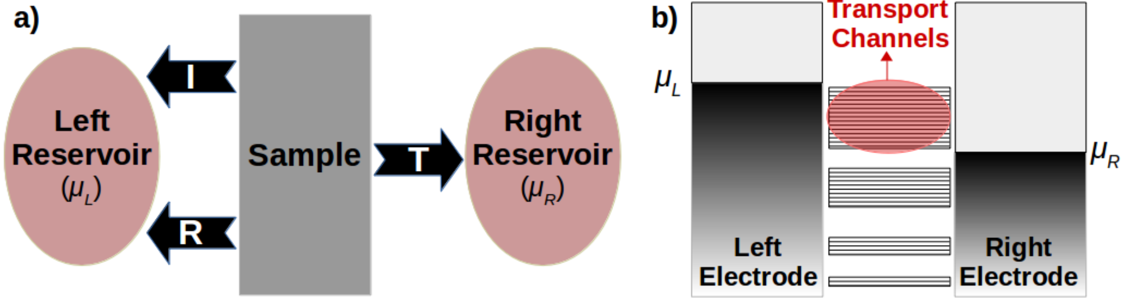


Figure 2.3: (Color online) **(a)** Schematic representation of conductance through an one-dimensional sample connected to reservoirs. **(b)** Illustration of the available transport channels between the left and right electrodes with electrochemical potentials of $\mu_L$ and $\mu_R$, respectively.

mesoscopic conductor (scattering channel) from an electrode, called source, and exits into the other electrode, called drain.

As we presume a steady state, flow of charge carriers from source and drain into the channel is limited to the electrochemical potentials of electrodes. In addition, the propagated wavefunctions from one electrode into the device is never backscattered to itself. We now assume a 1D conductor as the device with two electrodes, in which the states in the left and right contact have positive and negative wavevectors, $k < 0$ and $k > 0$, respectively. The Fermi distribution of $f_L(E,T)$ and $f_R(E,T)$ are used to represent the available states for electrons in the left (L) and right (R) electrodes

$$f_{L/R}(E,T) = \frac{1}{e^{E-\mu_{L/R}/k_B T} + 1}, \tag{2.2.1}$$

with $\mu_L$ and $\mu_R$ being their chemical potentials. The net current in such device with a channel of length $l$, can be written as

$$I = I_L - I_R = \frac{e}{l} \sum_{n,k} V(k) \left[ f_L(E,T) - f_R(E,T) \right], \tag{2.2.2}$$

where $n$ is the number of electrons flowing into the channel and $T$ is the temperature. The group velocity is formulated as $V(k) = \partial E / \hbar \partial k$ with $\hbar$ being the Planck constant divided by $2\pi$. In a solid with a large number of states, the wave vector space

is continuum so that $\sum_k$ is transformed into the integral $l/2\pi \int dk$ [26]. Including the spin degree of freedom (multiply by 2 for spin-up and spin-down channels), the total current takes the form of

$$I = \frac{2e}{h} \sum_n \int_{-\infty}^{+\infty} \frac{\partial E}{\partial k} \left[ f_L(E,T) - f_R(E,T) \right]. \tag{2.2.3}$$

Due to the electron confinement in the transverse direction (perpendicular to the transport direction), charge carriers can move inside specific energy levels, called sub-bands, corresponding to the transport channels which are shown in Figure 2.3(b). Hence, the contribution to the current only comes from the electrons with energies within the bias window, meaning

$$I = \frac{2e}{h} \int_{\mu_L}^{\mu_R} dE \left[ f_L(E,T) - f_R(E,T) \right] T(E), \tag{2.2.4}$$

where the electrons flowing through all the transport channels participate in the total current. Here, $T(E)$ represents the transmission probability of the electrons with energy $E$ from the source to the drain electrodes through the channel. In the case of applying very small voltages, the system (device) is presumed to be in the linear response regime. Hence, the electronic states close to the Fermi level are mainly involved in the transport and the Fermi function can be replaced with a step function. Now, Eq. 2.2.4 can be written as

$$I = \frac{2e}{h} \left[ \mu_L - \mu_R \right] \int dE \left[ - \left. \frac{\partial f(E)}{\partial E} \right|_{E_F} \right] T(E) \approx \frac{2e}{h} T(E_F) \left[ \mu_L - \mu_R \right]. \tag{2.2.5}$$

In the last step, we make use of the fact that the derivative of a step function is a Dirac delta function. The bias voltage is equal to the difference of the left and right electrodes' chemical potentials ($\mu_L - \mu_R = eV$). The conductance $G$ is defined as the derivative of the current with respect to the applied bias as below

$$G = \frac{\partial I}{\partial V} = G_0 T. \tag{2.2.6}$$

with $G_0 = 2e^2/h$ which is the fundamental quantum conductance. After a decade, the Landauer formula was extended to take into account the conductance of a system with multiple independent transport channels, Büttiker *et al.* employed a quantity

called transmission matrix ($t$). This is the ratio of transmitted wave functions out of the incident wave functions in the central region. All being said, the Landauer-Büttiker formula for total conductance can be written as

$$G = G_0 \, Trace(tt^{\dagger}). \tag{2.2.7}$$

Here, it is clear that the total conductance is described in terms of the quantum conductance and importantly the coefficients of the out-scattered wavefunctions. The framework known as non-equilibrium Green function formalism provides the required tools to calculate such transmission coefficients.

### 2.2.2 NEGF techniques: TranSIESTA

Green's functions (GFs) present a mathematical framework to obtain various physical properties of systems in equilibrium [146]. Working with such GFs is relatively easier, particularly with very efficient recursive methods, to treat many-body quantum systems in comparison to a direct numerical solution of the Schrdinger equation [146]. As a major breakthrough, the application of GF method in quantum transport theory was formulated in 1992 by Meir and Lake in separate papers [147, 148]. Beside being computationally fast and powerful, one of the main advantages of GF techniques is the possible connection to the modern first-principle theory and calculations. Thus, there are many implementations of the Landauer-Büttiker formalism within the NEGF approximation and localized basis functions [149–154]. Here, we present briefly the main concepts of the NEGF method and drive the formulas used in this thesis. For a more detailed and comprehensive explanation of this technique, we refer the curious readers to the book by Datta [151].

In the present study, a linear combination of atomic orbitals are used as basis sets to calculate different properties of defective TMDs monolayers; therefore, the Green's function equation for the whole system can be written as

$$[(E \mp i\eta)S - H]\, \mathcal{G}(E) = I \tag{2.2.8}$$

with $H$ being an effective single-particle Hamiltonian, $S$ an overlap matrix due to the

non-orthogonality of the LCAOs, and $I$ an infinitely-dimensional identity matrix. The solution to this equation is $\mathcal{G}(E) = ((E \mp i\eta)S - H)^{-1}$, which clearly has poles and is not defined at the eigenvalues of the Hamiltonian if $\eta = 0$. In order to resolve this drawback, $\eta$ is considered a small positive/negative value ($0^{-/+}$), resulting in two solutions;

$$\begin{aligned} \mathcal{G}(E) &= ((E + i\eta)S - H)^{-1}, \\ \mathcal{G}^{\dagger}(E) &= ((E - i\eta)S - H)^{-1}, \end{aligned} \tag{2.2.9}$$

where retarded Green's function $\mathcal{G}(E)$ and advanced Green's function $\mathcal{G}^{\dagger}(E)$ represent, respectively, the outgoing and incoming wavefunctions in the electrodes. Besides, $\eta$ is related to the finite life-time of the charge carriers. The real part of these GFs correspond to a shift in the energy levels and can change the effective mass. In principle, the GF matrix can be expanded in any basis representation. If the GFs are expanded in the basis of the Hamiltonian eigenvectors, the poles along the real axis are the corresponding eigenvalues. In this case, the total density of states can be written as

$$N(E) = \frac{1}{2\pi} Trace\left[A(E)\right], \tag{2.2.10}$$

in which the spectral function $A(E)$, one of the important quantities in the GF formalism, is equal to $i[\mathcal{G}(E) - \mathcal{G}^{\dagger}(E)]$. Consequently highlighting one of the primary advantages of the GF methodology which is the possibility to calculate all the properties of a single-particle system without explicitly calculating the eigenstates of the $H$.

For the rest of this section, we present the process to solve the equation 2.2.8 for the retarded GF, e.g. $\epsilon^{+} = lim_{\eta \to 0^{+}} E + i\eta$. Due to the similarity of the Green's function equation for the advanced GF, the solution is the same. Using the block-diagonal structure of the Hamiltonian, the overlap matrix, and the GF matrix, we

now write the Eq. 2.2.8 in the form of

$$\begin{pmatrix} \epsilon^+ S_L - H_L & \epsilon^+ S_{LC} - H_{LC} & 0 \\ \epsilon^+ S_{CL} - H_{CL} & \epsilon^+ S_C - H_C & \epsilon^+ S_{CR} - H_{CR} \\ 0 & \epsilon^+ S_{RC} - H_{RC} & \epsilon^+ S_R - H_R \end{pmatrix} \times \begin{pmatrix} \mathcal{G}_L & \mathcal{G}_{LC} & \mathcal{G}_{LR} \\ \mathcal{G}_{CL} & \mathcal{G}_C & \mathcal{G}_{CR} \\ \mathcal{G}_{RL} & \mathcal{G}_{RC} & \mathcal{G}_R \end{pmatrix} = \begin{pmatrix} \mathcal{I} & 0 & 0 \\ 0 & \mathcal{I} & 0 \\ 0 & 0 & \mathcal{I} \end{pmatrix}, \tag{2.2.11}$$

where subscripts $L$, $R$, and $C$ corresponds to the block quantities for the left electrode, the right electrode, and the central region, respectively. The interaction between the leads and the central region is labeled via subscripts $LC/RC$. The GF block $\mathcal{G}_{LR/RL}$ describes the direct scattering between the two electrodes. We now define the coupling matrices between the channel and the electrodes as

$$\begin{aligned} \tau_L &= H_{CL} - \epsilon^+ S_{CL}, \\ \tau_R &= H_{CR} - \epsilon^+ S_{CR}. \end{aligned} \tag{2.2.12}$$

Since the quantity that we want to evaluate is $\mathcal{G}_C$, a set of equations related to the central region and leads have to be solved simultaneously. This can be accomplished via multiplying the rows of the first matrix by the second column of the second matrix as

$$\begin{aligned} (\epsilon^+ S_L - H_L)\mathcal{G}_{LC} - \tau_L \mathcal{G}_C &= 0, \\ -\tau_L^\dagger \mathcal{G}_{LC} + (\epsilon^+ S_C - H_C)\mathcal{G}_C - \tau_R^\dagger \mathcal{G}_{RC} &= 0, \\ -\tau_R \mathcal{G}_C + (\epsilon^+ S_R - H_R)\mathcal{G}_{RC} &= 0. \end{aligned} \tag{2.2.13}$$

If we define the Green's function of the isolated electrodes, $g_{L,R} = (\epsilon^+ S_{L,R} - H_{L,R})^{-1}$, then the first and last term of the above equation can be rewritten as

$$\mathcal{G}_{LC} = g_L \, \tau_L \, \mathcal{G}_C \quad , \quad \mathcal{G}_{RC} = g_R \, \tau_R \, \mathcal{G}_C. \tag{2.2.14}$$

Substituting these electrode GFs into the second term of Eq. 2.2.13 and performing simple algebra, the final expression for the total GFs of the system can be

written

$$\mathcal{G}_C = \left[\epsilon^+ S_C - H_C - \Sigma_L - \Sigma_R\right]^{-1}, \tag{2.2.15}$$

which contains all the information about the electronic structure of the whole device. Here, $\Sigma_{L,R}$ are the self-energies of the left and right electrodes, including the effect of the semi-infinite electrodes on the isolated channel. They have the form of

$$\Sigma_{L,R} = \tau_{L,R}\; g_{L,R}\; \tau^{\dagger}_{L,R}, \tag{2.2.16}$$

where shows that their dimensionality are defined by the size of the channel. Looking at the Eq. 2.2.15, it can be seen that the total GF is associated with the effective Hamiltonian matrix

$$H_{eff} = H_M + \Sigma_L + \Sigma_R, \tag{2.2.17}$$

where $H_{eff}$ is a complex matrix with a nonzero imaginary part due to the fact that the self-energies are not Hermitian matrices. As a consequence, there is a possibility for the central region to exchange electrons with the electrodes, so that the total number of charge carriers in the channel is not conserved. Knowing this effective Hamiltonian, we can write the GFs of the whole device; hence, calculating all its physical properties. We now need to drive the relation for the self-energies of the semi-infinite leads.

### 2.2.3 Self-energies of the semi-infinite electrodes

To obtain the self-energies of the electrodes, we need to realize the form of coupling matrices and the Green's functions of the semi-infinite leads. The relation for the $g_{L,R}$ can be driven by means of the iterative procedures [155, 156]. Here, it is convenient to divide the electrodes into an infinite series of principal layers (PLs) which is repeated along the transport direction. A principle layer is considered to be the smallest cell possible in such a way that only the nearest neighbor layers interact with each other. Thereupon, the matrix elements corresponding to the interaction of the atoms of two non-adjacent PLs can be neglected [157, 158]. The Hamiltonian matrix of the left and right electrodes can be represented in block-diagonal structure

$$
\begin{aligned}
H_L &= \begin{pmatrix} \ddots & \ddots & \ddots & & 0 \\ & H_{01}^{\dagger} & H_{00} & H_{01} & \\ & & H_{01}^{\dagger} & H_{00} & H_{01} \\ 0 & & & H_{01}^{\dagger} & H_{00} \end{pmatrix} \\
H_R &= \begin{pmatrix} H_{00} & H_{01} & & & 0 \\ H_{01}^{\dagger} & H_{00} & H_{01} & & \\ & H_{01}^{\dagger} & H_{00} & H_{01} & \\ 0 & & \ddots & \ddots & \ddots \end{pmatrix}
\end{aligned} \tag{2.2.18}
$$

with $H_{00}$ corresponding to the interaction between atoms within each PL, while $H_{01}$ and $H_{01}^{\dagger}$ describe the coupling between the two nearest-neighbor PLs. Similarly constructing the overlap matrices, the equation for the GFs of the right electrode which is defined as

$$(\epsilon^{+} S_R - H_R) g_R = I, \tag{2.2.19}$$

has the following form in the matrix representation:

$$
\begin{pmatrix} \epsilon S_{00} - H_{00} & \epsilon S_{01} - H_{01} & 0 \\ \epsilon S_{01}^{\dagger} - H_{01}^{\dagger} & \epsilon S_{00} - H_{00} & \ddots \\ 0 & \ddots & \ddots \end{pmatrix} \begin{pmatrix} g_{0,0} & g_{0,1} & \cdots \\ g_{1,0} & g_{1,1} & \cdots \\ \vdots & \vdots & \ddots \end{pmatrix} = \begin{pmatrix} I & 0 & \cdots \\ 0 & I & \cdots \\ \vdots & \vdots & \ddots \end{pmatrix} \tag{2.2.20}
$$

Using the matrix multiplication for the left-hand side of this equation, the $n+1$ independent equations can be written as

$$
\begin{aligned}
(\epsilon S_{00} - H_{00}) g_{0,0} + (\epsilon S_{01} - H_{01}) g_{1,0} &= I, \\
(\epsilon S_{01}^{\dagger} - H_{01}^{\dagger}) g_{0,0} + (\epsilon S_{00} - H_{00}) g_{1,0} + (\epsilon S_{01} - H_{01}) g_{2,0} &= I, \\
&\vdots \\
(\epsilon S_{01}^{\dagger} - H_{01}^{\dagger}) g_{n-1,0} + (\epsilon S_{00} - H_{00}) g_{n,0} + (\epsilon S_{01} - H_{01}) g_{n+1,0} &= I,
\end{aligned} \tag{2.2.21}
$$

from which we realize the below general form for $n > 1$

$$(\epsilon S_{00} - H_{00}) g_{n,0} = (\epsilon S_{01}^{\dagger} - H_{01}^{\dagger}) g_{n-1,0} + (\epsilon S_{01} - H_{01}) g_{n+1,0}. \tag{2.2.22}$$

From this equation it is clear that the Green's function of the individual PLs depends only on the GF of the neighboring layers. Here, we use the concept of transfer matrices to map the information from the $(n-1)-th$ PL into the $n-th$ PL and vice versa as follows:

$$
\begin{aligned}
P_{n-1,n}\, g_{n-1,0} &= g_{n,0}, \\
\overline{P}_{n,n}\, g_{n,0} &= g_{n-1,0}.
\end{aligned}
\tag{2.2.23}
$$

As a consequence, an iterative scheme is needed to compute the transfer matrices

$$
\begin{aligned}
P &= p_0 + \tilde{p}_0 p_1 + \tilde{p}_0 \tilde{p}_1 p_2 + \cdots + \tilde{p}_0 \tilde{p}_1 \tilde{p}_2 \cdots p_n, \\
\overline{P} &= \tilde{p}_0 + p_0 \tilde{p}_1 + p_0 p_1 \tilde{p}_2 + \cdots + p_0 p_1 p_2 \cdots \tilde{p}_n,
\end{aligned}
\tag{2.2.24}
$$

with matrices $p_i$ and $\tilde{p}_i$ being defined via the recursive relations

$$
\begin{aligned}
p_i &= (I - p_{i-1}\tilde{p}_{i-1} - \tilde{p}_{i-1}p_{i-1})^{-1} p_{i-1}^2, \\
\tilde{p}_i &= (I - p_{i-1}\tilde{p}_{i-1} - \tilde{p}_{i-1}p_{i-1})^{-1} \tilde{p}_{i-1}^2,
\end{aligned}
\tag{2.2.25}
$$

where the initial terms can be written as

$$
\begin{aligned}
p_0 &= -(\epsilon S_{00} - H_{00})^{-1}(\epsilon S_{01}^{\dagger} - H_{01}^{\dagger}), \\
\tilde{p}_0 &= -(\epsilon S_{00} - H_{00})^{-1}(\epsilon S_{01} - H_{01}).
\end{aligned}
\tag{2.2.26}
$$

The result of a self-consistent calculation for the transfer matrices with a convergence threshold of $\delta$, would be independent of n, i.e. $P$. Therefore the surface GF of the right electrode would also be independent of n as

$$
g_R = g_{0,0} = \left[(\epsilon S_{00} - H_{00}) + (\epsilon S_{01} - H_{01})P\right]^{-1}, \tag{2.2.27}
$$

where $g_{1,0} = P g_{0,0}$ is substituted into the first term of Eq. 2.2.21. Following an analogous derivation, the surface GF of the left electrode has the form of

$$
g_L = \left[(\epsilon S_{00} - H_{00}) + (\epsilon S_{01}^{\dagger} - H_{01}^{\dagger})\overline{P}\right]^{-1}. \tag{2.2.28}
$$

Substituting the last two relations for the GF of the leads into the Eq. 2.2.16,

the final form of the corresponding self energies can be written as

$$\begin{aligned}\Sigma_R &= [H_{CR} - \epsilon S_{CR}][(\epsilon S_{00} - H_{00}) + (\epsilon S_{01} - H_{01})P]^{-1}[H_{CR} - \epsilon S_{CR}]^\dagger, \\ \Sigma_L &= [H_{CL} - \epsilon S_{CL}][(\epsilon S_{00} - H_{00}) + (\epsilon S_{01}^\dagger - H_{01}^\dagger)\overline{P}]^{-1}[H_{CL} - \epsilon S_{CL}]^\dagger.\end{aligned} \tag{2.2.29}$$

### 2.2.4 Transmission and conductance

Explained in section 2.2.1, Landauer and Büttiker have proposed a framework to compute the electrical current passing through a device [144,145]. In this formalism, the flow of charge carriers from the left electrode into the device is subtracted from the charges moving out to the right electrode to obtain the total current, i.e. $I = I_L - I_R$, as in Eq. 2.2.4. Here, the chemical potential of the left and right leads are calculated based on the states around the Fermi energy via $\mu_{L,R} = E_F \pm eV/2$, where $V$ is the applied bias. Therefore, the net current is a function of two terms. One is the occupation factor, corresponding to the distribution of the charge carriers in the electrodes, expressed in Eq. 2.2.1. The other component describes the probability of the electrons transmitting from the left to the right lead which is called the transmission coefficient. It is a function of energy and can be written via the Fisher–Lee formula [159] as

$$T(E) = Trace\left[G_C^\dagger(E)\Gamma_R(E)G_C(E)\Gamma_L(E)\right]. \tag{2.2.30}$$

The broadening function $\Gamma(E)$ is related to the imaginary part of the self-energies and has the following form

$$\Gamma_{L,R} = i\left[\Sigma_{L,R}(E) - \Sigma_{L,R}^\dagger(E)\right] = -2Im\Sigma_{L,R}(E). \tag{2.2.31}$$

Substituting the relation 2.2.30 into the Eq. 2.2.6, the energy–dependent electrical conductance can be written as

$$G(E) = \frac{2e^2}{h}Trace\left[G_C^\dagger(E)\Gamma_R(E)G_C(E)\Gamma_L(E)\right]. \tag{2.2.32}$$

## 2.3 Mechanical Deformations

Strain engineering is the art of tuning various properties of the semiconductors via applying mechanical deformations [99]. In order to apply homogeneous and inhomogeneous strains to the 2D materials, experimentalists use various techniques, such as piezoelectric stretching [107], controlled wrinkling [111, 112], Elongating an elastic substrate [110], bending of flexible substrates [108, 109], substrate thermal expansion [105, 106], and nanoindentation via applying external load [50, 96]. Such methods result in a range of mechanical deformations from 0.2% to more than 4.0% [99]. Using an AFM tip, the breaking effective strains has been measured to be between 6.0% and 11.0% [50]

In theoretical simulation, we first change the in-plane lattice vectors of the monolayer based on the applied strain. Then the position of the atoms is relaxed within the new lattice to model the effect of strain on the sample. In this project, four different in-plane strain variations are considered to scrutinize the strain engineering of the 2D TMDs properties. Schematic representation of the strain options are shown in Figure 4.2. Uniaxial strains in X- and Y-direction as well as isotropic biaxial

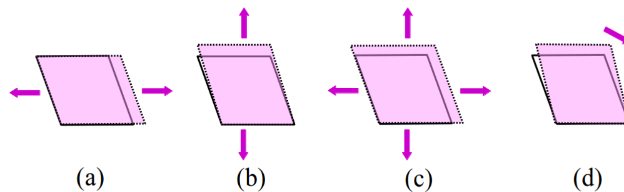


Figure 2.4: (Color online) Schematic representation of the strain options used in the present work: a) X- and b) Y-direction uniaxial strain, c) XY-plane biaxial strain, and d) a shear type (T1) deformation.

strain in the XY-plane are simulated the effects of simple mechanical deformations. We also consider an inhomogeneous shear type (T1), under which only the angle between the in-plane lattice vectors is changed, while keeping their magnitude constant. From 3.0% compressive to 3.0% tensile strains are applied to the unitcell of $MoS_2$ monolayers, to study their electronic structure transitions and validate our method, namely SIESTA package. Further investigating the properties of the defec-

tive 2D TMDs, monolayers are compressed and stretched within the same range as for unitcells.

## 2.4 Formation Energy Calculation

In order to understand the change in the thermodynamic stability of defects under various types of deformations, we calculate their formation energies, $E_f$, for all equilibrated and strained structures, as following:

$$E_{f,\alpha} = E_{d,\alpha} - E_{p,\alpha} + \Sigma_i n_i \mu_i, \tag{2.4.1}$$

where $E_{f,\alpha}$, $E_{d,\alpha}$, and $E_{p,\alpha}$ are the formation energy, the total energy of a defective structure and the corresponding pristine monolayer at strain $\alpha$, respectively. If $\alpha = 0$, this equation gives the formation energies for unstrained structures. Here, the chemical potential of the element $i$ is denoted with $\mu_i$ and the number of vacancy of that atom is given by $n_i$ variable. A detailed description of the approach is presented in Refs. [160–164].

For such analysis, we focus on the defective $MoS_2$ monolayers as a prototype for the family of the 2D TMDs, hence, $i = Mo, S$. In this work, the chemical potentials of Mo and S are presumed to be in a thermal equilibrium with $MoS_2$, meaning:

$$\mu_{MoS_2} = \mu_{Mo} + 2\mu_S. \tag{2.4.2}$$

The limiting factor of the accessible range of the $\mu_{Mo}$ and $\mu_S$ values are the lowest energy phases of these elements. For the case of sulfur chemical potential, it is rather complicated to choose the value due to the fact that there are large number of S allotropes [165]. Sulfur atoms form a solid phase of loosely bound $S_8$ rings at below 100°. Heating it up, S is in the liquid phase at above 120°, and at above 720°, it is found in the gas phase, containing different sulfur molecules. Further increasing the temperature above 820°, sulfurs form diatomic $S_2$ gas. On the other hand, the crystalline structure of molybdenum remain untouched within the range of all realistic growth temperatures [164].

In our calculations, we consider the Mo-rich limit and the body-centered-cubic structure of metal atoms as a reference. The analysis is not affected via this choice of potential reference. While it has been reported that intrinsic defects in ML $MoS_2$ may have charge states, it was shown that the neutral defect states are the most stable over a wide range of Fermi-level positions [164]. Therefore, we focus on the neutral defects in this paper.

# Chapter 3

# $MoS_2$ Monolayers Subject to Mechanical Deformations

The context of this chapter is based on the publication [166].

2D layered materials have gained enormous interest of different fields of science and technology in the past decade, because of their unique electronic, mechanical, and optical properties [1, 8, 28, 167–169], which are strongly dependent on the number of layers. In particular, 2H-phase of Group-6 TMDs monolayers are direct-band gap semiconductors with potential applications in field-effect transistors (FET), spin- and valleytronics, optoelectronics, flexible and piezoelectric devices [1, 10, 16, 24, 103, 169–171]. TMDs monolayers consist of an inner layer of transition metals sandwiched between two layers of chalcogenide atoms, with all three layers having hexagonal symmetry, as shown in Figure 1.2 [24, 25]. Previous studies have revealed unprecedented opportunities to tune their electronic properties via defects [17], strain [172], and nanostructuring [173].

A well-known member of 2D TMDs family, $MoS_2$ monolayers, was exfoliated for the first time in 2010 and characterized as a direct-band gap semiconductor [21, 22]. Shortly afterwards, its application in nanoelectronics was proposed and the first top-gated FET using $MoS_2$ was reported [23]. However, the synthetic samples of $MoS_2$ MLs contain some fraction of intrinsic defects, as discussed in Ch. 1.3. There, we also explain that structural defects and impurities can be introduced deliberately,

e.g., at the post growth stage. Besides, Ch. 1.4 shows the significant effect of the mechanical deformations on energetic and electronic properties of Group-6 TMDs monolayers, offering rapid and reversible tuning of their band gaps and the defect levels (DLs).

In this chapter, the effect of various strain situations are investigated on formation energies, orbital characteristics, and DLs of intrinsic point vacancies in $MoS_2$ monolayers. Since we use the periodic boundary conditions (PBC) in the framework of the first principle DFT, structural properties have to be chosen in a way that the interactions between defects inside the adjacent images become negligible. Hence, it is necessary to consider very large systems when studying defective monolayers. In order to significantly reduce the computational and storage requirements, we have selected the SIESTA method [134,174], which uses LCAO to expand the Kohn-Sham wavefunctions as shown in Ch. 2.1.5. First, we go over the parameters used for these computations. Then, a comparison of the calculated properties of the $MoS_2$ unit-cell is presented, both for bulk and monolayer, with respect to the previous studies. Then, the energetic properties of the point defects inside the MLs $MoS_2$ under strain are scrutinized. Finally, the electronic structure of such defective 2D materials are analyzed as a function of applied mechanical deformation. Complementary plots and images are provided in the Appendix A, which help with understanding the presented analysis.

## 3.1 Computational Details

In the present study, relativistic, norm-conserving pseudopotentials, including the correction from core electrons, are used, which were obtained by the Troullier-Martin method [175, 176]. This set of pseudopotentials are self-generated by means of *"atom"* tool, provided along with the SIESTA's source code. The input parameters are reported in A.5. The exchange and correlation interactions were described by the Perdew-Burke-Ernzerhof (PBE) functional in the generalized gradient approximation (GGA) [126]. In all the geometric optimizations and electronic calculations, we employed a double-zeta basis set with one polarization function (DZP) and 4p

diffusive orbitals. The Energy-Shift and the Split-Norm were set to 0.02 Ry and 0.16, respectively. We used an energy cut-off of 450 Ry to calculate hartree, exchange, and correlation contribution to the total energy. A vacuum of 40 Å along the out-of-plane ($c$) axis was used to make the structures effectively isolated as 2D layers. The conjugate-gradients (CG) technique was used to optimize the atomic positions and lattice vectors of equilibrium and strained configurations. The lattice constants along with the atomic positions of the unit cell, both for monolayer and bulk, were optimized until the Hellman–Feynman forces are below 10 meV/Å. Keeping the optimized lattice parameters, the same criterion was chosen to find the equilibrium atomic position of the pristine and defective supercells. Applying Monkhorst-Pack method, the Brillouin zone (BZ) was sampled with $25 \times 25 \times 1$, $25 \times 25 \times 15$ and $5 \times 5 \times 1$ k-points for the unit cell monolayer, bulk, and supercell calculations, respectively. To ensure the results are converging with respect to the k-points and energy cut-off, the threshold for $\triangle E_{tot}$ are chosen to be $10^{-5}$ eV and $10^{-4}$ eV, respectively, with $\triangle E_{tot}$ being the total energy difference. The ground state of $MoS_2$ monolayer with defects was shown to be non-magnetic up to more than +5% strain [177]. Hence, spin-polarization was neglected in our calculations. Although the spin-orbit coupling (SOC) affects the band structure of TMDs monolayers, the qualitative picture of the electronic structure of DLs is preserved according to the previous studies [178–180]. Thus, the SOC was not included in the present work. The total energies were considered converged when the difference between two consecutive self-consistent field (SCF) steps was less than $10^{-4}$ $eV$.

## 3.2 $MoS_2$ unitcell: Bulk & Monolayer

Using our optimized basis-set as well as self-generated pseudopotentials for molybdenum and sulfur, lattice parameters and electronic properties of bulk structure and monolayers of $MoS_2$ are calculated. For the fully optimized unit cell of MLs $MoS_2$, we obtained the in-plane (xy-plane) lattice constant of 3.176 Å. The Mo–S bond-lengths and the S–Mo–S angles are equal to 2.427 Å and 81.9°, respectively. For bulk $MoS_2$ structures, our calculated $c/a$ ratio is 4.37 Å. It can be seen from Table. 3.1

| Property | Monolayer $MoS_2$ | Bulk $MoS_2$ |
|---|---|---|
| Lattice Constant (in Å) | 3.176<br>3.173[a], 3.23[b], 3.185[c], 3.1827[d] | 3.176<br>3.23[b], 3.1827[d], 3.16[e] |
| c/a Ratio (in Å) | 40Å vacuum along $c$ axis | 4.37<br>4.001[a], 4.01[b], 4.3474[d], 3.89[e] |
| Bond Length (Mo–S) (in Å) | 2.427<br>2.45[b], 2.416[c], 2.41[d] | 2.426<br>2.45[b], 2.41[e] |
| Bond Angle (S–Mo–S) (in degree) | 81.90<br>80.88[b] | 81.90<br>80.84[b], 81.30[e] |
| Distance (S–S) (in Å) | 3.181<br>3.18[b], 3.133[c] | 3.179<br>3.18[b], 3.19[e] |

Theory (GGA-PBE): a= [184], b= [185], c= [186], d= [183];
Experiment: e= [21, 22, 181, 182]

Table 3.1: Structural parameters are calculated using GGA-PBE functional for monolayer and bulk $MoS_2$. For the purpose of comparison, experimental values and theoretical results are also provided.

that structural properties agree well with available crystallographic data and experimental measurements [21, 22, 181, 182]. In this table, comparing our result with the outcomes of the theoretical studies at the same level of DFT accuracy (GGA-PBE functionals) also indicates a very good agreement [183–186].

The realization of the band gap in $MoS_2$, generally in TMDs, stems from the strong hybridization between the metallic-$d$ orbitals, where band edges exhibit a strong character variation [181, 182]. Due to symmetry reasons, $d_{xz}$, $d_{yz}$, and $p_z$ orbitals are decoupled from other orbitals, which construct the other states, in both cases of monolayer and bulk structure.

In Figure 3.1 the calculated band structure and orbital characteristics, marked with colors, are shown for the bulk $MoS_2$, using the same pseudopotentials as for monolayers. The valance band edge at the Γ-point is higher than at the K-point, therefore; an indirect band gap of 1.37 eV is realized between the Γ-point in the valence band maximum (VBM) and the Q-point (between Γ and K) in the conduction band minimum (CBM), in agreement with earlier studies [25, 164, 185]. All occupied and unoccupied bands around the Fermi energy consist of $d_{x^2-y^2}$, $d_{xy}$, and $d_{z^2}$

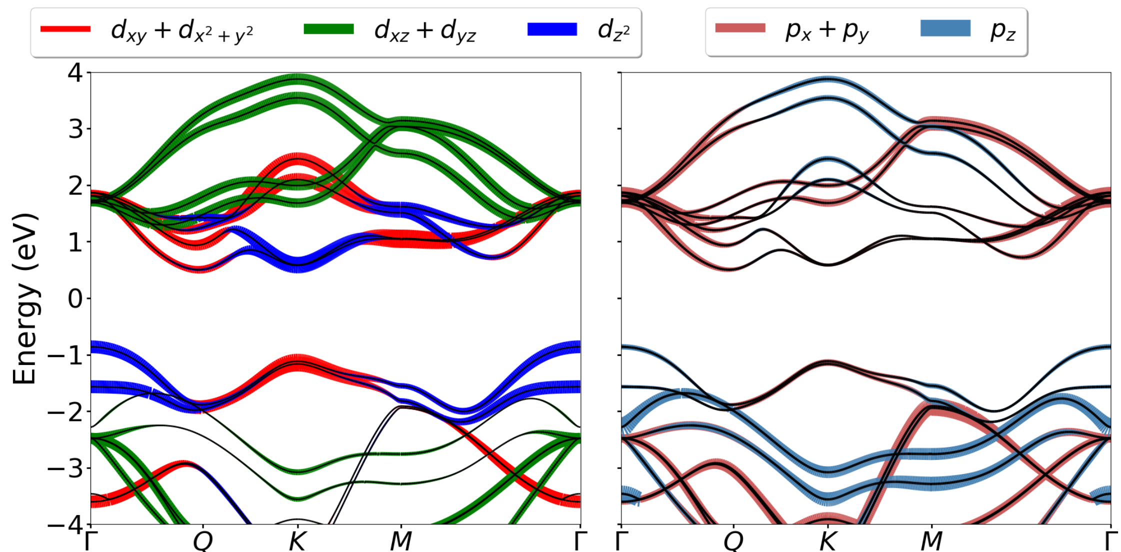


Figure 3.1: (Color online) The calculated band structure of the bulk $MoS_2$ in a unit cell representation. The energies were shifted with respect to the Fermi level, which was set in zero. Contributions from Mo-4$d$ (S-3$p$) orbitals to the states around the Fermi energy are marked with colors and shown in the left (right) panel.

orbitals of Mo hybridized with $p_x$ and $p_y$ orbitals of S, as illustrated respectively in the left and right panel of Figure 3.1, in accordance with previous studies [185–188].

Band structure for $MoS_2$ monolayers is plotted in Figure 3.2 where orbital components involved in the bands around the Fermi energy are highlighted with colored line width. Major contributions to the band edges are originated from mettalic d-orbitals, $d_{x^2-y^2}$, $d_{xy}$, and $d_{z^2}$ (see the left panel in this figure ), while $p_x$ and $p_y$ orbitals of sulfur mainly contribute to the CBM around the Γ-point, as in the right panel of the Figure 3.2. These are in very good agreement with previous studies [25,185,187]. For example, a detailed description of the orbital characteristics of the bands has been obtained by means of a 11-band tight-binding model Hamiltonian [187]. According to our calculation on the optimized geometry, MLs $MoS_2$ is a direct-band gap semiconductor with a gap of 1.73 eV at the $K$ point, which is in accordance with theoretical results with GGA-PBE functional [25, 164, 184–186]. It should be emphasized, that the true quasi-particle band gap is about 2.4 to 2.9 eV [12,25,189]. Our results differ due to the well-known underestimation of the band gap in GGA.

It has been reported that the electronic structure of pristine MLs TMD can be

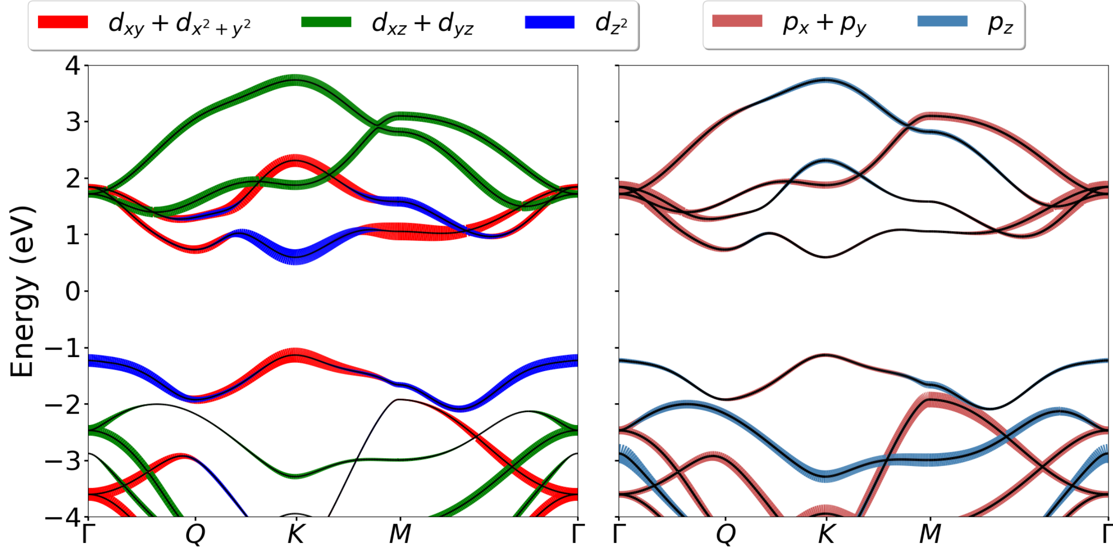


Figure 3.2: (Color online) The calculated band structure of the MLs $MoS_2$ in a unit cell representation. The energies were shifted with respect to the Fermi level, which was set in zero. Contributions from Mo-4*d* (S-3*p*) orbitals to the states around the Fermi energy are marked with colors and shown in the left (right) panel.

tuned in a controlled way via strain [99,100,190]. Further analyzing our method and the self-generated parameters, the change in the band gap of the pristine MLs $MoS_2$ is studied as function of four strain situations, as shown in Figure 3.3. Direct band gap is plotted with blue line, while red and green lines show indirect band gaps from Γ-point in the VBM to K-point in the CBM, and from K-point in the VBM to Q-point in the CBM, respectively (see Figure 3.2). Even though the applied strains are considered within a range of 3% compression to 3% tesnile, breaking point of the MLs $MoS_2$ has not been reached as predicted via experimental measurements [50].

According to our calculations, a direct-indirect transition is realized for the band gap of pristine MLs $MoS_2$ at 1.5% (less than 2.0% ) uniaxial tensile (compressive) strain in X- and Y-direction, agreeing very well with previous reports [99, 100]. In line with these studies, the cases of isotropic biaxial strain cases lead to a direct-indirect band gap transition at less than 1.0%, for both compressing and streching. In the right plot of Figure 3.3 can be seen that band gap of MLs $MoS_2$ remains direct over the whole range of the considered inhomogeneous shear T1 strain.

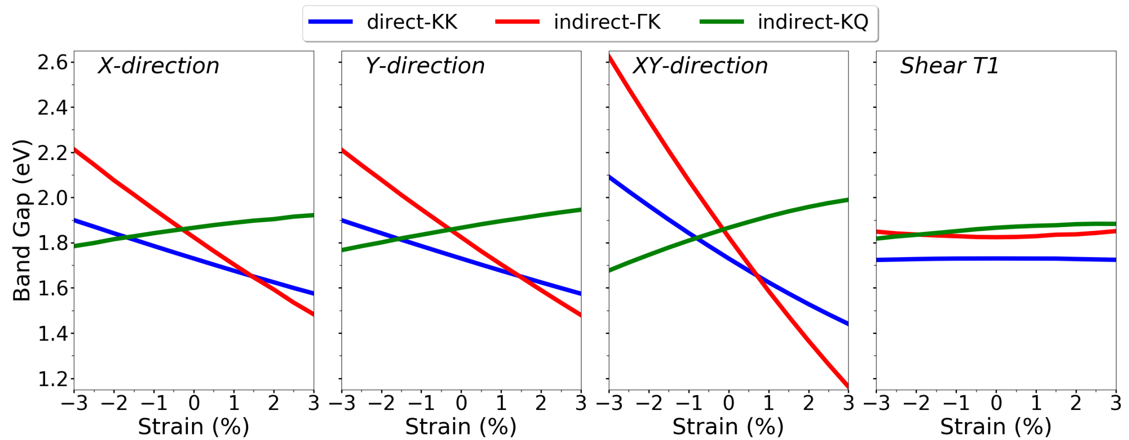


Figure 3.3: (Color online) The change in the band gap of pristine MLs $MoS_2$ under various compressive and tensile strain cases; uniaxial strain in X- and Y-direction, biaxial strain in XY-direction, and an inhomogeneous shear T1 strain. Direct band gap is plotted with blue line, while red and green lines show indirect band gaps.

## 3.3 Monolayer of $MoS_2$ with Vacancies

Our objective is to scrutinize the influence of compressive and tensile strains on the electronic and energetic properties of the MLs $MoS_2$ with intrinsic vacancies. Such defects have advantages and disadvantages based on the desired application. For example, depending on the concentration of the defects, performance of $MoS_2$-based FETs may differ by several orders of magnitude [23, 55, 81]. On the other hand, some studies imply that the vacancy creation can extend the application of $MoS_2$ nanosheets [47, 83–86], e.g. as single-photon emitters, due to localized states of the isolated defects [47, 85]. In a recent study, molybdenum (Mo) vacancies were generated site-selectively to write optically active defect states in TMDs MLs [47]. The mid-gap localized levels have also observed to improve the photoresponsivity of $MoS_2$ monolayers by trapping the photo-excited charge carriers, leading to a growth of the photocurrent in photodetectors [87–89]. Furthermore, intrinsic defects such as sulfur (S) and Mo vacancies, may promote the contact resistance and the carrier transport efficiency of devices depending on the electrode's elements [65, 90–93].

We work with the PBCs to simulate the vacancies inside the monolayers. Supercells with sizes ranging from 6×6×1 up to 8×8×1 are created to realize the decrease

in the defect-defect interactions in the computational model. Accordingly, chalcogen vacancies were studied in a 7×7×1 supercell representation, while supercells of 8×8×1 were considered to scrutinize the transition metal vacancies and vacancy complexes.

Figure 3.4 displays the structures of the MLs $MoS_2$ with various point defects: $V_S$, $V_{2S-top}$, $V_{2S-par}$, $V_{Mo}$, $V_{Mo+3S}$, and $V_{Mo+6S}$. The position of the vacancies inside

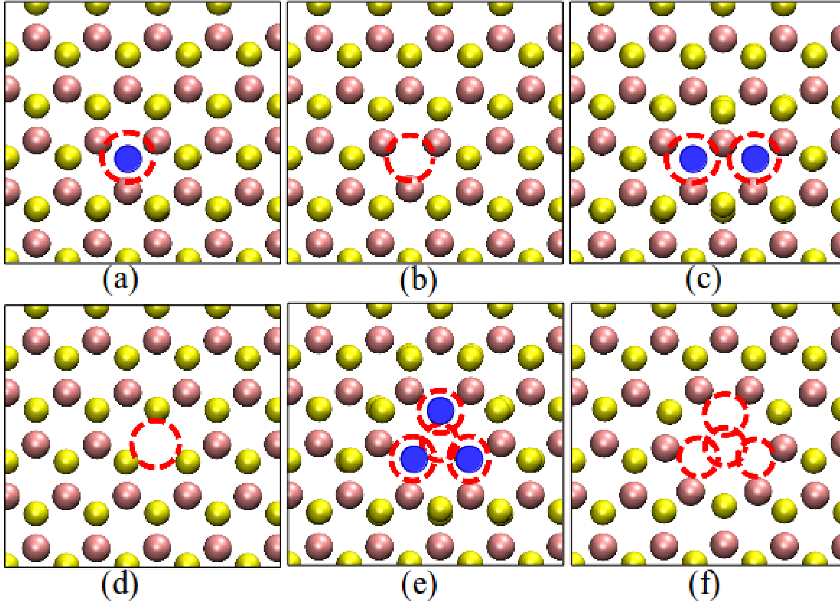


Figure 3.4: (Color online) Geometries of MLs $MoS_2$ with vacancies: a) $V_S$, b) $V_{2S-top}$, c) $V_{2S-par}$, d) $V_{Mo}$, e) $V_{Mo+3S}$, f) $V_{Mo+6S}$. Red dashed-circles denote the position of the defects inside the monolayers. At the vacancy sites, sulfurs from the lower layer are highlighted with blue solid points.

the monolayers is denoted with the red dashed-circles. The blue solid points are highlighting the sulfurs from the lower layer at the vacancy sites. These vacancies were observed in experimental samples by means of atomic-resolution measurements and analyzed via theoretical techniques [17,61,82,164,191,192]. S and Mo vacancies could also be produced by processes such as ion-irradiation and plasma exposure [47, 75,82,192]. Most of the defects kept the $C_{3v}$ symmetry of the monolayer, except for the sulfur-pair vacancy in the top atomic layer, $V_{2S-par}$, as depicted in Figure 3.4(c).

We also study the local strains induced into the MLs $MoS_2$ by such defects. Here, the amount of shifts in the position of atoms surrounding the defects are calculated

with respect to their position in the pristine structure. This property is called the displacement map, in Å, and illustrated in Figure 3.5. It can be seen that $V_{Mo}$

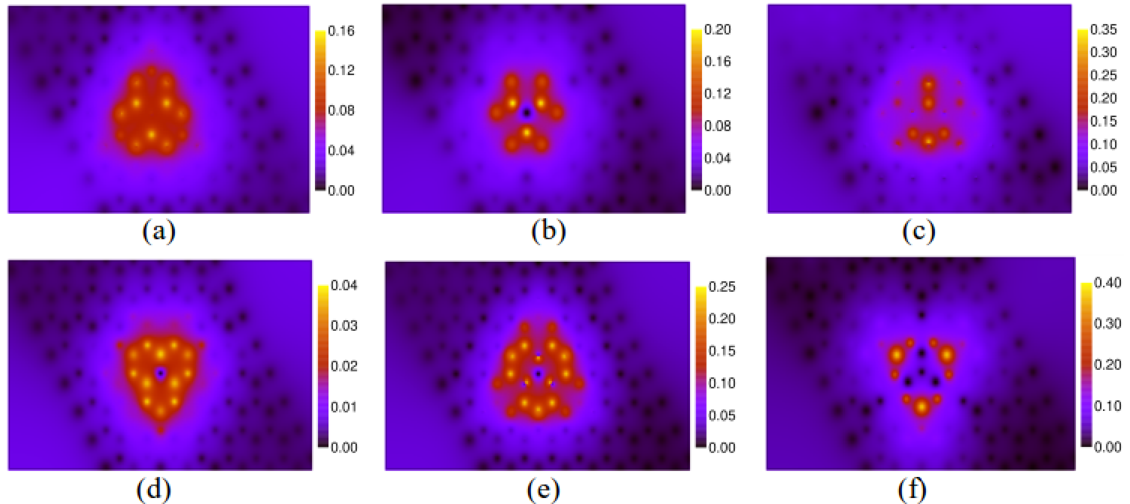


Figure 3.5: (Color online) The displacement map of atoms in the MLs $MoS_2$ surrounding the defects as a) $V_S$, b) $V_{2S-top}$, c) $V_{2sv-par}$, d) $V_{Mo}$, e) $V_{Mo+3S}$, f) $V_{Mo+6S}$. All the numbers in the colorboxes are in Å.

has the smallest impact on the neighboring atoms in the MLs $MoS_2$, up to 0.08 Å shift. For the case of $V_S$, $V_{2S-top}$, and $V_{Mo+3S}$ vacancies, the neighboring atoms are moved up to 0.16 Å, 0.20 Å, and 0.25 Å, respectively. These figures also show that the atomic positions are mostly renormalized by the presence of the defects $V_{2sv-par}$ ($V_{Mo+6S}$) in the $MoS_2$ monolayers with the amount of 0.35 Å (0.40 Å). Such displacement maps emphasize the significance of the local rearrangements caused by the intrinsic vacancies inside the defective monolayers. The electronic structure of 2D materials are very sensitive to strain [50,99,100,193]. Therefore, it was conlcuded that selecting the largest possible supercell size and performing atomic optimization are in fact crucial in further studying their properties.

### 3.3.1 Energy of formation

Equation 2.4.1 is used to obtain the energy required to form such point defects inside the $MoS_2$ monolayers. Calculated formation energies, as shown in Figure 3.6, are in line with previous studies [61, 164, 188, 193].

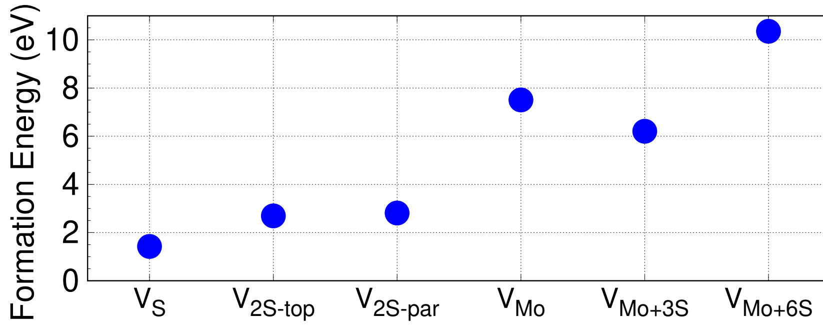


Figure 3.6: (Color online) Calculated formation energies of different sulfur- and molybdenum-based vacancies in MLs $MoS_2$.

We found that the most probable defect in MLs $MoS_2$ is a single S vacancy, $V_S$. Formation energies when removing two sulfur atoms from top and bottum layer at the same site, $V_{2S-top}$, is very close to the case of removing two neighboring sulfur atoms from the same layer, $V_{2S-par}$. It can be seen in Figure 3.6 that observation of the vacancy complex $V_{Mo+3S}$ in synthesiozed samples is more likely than a single Mo vacancy, $V_{Mo}$. This is due to the coordination of the metal atoms and the fact that they are sandwiched between two S-atom layers. Hence, when creating Mo vacancies for single-photon emitters at selective sites [47], care has to be taken not to generate vacancy complexes. The energy required to form a molybdenum vacancy with its six neighboring sulfur atoms, $V_{Mo+6S}$, is the highest among all the suggested types of defect.

As previous studies have shown, the qualitative picture of occupied and unoccupied DLs in the band structure are unaffected when the SOC is included in the calculations. Thus, modification of the formation energies due to the spin-orbit effect are considered to be small and neglected in the present study [178–180]. In our calculations, we consider the Mo-rich limit and the body-centered-cubic structure of metal atoms at $0K$ temperature as a reference. While it has been reported that intrinsic defects in MLs $MoS_2$ may have charge states, it was shown that the neutral defect states are the most stable over a wide range of Fermi-level positions [164]. Therefore, the focus of this chapter is on the properties of the neutral defects.

### 3.3.2 Defect levels: Position and orbital characteristics

Shown in Figures 3.7 and 3.8, the electronic band structure of MLs $MoS_2$ are plotted, containing sulfur and molybdenum vacancies as well as vacancy complexes; $V_S$, $V_{2S-top}$, $V_{2S-par}$, $V_{Mo}$, $V_{Mo+3S}$, $V_{Mo+6S}$. Here, defect states are highlighted according to the orbital components involved in their orbitals characteristics. Major contributions to the VBM and CBM mostly come from $d_{xy}$, $d_{z^2}$, and $d_{x^2+y^2}$ orbitals. The fact that the DLs are dispersionless, indicates the negligibility of the defect-defect interactions in 7×7×1 (8×8×1) supercells for S-(Mo-)based vacancies. These outcomes are in contrast to previous studies in which dispersion can be seen in the localized states [60, 179, 194, 195].

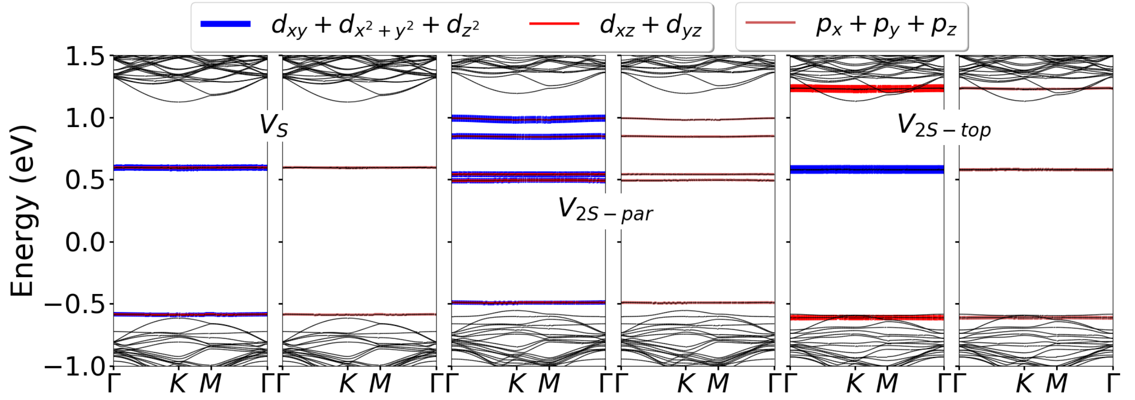


Figure 3.7: (Color online) The calculated band structure of the MLs $MoS_2$ with defects: $V_S$, $V_{2S-top}$, $V_{2S-par}$, are plotted along the high symmetry lines in the BZ. The energies were shifted with respect to the Fermi level, which was set in zero. Orbitals contributions to the DLs are also highlighted with colors. The VBM and CBM are mostly composed of $d_{xy}$, $d_{z^2}$, and $d_{x^2+y^2}$ orbitals.

Presence of sulfur vacancy, $V_S$, in $MoS_2$ monolayers leads to a localized state near the VBM and double degenerate mid-gap states which are unoccupied. Figure 3.7 shows that in the case of a sulfur-pair vacancy on the top atomic layer, $V_{2S-par}$, five non-degenerate DLs occur, one occupied and four unoccupied. A sulfur divacancy, $V_{2S-top}$, in MLs $MoS_2$ introduces similar localized states as in the case of $V_S$ together with another double-degenerate DLs whitin the CBM. According to our wavefunction analysis, the orbital characteristics of these DLs are mainly originated from $4d$ orbitals of molybdenum atoms, surrounding the vacancies, with a small contribution

from S-3$p$ orbitals. These results agree well with previous studies [77, 188, 196].

Shown in Figure 3.8, when $MoS_2$ monolayers contain a single Mo vacancy, $V_{Mo}$, double-degenerate occupied states can be seen in the band structure which is mainly constructed of 3$p$ orbitals of sulfur. There are also a non-degenerate and double-degenerate unoccupied states within the band gap to which $d_{xy}$, $d_{z^2}$, and $d_{x^2+y^2}$ orbitals mostly contribute. Structure of MLs $MoS_2$ with the vacancy complex of $V_{Mo+3S}$ is shown in Figure 3.4. Analyzing the orbitals characteristics indicates that all the localized states are composed of hybridization of $d$ and $p$ orbitals of atoms surrounding the vacancy. For the case of the vacancy complex with one molybdenum and six sulfurs, $V_{Mo+6S}$, DLs around the Fermi energy are composed of $d_{xz}$, $d_{yz}$, and $p$ orbitals while other unoccupied localized states are mostly constructed from $d_{xy}$, $d_{z^2}$, and $d_{x^2+y^2}$ orbitals. Our findings are in accordance with previous reports for the unstrained $MoS_2$ monolayers [77, 188, 196].

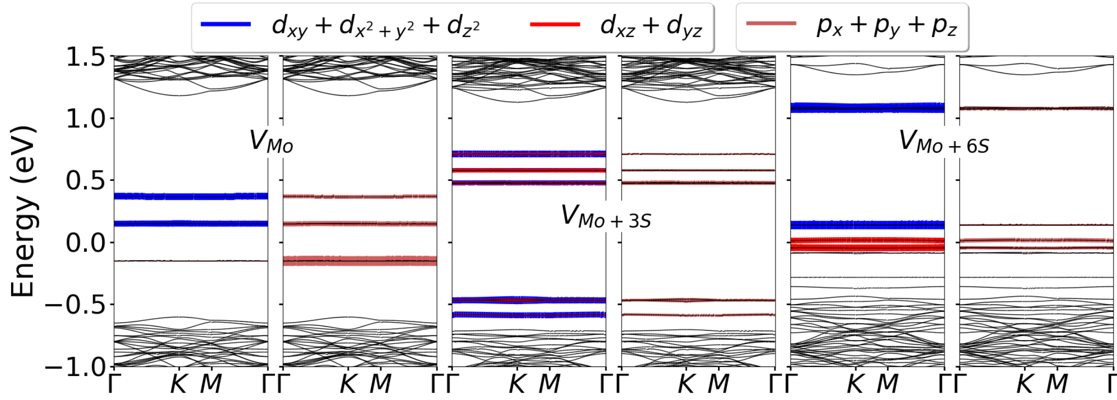


Figure 3.8: (Color online) The calculated band structure of the MLs $MoS_2$ with defects: $V_{Mo}$, $V_{Mo+3S}$, $V_{Mo+6S}$, are plotted along the high symmetry lines in the BZ. The energies were shifted with respect to the Fermi level, which was set in zero. Orbitals characteristics of the DLs are also highlighted with colors. The VBM and CBM are mostly composed of $d_{xy}$, $d_{z^2}$, and $d_{x^2+y^2}$ orbitals.

## 3.4 Strain Engineering of the Properties

It has been reported that the strain-engineering provides feasible approaches for tuning the properties of the 2D materials, in particular MLs TMDs. This leads to

new potential applications, such as piezoelectricity in $MoS_2$, broad-spectrum solar energy funnel, and flexible transparent phototransistors [10, 11, 16, 103, 104]. It was also observed that biaxial strain can tune the properties of photodetector devices based on $MoS_2$ monolayers [11]. Therefore, it is of great importance for the industrial applications of such structures to investigate the effect of mechanical deformations on the position of the localized states in the defective monolayers. A wide range of strain values, from 3.0% compression up to 5% tension, are considered yet they are below the breaking point of the MLs $MoS_2$ estimated from experiments [50]. We also investigate the sensitivity of the formation energies to various strain situations.

### 3.4.1 Energetics

Figure 3.9 shows the formation energies of the six studied vacancies as function of four different mechanical deformations applied to the defective $MoS_2$ monolayers. In earlier reports, the case of $V_S$ vacancy in MLs $MoS_2$ under uniaxial and biaxial strain was considered [30, 172], corresponding to pluses, crosses, and triangles in Figure 3.9(a). While our results agree very well with these works, we study several other sulfur based defects and vacancy complexes as well as various strain situations in Figure 3.9(a)–(f). In all the compressive strain situations, formation energies of the six vacancies are lowered. Moreover, the uniaxial and biaxial tensile strains increase the formation energy for $V_S$, $V_{2S-top}$, $V_{2S-par}$, and $V_{Mo+6S}$ defects, while a reduction is observed for $V_{Mo}$ and $V_{Mo+3S}$. This behavior stems from the fact that the latter two vacancies are surrounded by $3p$ orbitals of the neighboring S atoms in comparison with the other defects with $4d$ orbitals of Mo neighbors. When $V_{2S-par}$ is present in the MLs $MoS_2$, the strain in X- and Y-direction do not cause identical energy shifts, due to the broken $C_{3v}$ symmetry. The geometry modifications also lead to a similar behavior for a Mo vacancy under $\pm1.5\%$ of uniaxial strains. Applying the shear T1 tensile deformations, the formation energies of $V_{Mo}$ and $V_{Mo+3S}$ are reduced as DLs are constructed of $3p$ orbitals of the neighboring sulfur atoms. For the case of other vacancies, since some of the orbitals composing the DLs are mixing under the shear T1 tensile strain, the formation energies are decreased. All in all, uniaxial

and isotropic biaxial strains modify their energetic properties more profoundly than shear T1 strain.

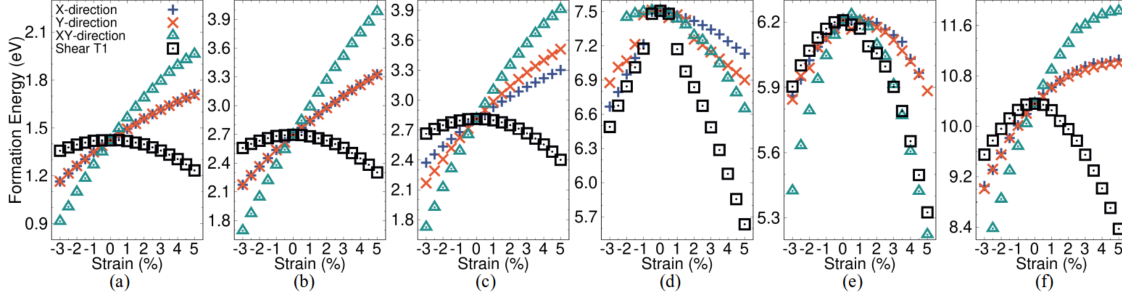


Figure 3.9: (Color online) The evolution of the formation energy as function of four different deformations applied to a) $V_S$, b) $V_{2S-top}$, c) $V_{2S-par}$, d) $V_{Mo}$, e) $V_{Mo+3S}$, and f) $V_{Mo+6S}$ models of defective $MoS_2$. Symbols $+$, $\times$, $\triangle$, and $\boxdot$ correspond to the strain in X-, Y-, XY-direction, and shear T1, respectively.

### 3.4.2 Electronics: Sulfur vacancies

To study the effect of strain on the electronic properties of S-based defects within the $MoS_2$ monolayers, we have investigated the change in the positions of the DLs and their orbital composition for all studied strain situations. Figure 3.10 and 3.11 show the results obtained for the $V_{2S-top}$ and $V_{2S-par}$ defects, respectively. In addition, the corresponding results obtained for a single sulfur vacancy, $V_S$, are shown in Figures A.1 and A.2 in Appendix A. Green dashed-lines and black lines indicate the position of the Fermi energy and band edges, respectively. The occupied DLs in all the defective structures are shifted significantly less than the unoccupied DLs under any of the applied strain situations.

In the relaxed $MoS_2$ monolayers with $V_{2S-top}$, based on analysis of the orbital characteristics, DL2, DL3, DL4, and DL5 levels are mostly composed of $d_{xy}$, $d_{x^2-y^2}$, $d_{xz}$, and $d_{yz}$ orbitals of the neighboring Mo atoms, respectively. Since the deep defect levels, DL2 and DL3, exhibit the most pronounced shifts, we show the superimposition of the orbital character involved in those bands at integer strains, by the symbol sizes, in analogy to the fatbands. Such fatbands are projections of orbitals onto the corresponding band eigenvalues. These are not depicted for the case of biaxial strain under which the degeneracy is maintained. Illustrated in Figure 3.10(a)

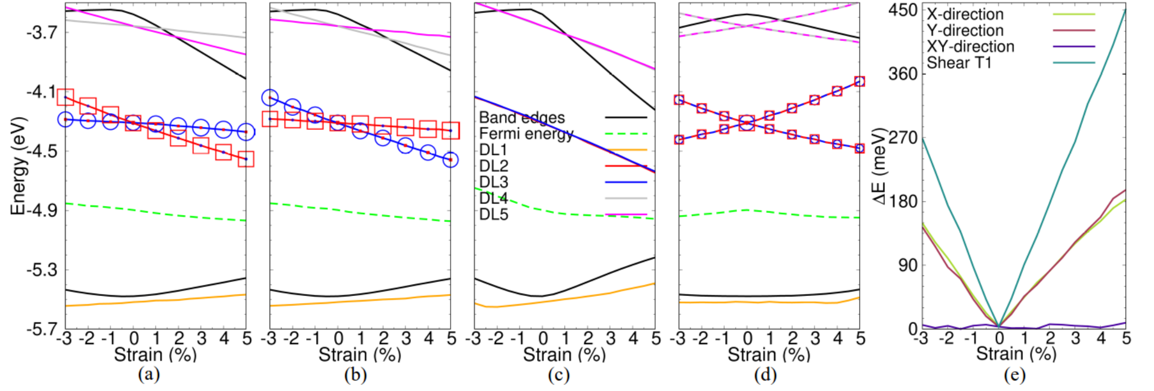


Figure 3.10: (Color online) Evolution of the DLs of the MLs $MoS_2$ with $V_{2S-top}$ defects under strain in a) X-direction, b) Y-direction, c) XY-direction, and d) shear T1. The Fermi level and band edges (VBM and CBM) are indicated with green dashed-line and black lines, respectively. The defect states, DL1–DL5, are shown with orange, red, blue, gray, and magenta lines, respectively. $d_{xy}$ and $d_{x^2-y^2}$ orbitals are plotted with red squares and blue circles, respectively, only for DL2 and DL3 bands at integer uniaxial and shear T1 strains. e) The amount of degeneracy splitting of the deep DLs is plotted in the same interval for all four strains.

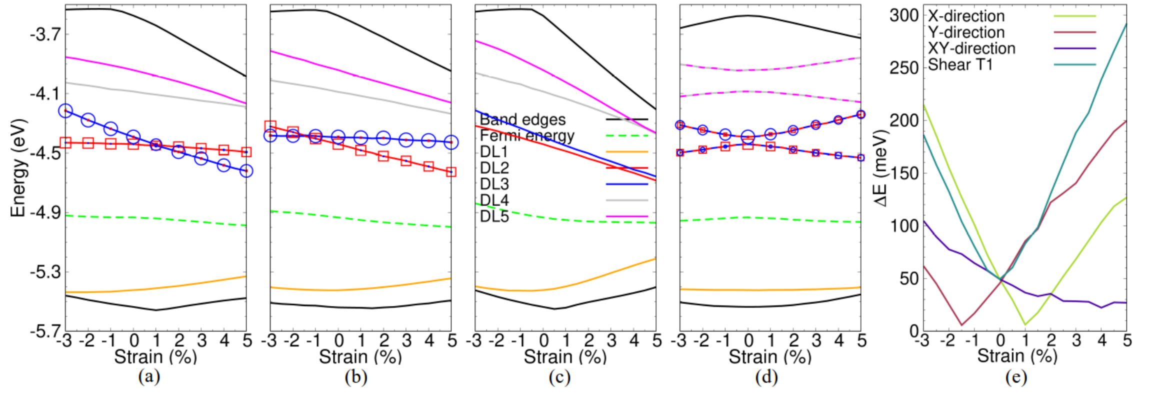


Figure 3.11: (Color online) Evolution of the DLs of the MLs $MoS_2$ with $V_{2S-par}$ defects under strain in a) X-direction, b) Y-direction, c) XY-direction, and d) shear T1. The Fermi level and band edges are indicated with green dashed-line and black lines, respectively. Color legend as in Figure 3.10. $d_{x^2-y^2}$ and $d_{xy}$ orbitals are plotted with red squares and blue circles, respectively, only for DL2 and DL3 bands at integer uniaxial and shear T1 strains. e) The amount of degeneracy splitting of the deep DLs is plotted in the same interval for all types of strains.

and (b), for strain in X(Y)-direction, the DL2(DL3) level is strongly tuned so that they are anti-crossing. This opposite shift of degenerate DLs is the consequence of the relative direction of each uniaxial strain to the nodal planes of the orbitals involved in the bands. Shown in Figure 3.10(c), since biaxial isotropic strain does not

break the $C_{3v}$ symmetry, the degeneracy remains intact, but the bands are shifted up(down) by compressive (tensile) strains. The hexagonal symmetry is removed via uniaxial and shear T1 strains which leads to breaking of the degeneracy of both the deep levels and the states around the CBM. Although the orbital composition can be uniquely identified for the relaxed MLs, shear T1 strain increases mixing of the orbital contributions from Mo neighbors into the DLs resulting in additional hybridization of the orbitals and a strong shift in the opposite directions, as shown in Figure 3.10(d). While a composition of $d_{x^2-y^2}$ and $d_{xy}$ makes up the states DL2 and DL3, localized level DL4 and DL5 are a mixture of $d_{xz}$ and $d_{yz}$ orbitals. In Figure A.3, the change in the orbital components of the mid-gap DLs as function of applied strains is demonstrated. The degeneracy splitting of DL2 and DL3, $\Delta E$, is shown as function of compressive and tensile strains in Figure 3.10(e). The splitting reaches to almost 200 meV and 450 meV for 5% of tensile uniaxial and shear T1 strain, respectively. As illustrated in Figure A.1, the DLs for a $V_S$ inside MLs $MoS_2$ demonstrate similar behavior under strain. However, compare to Figure 3.10(e), the splitting of the deep degenerate levels of $V_S$ is about half for the same amount of strain. In some experiments, luminescence peaks are assigned to intrinsic defects and oxygen passivation techniques are applied to identify their type [60, 197, 198]. The obtained difference in the degeneracy splitting of DLs, can be used as a noninvasive process to distinguish, e.g. $V_{2S-top}$ from $V_S$, even though the position of their DLs inside the band gap are very similar in the unstrained cases.

Due to the absence of the $C_{3v}$ symmetry in the $MoS_2$ MLs with $V_{2S-par}$, no degenerate levels are present in the band structure of the unstrained defective monolayer, as shown in Figure A.4(c). These bands are labeled DL1 to DL5 in Figure 3.11(a)–(d). In Figure A.4, we show the principal orbitals constituting these DLs of relaxed and strained defective MLs. Two defect states closer to the Fermi level, DL2 and DL3, mostly consist of $d_{x^2-y^2}$ and $d_{xy}$ orbitals of neighboring Mo atoms, respectively. As the change in these DLs are the highest, their orbital characteristics are highlighted in Figure 3.11 via symbols whose sizes are obtained following fatbands analysis at integer uniaxial and shear T1 strains. Moreover, main orbitals

in DL4 (DL5) are $d_{xy}$ and $d_{z^2}$ ($d_{x^2-y^2}$ and $d_{xz}$). The uniaxial strain in X-direction (Y-direction) tunes DL3 (DL2) much more than DL2 (DL3) in such a way that bands anticross each other at around +1% (−1.5%) strain. This tendency is related to the directional influence of uniaxial strains on the nodal planes of the orbitals corresponding to these localized states. As it shows in Figure 3.11(c), the isotropic biaxial compressive and tensile strains move the deep DLs relative to each other as the overlap between their orbitals varies. Shear T1 strain combines the orbital components of DLs in a way that a mixture of $d_{xz}$ and $d_{yz}$ ($d_{x^2-y^2}$ and $d_{xz}$) orbitals is added to $d_{x^2-y^2}$ ($d_{xy}$) orbital to make DL2 (DL3) state, as shown in Figure 3.11(d). Accordingly, the orbitals are further hybridized and bands are shifted in the opposite direction. The orbital characteristics of other two bands, DL4 and DL5, are also mixed. Thus, they move away for all strain values. The absolute splitting of DL2 and DL3 under four types of strain is shown in Figure 3.11(e). For the case of shear T1 strain, even though the band edges are not modified as much as the other deformations, the separation of the localized bands is up to 290 meV for 5% of tensile strain.

Since these defects are optically active, the degeneracy splitting could be a way to nondestructively identify the type of defects as well as to measure the applied strain. This should also shift and broaden the optical spectra of defective monolayers at low temperature. Furthermore, due to high resilience of the MLs $MoS_2$ to the mechanical deformations, it is possible to use such splittings as a switch in desired devices. As mid-gap states trap the charge carriers, the shift in the DLs under deformations, in particular isotropic biaxial strains, results in tuning the photoresponsivity and other characteristics of photoconductor devices based on $MoS_2$ monolayers.

### 3.4.3 Electronics: $V_{Mo}$ and vacancy complexes

Now, we turn our attention to the case of molybdenum vacancies. The change in the localized defect states of the MLs $MoS_2$ with $V_{Mo}$ as function of various types of compressive and tensile strain are shown in Figure 3.12(a)–(d). The defect states inside the band gap are labeled as DL1–DL6. The DL1 state is composed of a mixture

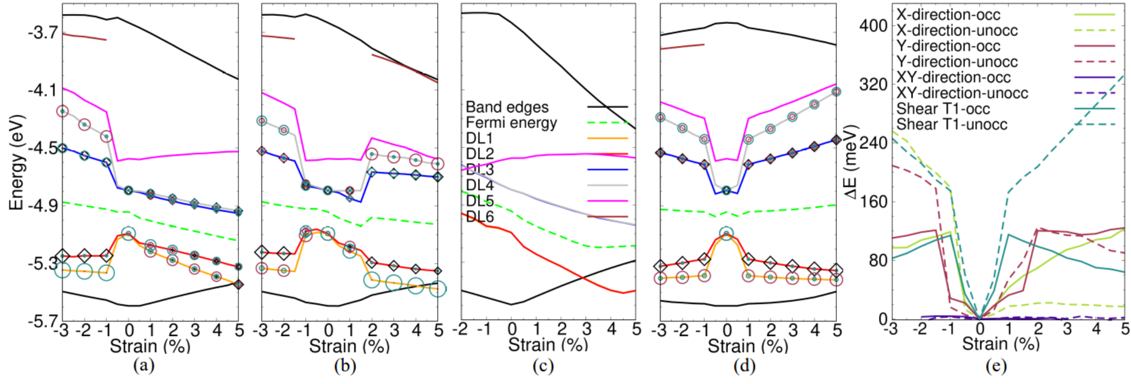


Figure 3.12: (Color online) Evolution of the DLs of the MLs $MoS_2$ with $V_{Mo}$ under strain in a) X-direction, b) Y-direction, c) XY-direction, d) shear T1. The Fermi level and band edges are indicated with green dashed-line and black lines, respectively. The defect states, DL1–DL6, are shown with orange, red, blue, gray, magenta, and brown line, respectively. At zero strain, the DL6 is in resonance with CB. Some of the strain situations shift it down into the band gap. At integer strains. orbital contributions of the deep degenerate DLs are superimposed onto the bands using dark cyan (dark pink) circles for $p_y$ ($p_x$), and black diamonds for a summation of $d$ orbitals. e) The amount of degeneracy splitting of the occupied DL1 and DL2 (solid-line) and unoccupied DL3 and DL4 (dashed-line) levels is plotted in the same interval for all types of strain.

of $p_x$ and $p_y$, while DL2 level is mostly made of $p_x$ orbitals of the six neighboring sulfurs. For the case of DL3 and DL4, $d_{z^2}$ orbital of Mo is mixed with sulfur $p_y$ and $p_x$, respectively, to construct the states. Both DLs also containing a small part from $d_{x^2-y^2}$ and $d_{xy}$ orbitals of the neighboring molybdenums. Nevertheless, summation of the $d$ orbitals ($d_{z^2}+d_{xy}+d_{x^2-y^2}$) contribution to the bands are comparable to $p$ orbitals as deduced from fatbands calculations. These are plotted for $p$ orbitals and for the sum of $d$ orbitals with colored circles and black diamonds, respectively, for degenerate DL2–DL5 bands at integer strains. The non-degenerate DL5 state is mostly composed of $d_{xy}$, $d_{x^2-y^2}$, $p_x$, and $p_y$ orbitals of atoms surrounding the vacancy. The orbital characteristics of the DL2–DL5 bands in defective structures, as well as geometry modifications under strains are also presented in Figures A.5 and A.6 of the supporting information. As shown in Figure 3.12(a),(b),(d), uniaxial and shear T1 strains break the $C_{3v}$ symmetry and remove the degeneracy of the DLs. The hybridization of the orbitals are modified due to changes in the atomic bond lengths around the vacancy position which, in turn, leads to an abrupt shift in

the localized states of DL1–DL5. This will be discussed in detail below. Moreover, except for DL3 and DL4 bands under tensile strain in X-direction, the degeneracy of DLs is removed by applying uniaxial and shear T1 compressions and tensions. Shown in Figure 3.12(c), isotropic biaxial strains shift the degenerate bands, but not separate them. At zero strain, the DL6 band, mainly composed of $d_{x^2-y^2}$ and $d_{xy}$ orbitals, is in resonance with the CB. As the charge density profile around the defect site changes in some strain cases, the DL6 is shifted down into the band gap. The amount of degeneracy splitting of occupied DL1 and DL2 (unoccupied DL3 and DL4) degenerate levels are displayed with solid(dashed)-lines as function of four types of strain in Figure 3.12(e). Of significance, tensile shear T1 breaks the degeneracy of the occupied levels the most and up to 330 meV. The effect of various strains on the DLs of vacancy complexes, $V_{Mo+3S}$, and $V_{Mo+6S}$, are depicted in Figures A.7 and A.8. Shown in this section, as localized states are shifted due to applied strains, we expect a drastic change in the position and height of the peaks in the optical spectra of defective MLs. Accordingly, mechanical deformations can impact the performance of flexible optoelectronic devices based on $MoS_2$ MLs, e.g., single-photon emitters.

The change in the charge density of the MLs $MoS_2$ with $V_{Mo}$ under strain in Y-direction is shown in Figure 3.13. These are plotted at 0.25 $e/\AA^3$. Here, the strain cases of $-2.0\%$ and $+2.5\%$ are presented as an example in Figure 3.13(a) and (c), respectively. At zero strain, the hexagonal symmetry is visible in the density profile of the defective monolayer, displayed in Figure 3.13(b). As compressive or tensile strains applied, the symmetry is broken resulting in two sets of neighboring sulfurs reducing their distance by up to 27.39% (29.34%) for $+2.5\%$ ($-2.0\%$) strain and forming a charge density overlap. The remaining set is simultaneously pushed away from its equilibrium position. As a consequence, stepwise shifts of localized bands are observed in the electronic structure of the $MoS_2$ monolayers with $V_{Mo}$, as shown in Figure 3.12. In case of a single $V_S$, the S atoms in the lower layer prevent a dramatic changes of the geometry and consequently in the charge density, so that no stepwise shifts are observed in the band structure.

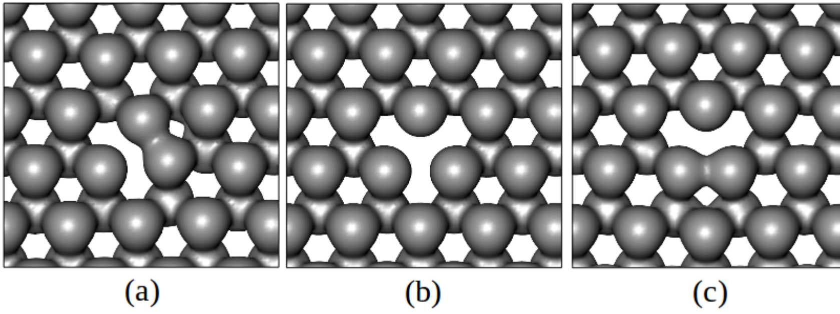


Figure 3.13: (Color online) The change in the charge density of the MLs $MoS_2$ with $V_{Mo}$ under strain in Y-direction for an amount of a) −2.0% b) 0.0%, c) +2.5%. The charge densities are plotted at 0.25 $e/\AA^3$.

## 3.5 Conclusions

We have scrutinized the influence of four different compressive and tensile strains on the electronic and energetic properties of the $MoS_2$ MLs with point defects: $V_S$, $V_{2S-top}$, $V_{2S-par}$, $V_{Mo}$, $V_{Mo+3S}$, and $V_{Mo+6S}$. It was shown that applying strain is a simple yet powerful tool to tune defect properties in MLs $MoS_2$. For example, strain reduced the energy of formation for $V_{Mo}$ and $V_{Mo+3S}$ vacancies. In addition, shear T1 strains lowered the formation of all the point defects. Breaking the symmetry of the monolayers lead to considerable degeneracy splitting of the DLs, ranging from a few meV to more than 400 meV, depending on the vacancy and type of strain. These could be used as a noninvasive method to identify the type of defect. It also allows for a measurement of strain via optical means. The observed stepwise shifts in the localized energy levels of the $MoS_2$ MLs with Mo vacancies under strain are originated from the transition of the charge overlaps between neighboring atoms. The tunability of the photodetector devices properties via strain could stem from the shift in the localized DLs under the applied deformation. Therefore, for flexible optoelectronic devices, the effect of strain on the localized DLs position needs to be considered. Due to the analogy of the properties and geometries of various compounds in the TMD family, we expect a similar response to strain from the intrinsic defects inside their MLs.

# Chapter 4

# Optical Response from Defective TMDs under Strain

The context of this chapter is based on the publication [199].

Monolayers of semiconducting molybdenum (Mo) and tungsten ($W$) dichalcogenide, with direct bandgap, high carrier mobility, and unique optical and mechanical properties, are widely investigated due to their promising applications in electronics and optoelectronics [3, 21, 24, 83]. Experimental measurements have shown that MLs TMDs are highly stable under external mechanical fields compared to conventional bulk semiconductors [50, 96, 97, 101]. At the same time, the electronic and optical properties of such 2D materials are proven to be sensitive to compressive and tensile strain [99–101, 200, 201]. Thus, They have great advantages over conventional semiconductors for applications in transparent and flexible electronic and optoelectronic devices [3, 24, 202, 203].

As discussed in Ch. 1.3, crystalline defects, in particular point vacancies, are always present in the synthetic samples of MLs TMDs. Hence, the defect engineering has been proposed to tune their electronic and optical properties [62,99,100,167,204]. Among these defects, vacancies induce localized defect states deep inside the band gap and close to the VBM as well as the CBM, as presented in Ch. 3 [61, 164, 166, 194, 205]. These midgap states lead to new optical transitions in the spectra, making the defective TMDs monolayers even more interesting for electronic and

optoelectronic devices [17, 47, 83, 171]. Particularly, defect luminescence centers are promising candidates for light-emitting diodes (LEDs) and lasers [47, 203, 206, 207]. In addition, single-photon emission from defect levels (DLs) inside the bandgap of $MoS_2$ and $WSe_2$ monolayers were observed [47, 85, 208, 209]. It has been measured that photo-excited charge carriers can be trapped at the midgap localized levels, which, in turn, leads to a growth of the photocurrent in photodetectors based on MLs $MoS_2$ [88, 89, 210]. We established in Ch. 3, that it is possible to engineer the degenerate DLs of sulfur and molybdenum vacancies inside MLs $MoS_2$ via various mechanical deformations [166]. Hence, scrutinizing the optical properties of crystalline point defects inside MLs TMDs is of great importance both from the application and the fundamental point of view [3, 17, 83, 211].

In this chapter, we will present the effect of three different compressive and tensile strain on the optical properties of $MoS_2$ and $WSe_2$ monolayers, containing transition metal vacancies and vacancy complexes. Using DFT, we analyze the change in absorption spectra of such defective monolayers within the linear response regime. At zero strain, the optical response from defects inside MLs $MoS_2$ are different than vacancies inside MLs $WSe_2$. Applying various mechanical deformations to MLs TMDs modifies the absorption strength, depending on the type of vacancy. Several defect-defect transitions (DDTs) become visible if strain is applied to the defective monolayers.

## 4.1 Computational Details

Semiconducting TMDs monolayers, with hexagonal symmetry, are constructed of a triple X-M-X layer, where the transition metal M is covalently bonded to two chalcogen atoms X, as shown in 1.2 [17, 24, 99]. The focus of this chapter is on two polytypes: $MoS_2$ and $WSe_2$, which are also the experimentally most investigated ones. First-principles calculations are performed using the DFT formalism as implemented in the SIESTA code [134, 174]. The wavefunction for the valance electrons are expanded by a linear combination of double-zeta basis sets with polarization function (DZP). The 4p diffusive orbitals are also included to improve

the characterization of sulfur atoms. The exchange and correlation interactions are described using the generalized gradient approximation (GGA) via the semilocal XC-functional of Perdew-Burke-Ernzerhof (PBE) [126]. The GGA-PBE functional underestimates the bandgap, in particular for the case of TMDs monolayers. However, previous studies have shown that using more sophisticated methods would only lead to similar relative shifts in the band edges and DLs, but do not change the qualitative picture of the defect states within the bandgap [178–180]. Within the Troullier-Martin approach, we have generated a norm-conserving and relativistic pseudopotentials, including core electrons, to describe the valance electrons [175, 176]. Values for the Energy-Shift and the SplitNorm are equal to $0.02Ry$ and 0.16, respectively. Lattice vectors and atomic positions of the equilibrium and strained configurations are optimized using the conjugate-gradient (CG) method. The lower limit for the Hellmann-Feynman forces on each atom is set to 0.01 $eV/\AA$. In order to minimize spurious defect-defect interactions between the defect images in adjacent supercells as much as possible, we calculate the properties of defective $MoS_2$ ($WSe_2$) monolayers for supercell sizes of $6\times6\times1$ to $9\times9\times1$. Our intention is to investigate the properties of isolated defects, rather than the influence of defect concentration. Accordingly, we found that for practical calculations, monolayers of $8\times8\times1$ are found to be a good compromise between accuracy and numerical efforts, for transition metal vacancies as well as for vacancy complexes. On the other hand, this supercell sizes are too small to observe ripple structures due to compressive strain. Normal to the layers, a vacuum of 40 $\AA$ is considered to avoid interactions between adjacent monolayers. The convergency of the total energy is ensured as the difference between two consecutive self-consistent field steps is set to less than $10^{-4}$ $eV$. The Brillouin zone of supercells is sampled by a $5\times5\times1$ k-points in the Monkhorst-Pack scheme to obtain both geometries and electronic properties. The Hartree, exchange, and correlation contribution to the total energy in the real space are calculated using a mesh cut-off of 450 $Ry$. The energy cut-off and k-points are considered converged when total energy differences were below $10^{-4}$ $eV$ and $10^{-5}$ $eV$, respectively. According to previous theoretical studies, the ground state of defective

MLs TMDs is non-magnetic up to more than 5% strain [177, 212–214]. Since we only applied 2% of mechanical deformations to the monolayers, spin-polarization is not considered here. The qualitative picture of the electronic structure of TMDs monolayers containing point defects is preserved in the presence of the spin-orbit coupling (SOC) interactions, even though SOC splits the VBM [178–180]. Due to the fact that inclusion of the SOC has minor influence on the provided analysis and the final conclusions, SOC was neglected in the present work.

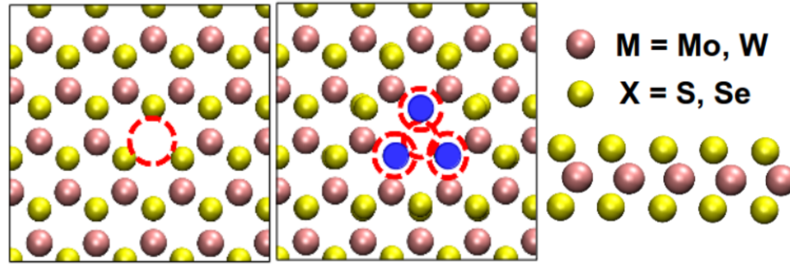


Figure 4.1: (Color online) Left) A monolayer of $MoS_2$ ($WSe_2$) containing the point defects: $V_M$ and $V_{M+3X}$. In every calculation, we only focus on one of these vacancies inside the monolayers. Red dashed-circles denote the position of the missing metal or chalcogens inside the monolayers. Right) side-view of MLs TMDs. Here, $M = Mo, W$, and $X = S, Se$.

Fig. 4.1 shows the position of the point vacancies and their neighboring atoms inside MLs $MoS_2$ (MLs $WSe_2$). In this work, we study $MoS_2$ and $WSe_2$ monolayers with a transition metal vacancy $V_M$ and vacancy complexes $V_{M+3X}$, where $M$ is $Mo$,$W$, and $X$ is $S, Se$. There are computational studies in addition to experimental observation of such vacancies in MLs TMDs samples [17, 61, 82, 164, 192]. It is as well possible to introduce these vacancies by plasma exposure and ion-irradiation [47, 75, 192]. For both defect cases, the $C_{3v}$ symmetry of hexagonal structures are preserved, as shown in Fig. 4.1. The atomic geometries are depicted via the VMD tool [215].

We examine the effect of three different compressive and tensile strain on the optical properties of defective $MoS_2$ ($WSe_2$) monolayers, which are shown in Fig. 4.2. For the purpose of resembling simple deformations, we considered uniaxial strain in X- and Y-direction. There is also an inhomogeneous shear type strain (shear T1)

which maintains the magnitude of in-plane lattice vectors but changes the angle between them. These types of strain are calculated at 2% of compression and 2% of stretching, yet they are below the breaking point of the monolayers [50].

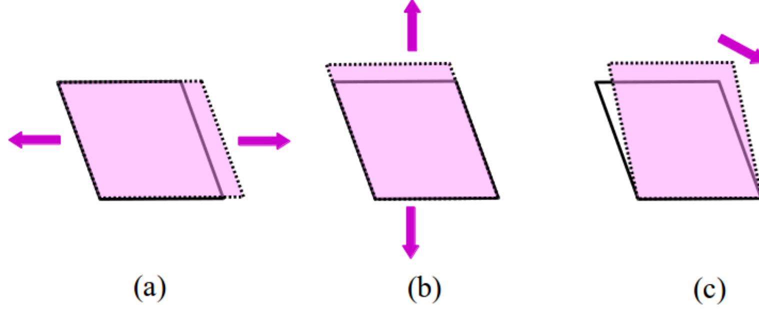


Figure 4.2: (Color online) Schematic view of the uniaxial strain in a) X-direction, and b) Y-direction, c) sheer T1 strain.

Optical properties are calculated using the SIESTA code, in which, the linear response function is used to compute the imaginary part of the dielectric function Im[$\varepsilon(\omega)$] [216]:

$$
\begin{aligned}
Im[\varepsilon(\omega)] =& \frac{1}{4\pi\varepsilon_0}\left(\frac{2\pi e}{m\omega}\right)^2 \sum_{\mathbf{k}} |\mathbf{p}_{c,v}|^2 \\
& \times \delta(E_c(\mathbf{k}) - E_v(\mathbf{k}) - \hbar\omega) \\
& \times \left[f(E_v(\mathbf{k})) - f(E_c(\mathbf{k}))\right].
\end{aligned}
\tag{4.1.1}
$$

Here, $c$ and $v$ subscripts are denoting conduction and valance bands properties, respectively. $E_{c,v}(\mathbf{k})$ are the energy bands with $k$-vector $\mathbf{k}$. Parameter $m$ is the electron mass, $\hbar\omega$ is the photon energy, and $\boldsymbol{p}_{c,v}$ is the momentum operator. An optical mesh size and broadening of 25×25×1 and 0.02 $eV$ are chosen, respectively.

We focus here on the dipole transition strength of various inter DL transitions under the influence of different types of strain. Although including the many-body effects modify the electronic and optical properties of TMDs monolayers, there are strong experimental evidence, as in Refs. [47,77,217,218], of peaks at energies below the bandgap. These peaks were identified to be corresponding to DDTs. Considering such effects into the calculations does not change the characteristics of optically active and inactive states. Besides, in order to avoid defect-defect interactions, we study a very large system size, for which it is prohibitive to include a description

of the level of many-body perturbation theory (like a GW0+BSE approach). Thus, we neglect the electron-hole Coulomb interactions in this work. As we consider only linear optical absorption and hence probing the states which would be available for excitation, geometry relaxation via the excitation process does not play a role here, in contrast to studies based on photoluminescence, where actual electrons are excited.

We investigate the effect of various strain situations on the optical properties of $MoS_2$ and $WSe_2$ monolayers containing transition metal vacancies, $V_M$, as well as vacancy complexes, $V_{M+3X}$. The presence of such vacancies in the synthesized samples have been observed in atomic-resolution measurements and studied via theoretical methods [61, 82, 164, 192]. Moreover, these defects can also be introduced to the TMDs monolayers by post processing techniques, such as plasma exposure and ion-irradiation [47, 75, 192].

## 4.2 Electronic Structure

A schematic of the electronic structure of these defective monolayers is displayed in Fig. 4.3. Here, we show the VBM, the CBM, and the Fermi energy ($E_F$) as well as the DLs. The occupied DLs are named with letters A to C, while the unoccupied DLs are labeled with numbers 1 to 6. Based on first-principles DFT analysis, there are five DLs in the band structure of $MoS_2$ ($WSe_2$) monolayers with a single transition metal vacancy, $V_{Mo}$ ($V_W$), as shown in Fig. 4.3a. Two occupied double-degenerate levels are labeled A&B, while 1&2 are the double-degenerate unoccupied DLs and 3 is a non-degenerate state. Structures with vacancy complexes of $V_{Mo+3S}$ and $V_{W+3Se}$ are shown in Fig. 4.1. Figure 4.3b shows a schematic of their electronic structure; B&C are double-degenerate occupied DLs. There are also six unoccupied localized states, a triple-degenerate 1&2&3, a double-degenerate 4&5, and a non-degenerate level 6. These results are in accordance with previous reports [61, 164, 166, 194, 205].

Accordingly, DDTs are indicated corresponding to the levels involved in the transitions: A1,A2,. . . ,B1,. . . ,C6. The orbital characteristics of the localized states and VBM are scrutinized to identify the DDTs in the absorption spectra of such

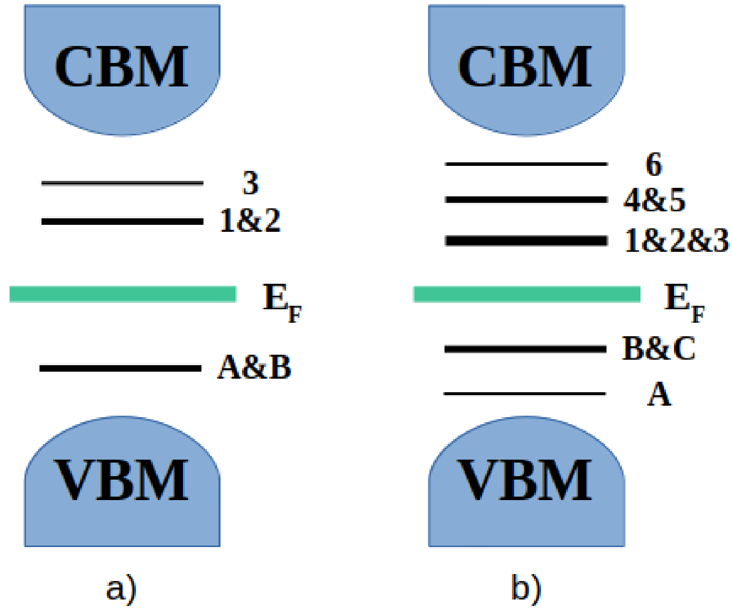


Figure 4.3: (Color online) Schematic of the electronic structure of the defective MLs $MoS_2$ (MLs $WSe_2$) with a) $V_{Mo}$ ($V_W$), b) $V_{Mo+3S}$ ($V_{W+3Se}$). Valance and conduction band edges, VBM and CBM, are shown along with the Fermi energy ($E_F$). Occupied (unoccupied) DLs in the bandgap are labeled with letters (numbers). A&B, B&C, 1&2, 4&5 are double-degenerate states. 1&2&3 are triple-degenerate DLs.

monolayers. Major contributions are originated from the $d$ orbitals of transition metals ($Mo, W$) and $p$ orbitals of chalcogens ($S, Se$). In the case of simple metal vacancy in MLs $MoS_2$, VBM is built from $4d_{xy}$,$4d_{x^2-y^2}$ ($4d_{XY}$) and $3p_x$,$3p_y$ orbitals, while a mixture of $4d_{z^2}$,$4d_{XY}$ and $3p_z$ orbitals are mainly involved in the VBM of system with $V_{Mo+3S}$. For $V_W$ in MLs $WSe_2$, $5d_{z^2}$ and $5d_{xy}$,$5d_{x^2-y^2}$ ($5d_{XY}$) orbitals are hybridized with $4p_x$,$4p_y$,$4p_z$ ($4p$) orbitals to construct the VBM; however, only $5d_{z^2}$,$5d_{XY}$ orbitals contribute to the VBM when $V_{W+3Se}$ is present in monolayers. These findings are in line with previous studies [187,188,194]. Orbital characteristics of the DLs for each vacancy are presented in corresponding sections.

## 4.3 Optical Properties

We investigate the effect of various types of strain on the absorption spectra of these defective monolayers within the linear response regime. Peaks at energies below the

bandgap indicate the presence of optically active DLs within the electronic structure of defective monolayers.

## Simple transition metal vacancy

The optical properties of MLs $MoS_2$ with $V_{Mo}$ vacancy are shown in Fig. 4.4. We study the in-plane imaginary part of the dielectric function ($\mathrm{Im}[\varepsilon_{\parallel}(\omega)]$) for the unstrained case (black lines) and under various types of compressive (blue lines) and tensile (red lines) strain. Orbitals $4d_{xz}$,$4d_{yz}$ and $3p_x$,$3p_y$,$3p_z$ ($3p$) are main compo-

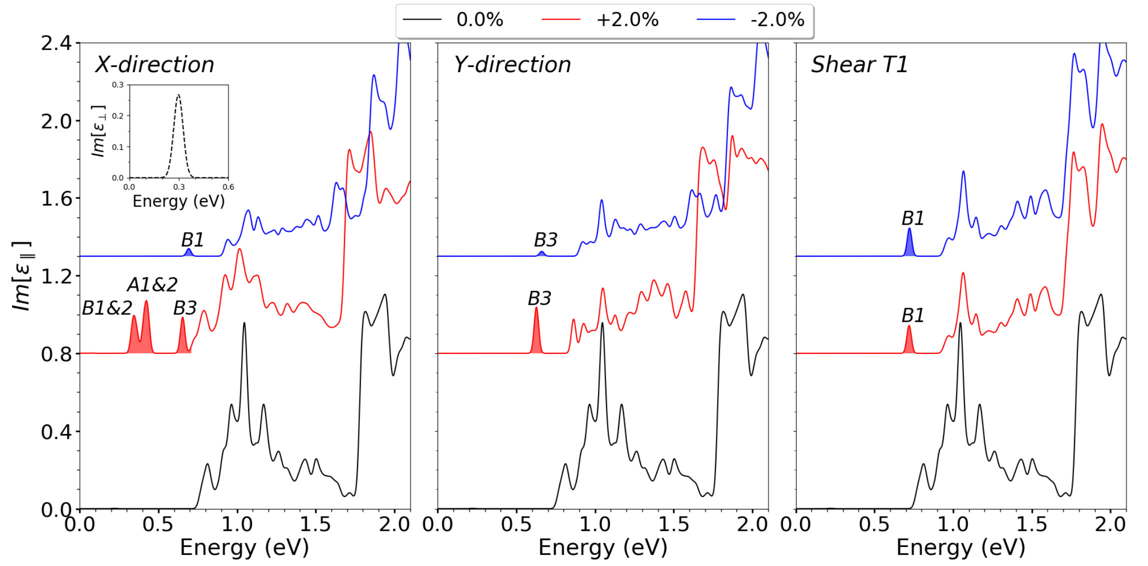


Figure 4.4: (Color online) The absorption spectra for MLs $MoS_2$ with $V_{Mo}$ at zero strain (black lines) and under 2% compressive (blue lines) and 2% tensile (red lines) strain. The inset is the out-of-plane response of the defective monolayer. From left to right, the plots represent the effect of strain in X-direction, Y-direction, and shear T1 strain. For each strain case, DDTs are labeled and highlighted with shaded colors.

nents of two occupied states A and B, while unoccupied DLs are constructed from a mixture of $4d_{z^2}$,$4d_{XY}$ and $3p$ orbitals. Hence, corresponding elements of the dipole matrix have zero value, leading to optically inactive DDTs in the in-plane spectra (See black curves in Fig. 4.4). Two peaks with the lowest energy arise due to the transition between the VBM and unoccupied double-degenerate DLs. In the inset of Fig. 4.4, the out-of-plane absorption spectra ($\mathrm{Im}[\varepsilon_{\perp}(\omega)]$) is plotted for unstrained

defective monolayers. In contrast to the case of in-plane spectra, DDTs A1&2 and B1&2 are visible here. These states are mainly composed of surrounding atomic orbitals with components outside of the XY-plane. Fig. 4.4 also shows the effect of various strain situations on the spectra of $V_{Mo}$ in MLs $MoS_2$, where DDTs are indicated with shaded colors. In the case of 2% stretching in X-direction, three peaks can be observed corresponding to DDTs B1&2, A1&2, and B3. Orbital characteristics of occupied level A (B) is modified and now containing a mixture of $4d_{xy}$ and $3p$ ($4d_{x^2-y^2}$,$4d_{z^2}$ and $3p$) orbitals. The first two unoccupied DLs remain intact under this strain, however, the third unoccupied localized state is now mainly constructed of $4d_{z^2}$,$4d_{XY}$ and $3p$ orbitals. Modifications of the electronic structure under 2% of compressive strain leads to observation of B1 transition, where both states are originated from a combination of $4d_{z^2}$,$4d_{XY}$ and $3p$ orbitals. When uniaxial compressive or tensile strain in Y-direction is applied, B3 transition becomes visible in the in-plane response of the dielectric function, where mostly $4d_{z^2}$,$4d_{XY}$ and $3p$ orbitals are contributing to both DLs. In general, the absorption strength of DDTs is larger for uniaxial tensile than compressive strain. The influence of compressive and tensile shear T1 strain on the optical response of $MoS_2$ monolayers with $V_{Mo}$ are similar and lead to a peak stemming from B1 transition. Here, $4d_{z^2}$,$4d_{XY}$ and $3p$ orbitals are mainly contributing to these states. When changes in orbital composition are not mentioned, this means orbitals contributing to other states remain unchanged under strain.

Looking at Fig. 4.4, as uniaxial and inhomogeneous shear T1 strain are applied, transitions between occupied and unoccupied DLs become optically active. This is due to the change in the hybridization of orbitals surrounding the vacancy. This also stems from breaking the hexagonal symmetry of the defective MLs $MoS_2$ via strain, thus removing the degeneracy of the localized states [166, 172, 193]. It can also be explained via the modification of the geometrical and electronic properties as function of applied strain, which is highlighted in Fig. 4.5. In this figure, the charge density of the $MoS_2$ monolayers with $V_{Mo}$ are shown for (a) 0.0% and b) +2.0% strain in X-direction at isovalue of 0.095 $e/\AA^3$. Atoms around the vacancy

are labeled with $A$, $B$, and $C$. At zero strain, symmetric structure of the monolayer is untouched and the distance between the neighboring atoms is 3.238$\AA$ for MLs $MoS_2$ with $V_{Mo}$ and 3.176$\AA$ for pristine geometry. When 2.0% of tensile strain in X-direction is applied, the $AC$ and $BC$ distances are 3.262$\AA$ and 3.192$\AA$ for defective monolayer and pristine structure, respectively. However, since atoms at $A$ and $B$ positions are along the strain direction, the $AB$ distance for the case of Mo vacancy in MLs $MoS_2$ has been increased by 5.8% to 3.426$\AA$, which is much larger than for pristine structure with the expected 2.0% increase to 3.240$\AA$. This geometry modification is responsible for the changes in optical properties for such defective monolayers, shown in Fig. 4.4.

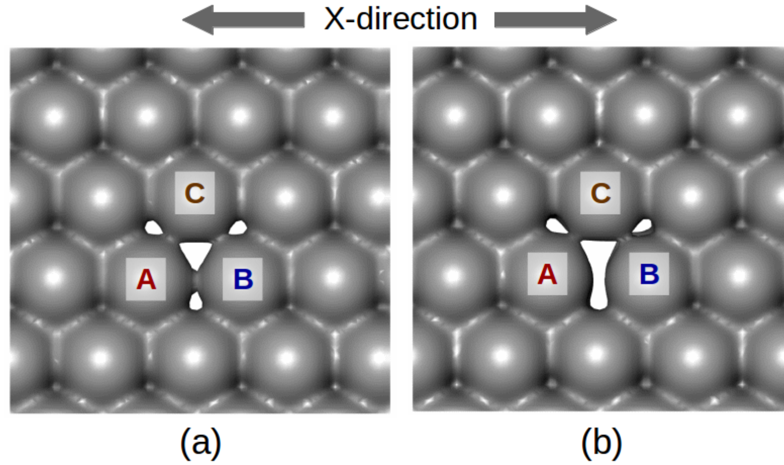


Figure 4.5: (Color online) The change in the charge density of the $MoS_2$ monolayers containing $V_{Mo}$ under strain in X-direction for an amount of a) 0.0% and b) +2.0%. These are plotted at 0.095 $e/\AA^3$. Atoms around the vacancy are labeled with $A$, $B$, and $C$.

The presence of a simple metal vacancy, $V_W$, in MLs $WSe_2$ results in localized states inside the bandgap. In Fig. 4.6, the optical spectra are shown (black lines) for the unstrained defective structure. Two peaks corresponding to transitions A1&2,B1&2 and A3,B3 are highlighted. The fact that DDTs are visible in the spectra is in explicit contrast to the case of $Mo$ vacancy in MLs $MoS_2$ at zero strain. This translates into differences in orbital characteristics of the DLs in two materials. For the case of $V_W$ in MLs $WSe_2$, two occupied localized states A and B are constructed of $5d$ orbitals mixing with $4p$ orbitals, and three unoccupied DLs

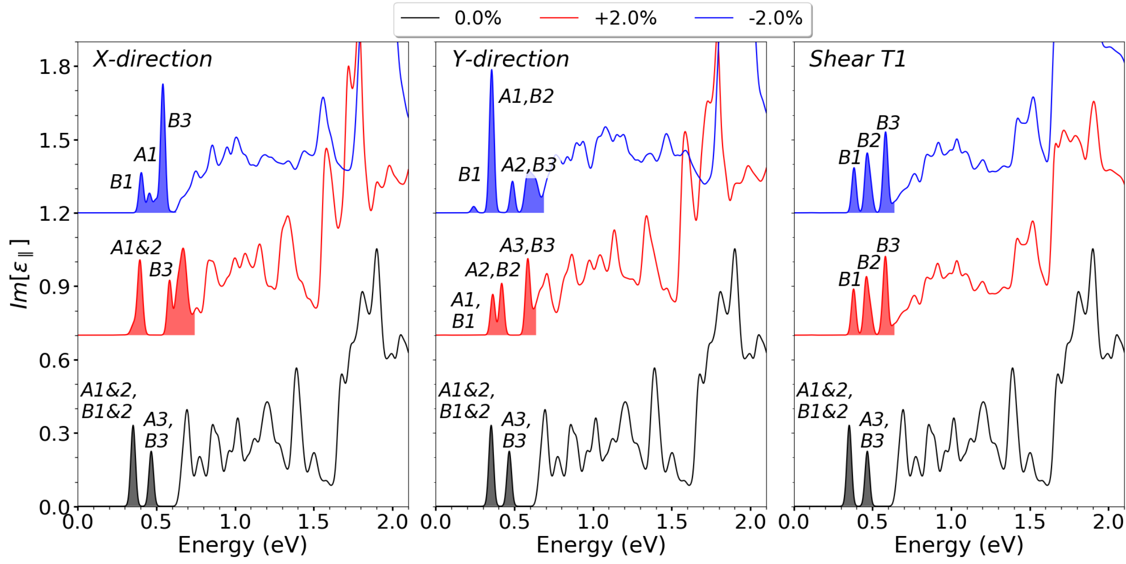


Figure 4.6: (Color online) The absorption spectra for MLs $WSe_2$ with $V_W$ at zero strain (black lines) and under 2% compressive (blue lines) and 2% tensile (red lines) strain. From left to right, the plots represent the effect of strain in X-direction, Y-direction, and shear T1 strain. For each strain case, DDTs are labeled and highlighted with shaded colors.

have major contributions from $5d_{z^2}$,$5d_{XY}$ and $4p$ orbitals. On the other hand, localized states in unstrained MLs $MoS_2$ with $V_{Mo}$ are mainly constructed from $4d_{xz}$,$4d_{yz}$ and $3p$ orbitals. Comparing Figs. 4.4 and 4.6, it can be seen that dipole matrix elements are larger for $V_W$ than $V_{Mo}$. In Fig. 4.6, the effect of various strain situations on the absorption spectra of these defective $WSe_2$ monolayers are displayed where DDTs are labeled and shown with shaded colors. In the case of 2% uniaxial tensile strain in X-direction, although the orbital characteristics of the unoccupied states remain unchanged, states A and B are now dominated with $5d_{xz}$,$5_{dxy}$,$5d_{yz}$,$5d_{z^2}$,$4p$ and $5d_{z^2}$,$5d_{XY}$,$4p$ orbitals, respectively. Peaks corresponding to DDTs A1&2 and B3 are visible. Applying 2% of compressive strain in X-direction, three transitions B1, A1, and B3 can be observed. Here, there are modifications only in the major orbitals contributing to the states A and B as well as the first unoccupied level. When uniaxial strain in Y-direction are applied, hybridization of the occupied DLs A and B are changed, while the main orbital components of the unoccupied states stay unaffected. Thus, the degeneracy breaking leads to the observation of A1–3

and B1–3 transitions in the spectra. When 2% compressive or tensile shear T1 strain is applied to MLs $WSe_2$ with $V_W$, orbitals $5d_{z^2}$,$5d_{XY}$ and $4p$ have the largest coefficients in wavefunction expansion of states A and B. The first unoccupied DL is now constructed of $5d$ and $4p$ orbitals. Peaks corresponding to DDTs B1, B2, and B3 are shown in Fig. 4.6.

## Vacancy complexes

In synthesized samples as well as during post processing mechanisms, vacancy complexes, i.e. $V_{Mo+3S}$ and $V_{W+3Se}$, are more likely to be present than single transition metal vacancies, according to previous studies [164,166,172,188,193]. This is particularly important when generating vacancies for single-photon emitters at selective sites [47, 75]. We investigate the optical properties of $MoS_2$ and $WSe_2$ monolayers containing vacancy complexes at zero strain and under various mechanical deformations. Such studies are also of interest for the production of flexible optoelectronic devices. In comparison to the case of $V_{Mo}$ ($V_W$) vacancies in MLs $MoS_2$ (MLs $WSe_2$), out-of-plane optical responses are negligible for monolayers with the complex vacancies, $V_{Mo+3S}$ ($V_{W+3Se}$).

Shown in Fig. 4.7, the in-plane imaginary part of the dielectric function is plotted for $MoS_2$ monolayers with $V_{Mo+3S}$. In this figure, optically active DDTs are highlighted. Their dipole matrix elements are noticeably much larger than peaks in the absorption spectra of MLs $MoS_2$ with $V_{Mo}$ (See Fig. 4.4). This could be an evidence that in ion-irradiation processes, single photons are emitted from vacancy complexes rather than simple transition metal vacancies. The peak with the highest absorption comes from DDTs B1&2&3, and C1&2&3, i.e. transitions from double-degenerate DLs B&C to triple-degenerate unoccupied localized states 1&2&3. The other peak is originated from transitions A1&2&3, B4&5, and C4&5. Unoccupied DLs 4&5 are double-degenerate. At zero strain, all the DLs are mainly composed of $4d$ and $3p$ orbitals. Even though the degeneracy of DLs is broken via applying uniaxial and inhomogeneous strain, orbital contributions to the localized states remain untouched. Except for the case of tensile strain in X- and Y-direction, where the

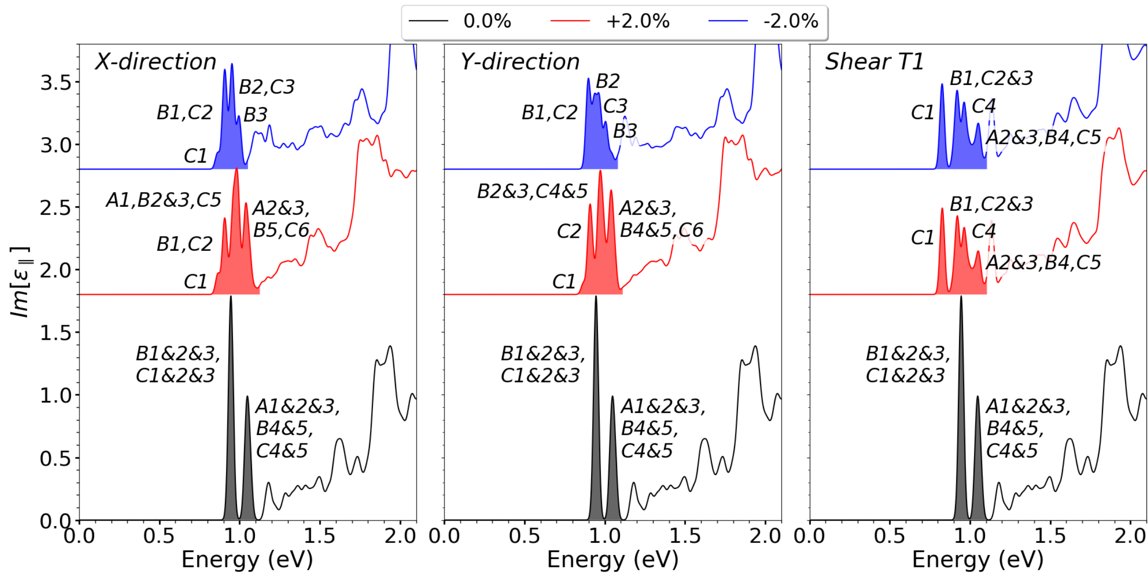


Figure 4.7: (Color online) The absorption spectra for MLs $MoS_2$ with $V_{Mo+3S}$ at zero strain (black lines) and under 2% compressive (blue lines) and 2% tensile (red lines) strain. From left to right, the plots represent the effect of strain in X-direction, Y-direction, and shear T1 strain. For each strain case, DDTs are highlighted with shaded colors and their labels.

occupied state A is mostly constructed from a mixture of $4d$ and $3p_y$,$3p_z$ orbitals. As monolayers are stretched or compressed by 2% of uniaxial strain, four optically active DDTs can be seen in the spectra. These are indicated in Fig. 4.7 with their corresponding labels. Applying 2% of either compressive or tensile shear T1 strain leads to identical modifications in the optical spectra, i.e. four peaks corresponding to transitions C1, B1,C2&3, C4, and A2&3,B4,C5 can be observed. All being said, the absorption strength of DDTs, consequently their brightness, is reduced by a factor of almost two (three) via uniaxial (inhomogeneous shear T1) strain.

The absorption spectra of unstrained MLs $WSe_2$ with the vacancy complex $V_{W+3Se}$ is shown with black curves in Fig. 4.8. Two sets of optically active DDTs can be seen, i.e. B1&2&3,C1&2&3 and A1&2&3. It should be noted that B&C are double-degenerate occupied states, and 1&2&3 are triple-degenerate unoccupied levels. Interestingly, the dipole matrix elements of the first peak is about five times larger than the intensity of the peaks in the optical response of MLs $WSe_2$ with $V_W$ (See Fig. 4.6). This outcome emphasizes our hypothesis that in ion-irradiated

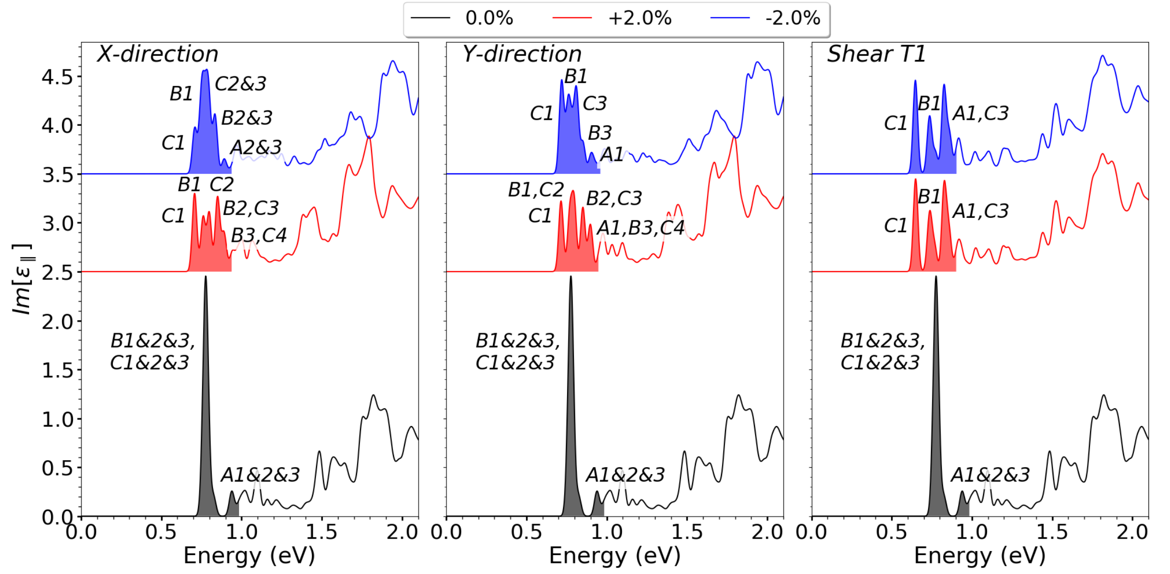


Figure 4.8: (Color online) The absorption spectra for MLs $WSe_2$ with $V_{W+3Se}$ at zero strain (black lines) and under 2% compressive (blue lines) and 2% tensile (red lines) strain. From left to right, the plots represent the effect of strain in X-direction, Y-direction, and shear T1 strain. For each strain case, DDTs are highlighted with shaded colors and their labels.

samples, the main source of single-photon emissions could be vacancy complexes rather than single transition metal vacancies. At zero strain, $5d$ orbitals of $W$ have the largest coefficients in wavefunction expansion of state A, which stays untouched as all strain situations are applied. Orbital characteristics of the occupied DLs B and C are mainly a combination of $5d$ and $4p$ orbitals. In the case of the unstrained defective monolayers, major contributions to all unoccupied DLs come from $5d$ and $4p$ orbitals which remain the same under any types of strain. In Fig. 4.8, blue (red) lines show the impact of various compressive (tensile) strain on the optical spectra of the defective monolayers, where DDTs are indicated with shaded colors and corresponding labels. When 2% of compression or tensile uniaxial strain is applied to the defective MLs $WSe_2$, degeneracy of the occupied DLs B and C is removed due to changes in their orbital characteristics. This leads to the observation of several optically active DDTs in the spectra, as indicated in Fig. 4.8. Shear T1 compressive and tensile strain result in analogous modifications to the absorption spectra of MLs $WSe_2$ with $V_{W+3Se}$. Three peaks corresponding to DDTs C1, B1 and A1,C3

can be seen in the spectra. Here, only the orbital components of the occupied state B is changed to a mixture of $5d$ and $4p_x$,$4p_y$ orbitals. It can be observed in Fig. 4.8 that the absorption strength are decreased by a factor of almost three as uniaxial or inhomogeneous strain are applied, for both compressing and stretching.

## 4.4 Conclusions

In this chapter, we have investigated the optical properties of MLs $MoS_2$ and MLs $WSe_2$ containing point vacancies; $V_M$ and $V_{M+3X}$. At zero strain, it is shown that DDTs are visible in the in-plane spectra for $V_W$ in MLs $WSe_2$ in contrast to MLs $MoS_2$ with $V_{Mo}$. According to our study, dipole matrix elements of peaks originated from DDTs are significantly larger for the case of the vacancy complexes than the simple vacancies.

The effect of two uniaxial and an inhomogeneous shear T1 strain on the optical properties of defective TMDs monolayers is studied. Interestingly, DDTs in MLs $MoS_2$ with $V_{Mo}$ become visible in the in-plane spectra as mechanical deformations are applied. We have traced this behavior back to the change in the hybridization of atomic orbitals surrounding the vacancy at the defect site. Depending on the type of strain, the absorption strength of MLs TMDs with vacancy complexes has been reduced by a factor of two to three. Thus, the brightness of the spectra from samples with point vacancies could be reduced via strain. Applying strain allows to tune the optical properties of monolayers in a controllable way. Our findings will be beneficial to the application of MLs $MoS_2$ in optoelectronic, flexible, and piezoelectric devices as well as heterostructure setups.

# Chapter 5

# Devices Based on 2D Lateral Heterojunctions

The context of this chapter is based on the publication [219].

Among the developing family of two-dimensional (2D) materials, transition metal dichalcogenides (TMDs) provide one of the most diverse electronic properties including topological insulators, semiconductors, (semi)metals and superconductors [220–222]. Noticeably, such a difference in the electronic structure of TMDs correlates with their structural configurations, called phases [223]. Monolayers of $MoS_2$ in H-phase, with trigonal prismatic coordination of metal atoms is a semiconducting material [43, 224], while T-phase with octahedral coordination shows metallic character. The H-phase monolayer is reported to be a promising material for field-effect transistors (FETs) with small-scale channel lengths and negligible current leakage [43, 224]. The atomically thin nature of MLs $MoS_2$ maximizes the gate tunability in ultrashort-channel transistors. Besides, the direct source-drain tunneling in $MoS_2$-based devices are minimized because of the high effective mass and large bandgap [43, 224]. The contact resistance and high Schottky barrier between metallic electrode and semiconducting region limit the performance and potential of these devices [225–228].

Recent experiments have already shown controlled transitions from one phase to another via external stimuli such as electron beam [36], ion intercalation [34],

or laser irradiation [229]. The coexistence of 1T-phase and 2H-phase of $MoS_2$ has also been observed in high resolution scanning transmission electron microscope (STEM) imaging [41]. These phase-engineered 2D materials with minimum variations in atomic structure and uniform stoichiometry not only demonstrate rich physical behavior but also open up new avenues for the design of electronic devices. The fabrication of lateral metallic/semiconducting heterostructures has been suggested as a practical method to minimize the contact resistance at the interface between 2D semiconductors and metal electrodes. In particular, the formation of covalent bonds between the two phases can introduce paths for carriers to travel across the interfaces, thus, the Schottky barrier and contact resistance are reduced [45,225,230,231]. It has also been demonstrated that 1T-phase engineered electrodes in $MoS_2$ based electronic devices would generate ohmic contacts and, as a result, improve electrical characteristics [230, 232].

So far, several theoretical studies have reported the transport properties of phase-engineered devices based on TMDs monolayers including $MoS_2$ based lateral junctions [33, 35, 44, 45, 230, 233, 234]. In most of these studies, it is assumed that two phases have a perfect crystalline structure and connected via an atomically sharp and defect-free interface. However, structural defects are always present in the synthetic samples due to the thermal equilibrium and the kinetics of processing which impose significant effects on their properties [17, 60, 61, 91, 194, 235]

Apart from intrinsic defects, the local phase transitions induced by electron beam irradiation may give rise to the formation of point defects, in particular at the interface of the two phases. [47, 75, 79, 82, 170, 217, 218, 236]. Defects can also be intentionally introduced during the post-growth stage via ion bombardment, plasma treatment, vacuum annealing, or chemical etching. [47, 75, 79, 82, 170, 217, 218, 236]. Indeed, the theoretical and experimental results showed that the presence of sulfur vacancies can decrease the energy difference between the H and T phases and eventually stabilize the 1T phase in $MoS_2$ monolayer [237, 238]. The presence of point defects in semiconducting $MoS_2$ monolayers leads to the observation of the localized states in their electronic structure, which act as short-ranged scattering

centers for charge carriers [17,166,194,235]. Hence, defects were found to deteriorate the mobility of the fabricated devices [23, 55, 81]. It was also shown that sulfur line vacancies in $MoS_2$ can behave like pseudo-ballistic wire for electron transport [239].

Here, transport properties of devices based on MLs $MoS_2$, containing various point vacancies and antisites at the interface between metallic and semiconducting phases, are the subject of the present study. Our systematic investigations show significant improvements in the current, as molybdenum vacancy and vacancy complexes are created at the interfaces of two phases. These findings render defect engineering as an efficient route to further improve the performance of the devices based on the lateral heterojunctions formed from TMDs.

## 5.1 Computational Details

Density-functional theory calculations were performed using numerical atomic orbitals (NAOs) basis sets as implemented in SIESTA code [134, 174]. The norm-conserving pseudopotentials, including the effect of core electrons, are employed, which were obtained using the Troullier-Martin method [175, 176]. The GGA-PBE functional is used to describe the exchange and correlation interactions [126].

In the optimization calculations, the Brillouin zone (BZ) of supercells was sampled using a 9×1×3 Monkhorst-Pack grid. In the electronic and transport calculations, 5 and 29 k-points were used, respectively, along the transverse direction. The conjugate-gradients method was applied to optimize the lattice vectors and atomic positions of all the structures and interfaces. The geometries were considered relaxed when the Hellman-Feynman forces on each atom became smaller than 10 meV/Å. The energy cut-off of 450 Ry is used in the framework of the real-space grid techniques to obtain Hartree, exchange, and correlation energies. The Split-Norm was set to 0.16 and the Energy-Shift of 0.02 Ry was chosen to determine the confinement radii. The total energy convergency criteria ($\triangle E_{tot}$) is chosen to be $10^{-5}$eV for k-points and $10^{-4}$eV for energy cut-off. When the difference between two consecutive steps was less than $10^{-4}$eV, the total energies in self-consistent field (SCF) cycles are considered converging.

The electron transport calculations were performed using NEGF techniques, explained in details in Ch. 2.2, as implemented in TranSIESTA and TBtrans [153,154]. The same basis sets as for the electronic calculations, namely SZP, are employed for the transport calculations. The current through the heterophase junction under a finite bias voltage is calculated within the Landauer formula, which its derivation is presented in Ch. 2.2.1, [144]

$$I = \frac{2e}{h} \int Trace \left[ G_C^{\dagger}(E)\Gamma_R(E)G_C(E)\Gamma_L(E) \right] (f_L(E) - f_R(E))\, dE. \quad (5.1.1)$$

Where $G_C^{\dagger}(E)$ and $G_C(E)$ are the retarded and advanced Green's functions of the channel region. The effect of left (L) and right (R) electrodes are projected onto the scattering region via their corresponding self-energies, $\Gamma_L(E)$ and $\Gamma_R(E)$. The Fermi distribution of $f_L(E)$ and $f_R(E)$ represent the available states for electrons in the left and right electrodes. In order to calculate the self-energies of the electrodes, we have used 65 k-points along the transport direction (Z-axis) and 5 k-points transverse to the transport direction (X-axis) to simulate a semi-infinite metallic electrode. The transport calculations are performed at 300 K.

## 5.2 1T-2H Interface

Previous theoretical studies have shown no difference or a difference of 0.63% between the lattice constant of the T- and H- phase of $MoS_2$ monolayers [25, 164, 224, 240, 241]. Therefore, the same lattice parameters, namely 3.176Å, are used for both phases. Such a phase transition can be seen as the collective displacement of sulfur atoms while the stoichiometry of the materials is preserved. Band structures for 2H- and 1T-phase of $MoS_2$ are plotted in Fig.5.1. It can be clearly observed that 2H-$MoS_2$ is a semiconductor with a bandgap of 1.73 eV, while 1T-$MoS_2$ has a metallic character. We have compared our calculated band gap for perfect 2H-$MoS_2$ monolayer with the values reported at different levels of theories, as listed in Table B.1 [25, 164, 242]. These shows an agreement with previous theoretical reports at

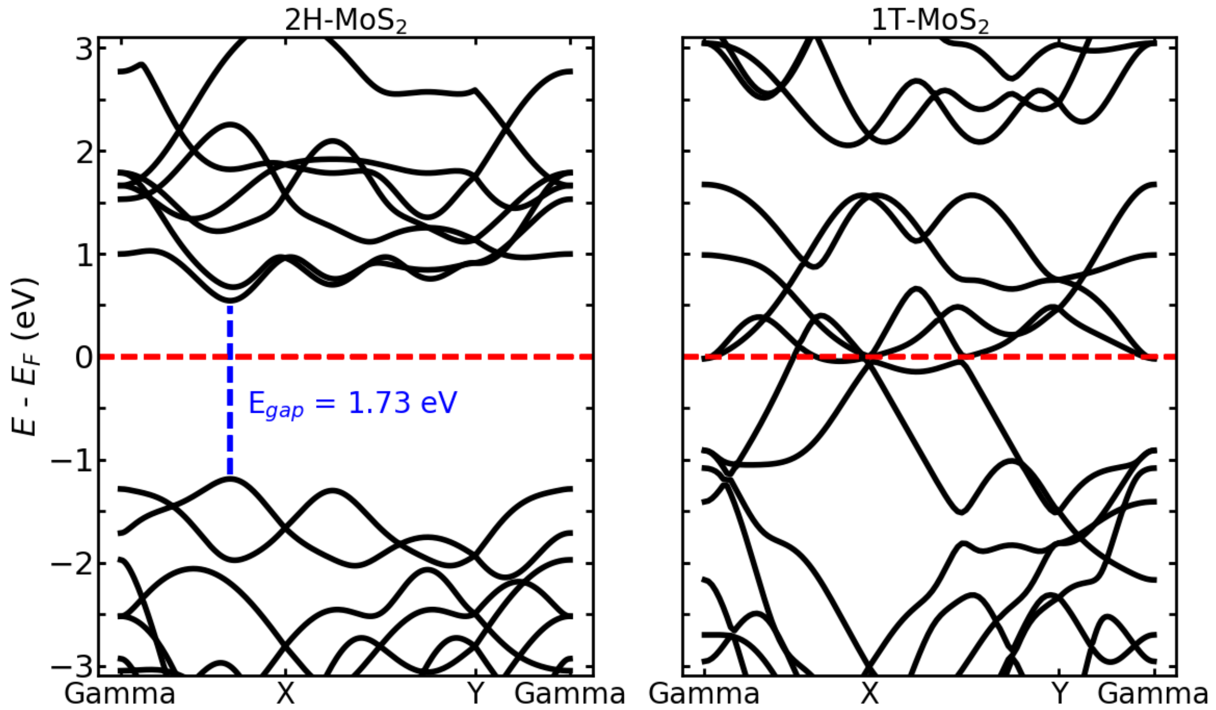


Figure 5.1: Band structures are plotted for **left)** Semiconductor (2H) and **right)** metallic (1T) phases of $MoS_2$ monolayers. Energies are shifted according to the Fermi energy. There is a bandgap of 1.73 eV for the case of the semiconducting monolayers while 1T-$MoS_2$ has a clear metallic character.

the same level of theory [25, 164, 224, 240, 241]. In the case of defective systems, it has been known that more advanced methods like GW approximation would only lead to shifts in the band edges and defect levels in the same direction, but do not change the qualitative picture of the defect states within the bandgap and their relative position to the VBM and CBM (see Refs. [178–180]). Therefore, it is expected that these methods would only affect the range of the applied voltage in transport calculations and the provided analysis remain intact.

Depending on the edge orientation of MLs-$MoS_2$, armchair and zigzag interfaces can be realized. The armchair interfaces have been shown to be most stable against buckling [33, 45]. They are also energetically more favorable than connecting the zigzag terminated edges in the sulfur-rich limit [33, 44]. The recent theoretical study on 1T/2H-$MoS_2$ devices showed that the conductivity of the armchair edges is higher than the zigzag interfaces due to the presence of metallic Mo zigzag chains along

the transport direction [45]. Accordingly, we consider the armchair interface in the present study. The constructed lateral heterostructures with armchair edges are optimized. It should be noted that the optimization could not transform 1T into the 2H phase but induce some distortions, indicating the activation barrier for the phase transformation is higher than the relaxation of the boundary.

In order to create Schottky contacts at the interfaces, 2H-$MoS_2$ is sandwiched between two metal electrodes of 1T-$MoS_2$, as shown in Fig. 5.2. The whole set up consists of 21 layers of semiconducting $MoS_2$ and 8 layers of metallic $MoS_2$ at both sides.

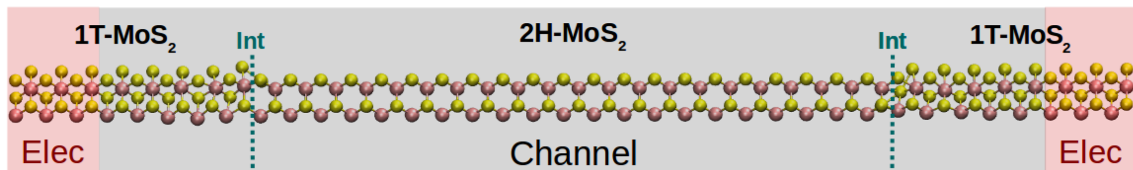


Figure 5.2: Schematic of a device based on metallic (1T) and Semiconductor (2H) phases of $MoS_2$ monolayers. Left and right interfaces are shown with green dashed-lines. Electrodes in this work are the part of the 1T-$MoS_2$ that are highlighted under the shaded red box.

Having perfect electrodes is a key concept within the NEGF framework in order to obtain physically reliable results. Our electrode calculations have revealed that 3 layers of 1T-phase of $MoS_2$ (highlighted with red boxes in Fig. 5.2) are sufficient to simulate the bulk-like behaviour of the contacts. Another five layers of 1T-$MoS_2$ are added to 2H-$MoS_2$ to construct the channel region (highlighted with a gray box in Fig. 5.2) which minimizes the effect of geometry relaxations at the interfaces on the perfect electrodes.

## 5.3 Schematic of 1T/2H-$MoS_2$ Devices

The 1T/2H heterojunction device in the present study has a length of 117.50 Å along the transport direction (Z axis) and width of 22.00 Å in the transverse direction (X axis). The size of the channel part is 98.46 Å corresponding to 31 unit cells of $MoS_2$. The channel length is long enough to avoid artificial interactions between the two

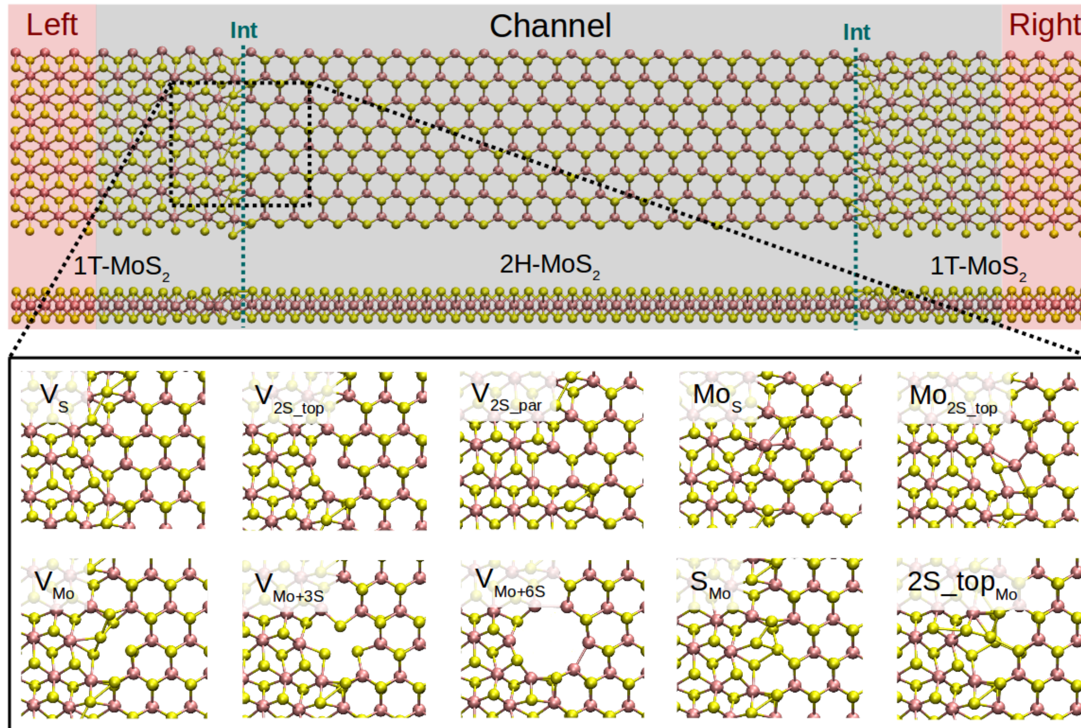


Figure 5.3: Upper: Schematic of the T-H heterophase junction of $MoS_2$ monolayer. Electrodes (only 1T-$MoS_2$) and channel region (a combination of 1T- and 2H-$MoS_2$) are highlighted with shaded red and black, respectively. The interfaces are indicated with green dashed-lines. All the structures are considered periodic along the axis transverse to the transport direction. Lower: Optimized structures of the point defects at the left interface of the devices are shown. Only defects at the left electrode are shown here. The complete defective devices are shown in Fig. B.1 in the supplementary information.

electrodes. Also, it includes small adjacent portions of the 1T phase as buffer layers to provide a computationally convenient configuration for calculating self-energies at the boundaries [243]. The periodic boundary conditions were applied along the axis transverse to the transport direction. A vacuum layer of 50 Å normal to the monolayers was considered, which prevents interactions between adjacent supercells.

Several junctions composed of 1T and 2H of MLs $MoS_2$ are considered without defects (perfect) and when containing point defects in the phase boundaries, as shown in Fig. 5.3. Here, we considered only the high-symmetry cases where similar defects are created at both interfaces. In Fig. B.1 of the supplementary information, the structure of the whole device is shown. We consider 10 types of point defects,

most of which were observed in experiments [47,61,79,82,170,192] and their stability were analyzed by DFT calculations [17, 164, 166, 236]. Our main objective is to present the difference between the effect of such defects in transport prop- erties of 1H pristine phases and 1T-2H heterostructures. Hence, complex defects containing antisite aggregated with another type of defect, as mentioned in Ref. [244], are neglected in this study. We look at a sulfur and a molybdenum vacancy, $V_S$ and $V_{Mo}$, a double sulfur vacancy from upper and bottom layers $V_{2S-top}$, and the case of removing two atoms from the upper sulfur layer and parallel to the interface, $V_{2S-par}$. Besides, vacancy complexes of molybdenum and three sulfurs ($V_{Mo+3S}$) and six sulfurs ($V_{Mo+6S}$) are also studied. Four antisites are also considered: $Mo_S$, $Mo_{2S-top}$, $S_{Mo}$, and $2S-top_{Mo}$. We consider only the high-symmetry cases where similar defects are created at both interfaces, hence, rectifying effect will not appear.

In this study, all defects are assumed to be in their charge-neutral states. The previous report on the charged defects in semiconducting 2H-$MoS_2$ revealed that when the Fermi level is close to the conduction band (n-type doping), both $V_S$ and $V_{Mo}$ are likely to assume negative charge states [164]. However, because of

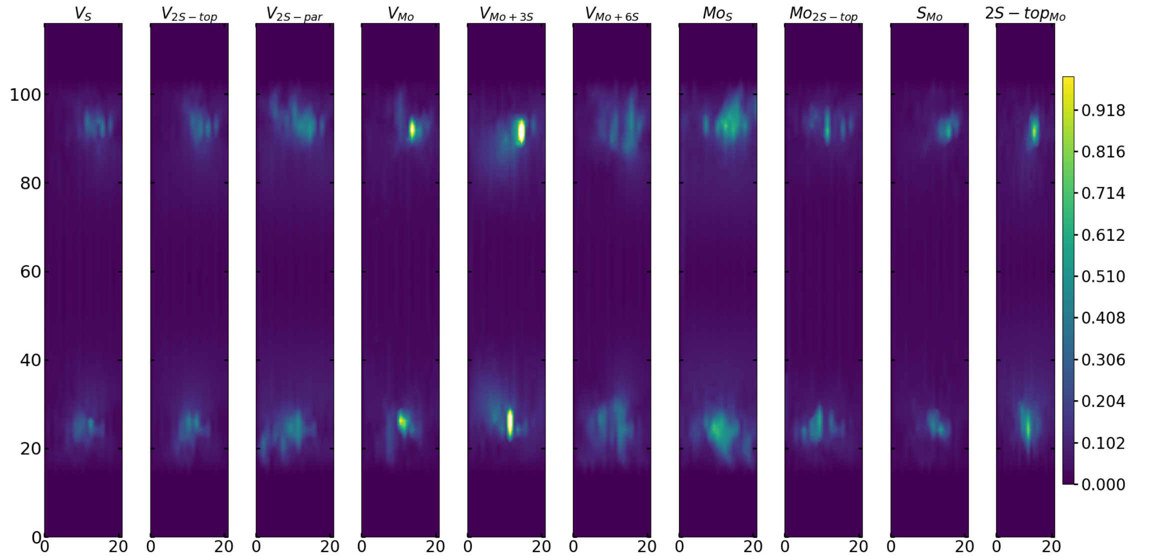


Figure 5.4: Displacement map of the defective structures. Sum of displacements in the three axis are calculated.

the metallic character of 1T-$MoS_2$, defects in the 1T-2H heterophase junction are

considered only in their neutral state as the extra charge migrates to the 1T phase.

As a result of defects in the phase boundary, the atomic network can be subjected to strain. Fig. 5.4 shows the strain map, which is specified as the total displacements in all three axes as compared to the perfect interface. It shows the effect of induced local strain on the device properties. It can be seen that the largest change in the atomic positions are for the case of $V_{Mo+3S}$ at the interfaces while removing two Sulfurs, from top and bottom layers, $V_{2S-top}$, induce the smallest displacements into the phase boundary.

## 5.4 Transport Through Lateral Heterojunctions

In this section, we analyze the effect of interfacial defects on the transport properties of $MoS_2$ lateral heterojunctions, based on transmission, current and LDOS.

### 5.4.1 Sulfur vacancies

First, we present the electronic and transport properties of T-H heterophase junction containing interfacial sulfur vacancies; $V_S$, $V_{2S-top}$, and $V_{2S-par}$. In Fig. 5.5, local density of states (LDOS) on the atoms at the left interface of such devices are plotted at Bias $= 0.00\,V$ and Bias $= 1.40\,V$. In the following, the term "interface" is used for a part of the device, which consists of atoms from one layer of 1T-$MoS_2$ and one layer of 2H-$MoS_2$. Due to the electronic states from T phase, the band gap in LDOS is narrower than that for pristine 2H phase of $MoS_2$. Comparing the two figures, there is a shift in the energy, corresponding to half of the applied voltage.

The presence of defects introduces new states close to the Fermi level and increases electron density at the interface, which is mainly contributed by metal $d$ orbitals. It is evident that defect-associated states are more pronounced in the case of $V_{2s-par}$ where the electron density is enhanced in the vicinity of the Fermi level, including a peak at -0.2 eV. The results showed that other types of sulfur vacancies have a negligible impact on the electronic structure around the Fermi energy. It should be noted that the sulfur vacancies in 2H-$MoS_2$ monolayers act as scattering

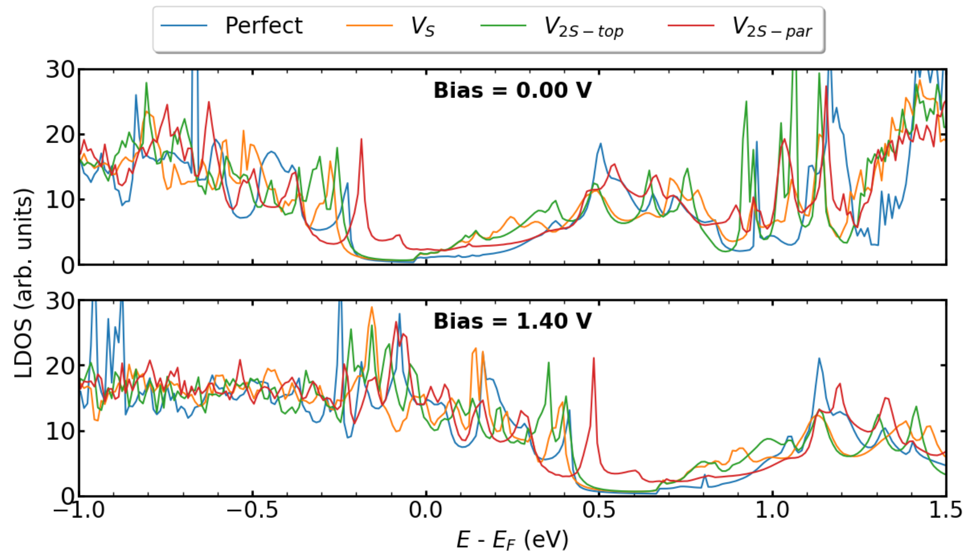


Figure 5.5: (Color online) LDOS at the left interface for devices without defects (Perfect) and with sulfur vacancies, $V_S$, $V_{2S-top}$, and $V_{2S-par}$, are plotted at Bias equal to $0.00\,V$ and $1.40\,V$. Energies are shifted with respect to their corresponding Fermi energy. In the case where two sulfurs from the top layer and parallel to the interface, $V_{2S-par}$, are removed, midgap states can be observed in LDOS. Other defects have a negligible impact on the LDOS around the Fermi energy.

centers and consequently diminish the transport properties [17, 166, 194, 235].

In order to elaborate the electron conduction dependency on the geometry of contact between the T and the H phases, transmission spectra for the junction without and with interfacial defects at two Bias, 0.00 and $1.40\,V$, are shown in Fig. 5.6a and 5.6b, respectively. Corresponding to the band gap of 2H-$MoS_2$, there is no transmission at zero bias within an energy range of $1.7\,eV$ around the Fermi level. A comparison between perfect interface and those containing sulfur vacancies shows a growth in transmission probability, suggesting the contribution of defect states in electrical transport. Specifically, the transmission coefficients close to the valance band edge can be increased to almost two times for the case of $V_{2S-par}$ vacancy. The IV characteristics of the studied T-H heterophase junction are shown in Fig. 5.6c. The junction displays a non-linear current-voltage similar to the characteristics of a resonant tunneling diode. The energy mismatch between the Fermi energy of the metallic 1T electrodes and the lowest unoccupied levels of the 2H phase causes the presence of zero current and the need for threshold voltage to produce finite current

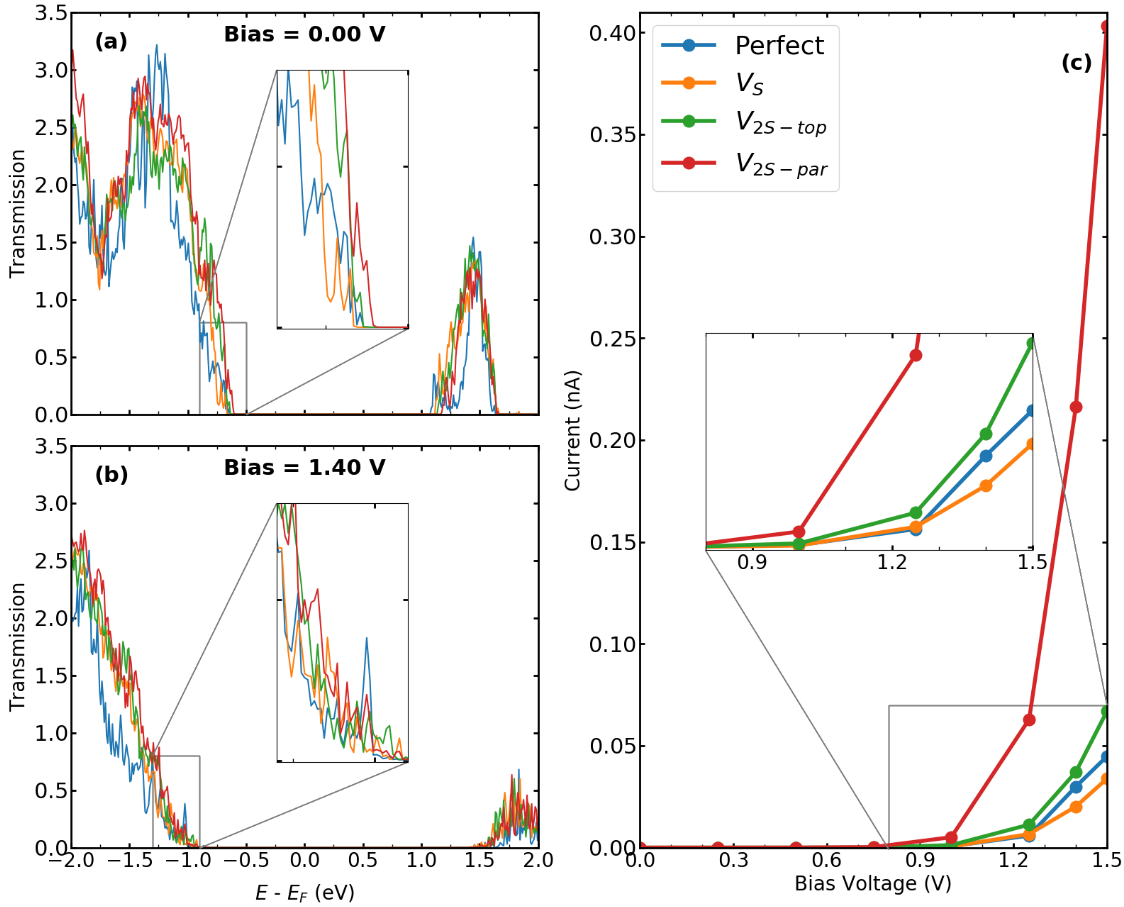


Figure 5.6: (Color online) Transmission spectra for T-H heterophase junction of $MoS_2$ monolayer containing various sulfur vacancies at both interfaces at a) Bias = $0.00\,V$ and b) Bias = $1.40\,V$. Energies are shifted with respect to their corresponding Fermi energy. The insets show how the electronic transmission channels change at the top of the valance band. c) I-V characteristics for the same devices. The inset shows the current around the threshold voltage.

flow through the junction. The value of threshold voltage was reduced from 1.0 V for the perfect interface to 0.75V for the interface with divacancy. The appearance of defect-associated resonant states in the transmission spectra within the voltage window changes the current through the system, leading to an increase by an order of magnitude, when $V_{2S-par}$ vacancy is present at the interfaces, as shown in Fig. 5.6c.

### 5.4.2 Molybdenum vacancies and vacancy complexes

We then turn to the calculation of the electronic and transport properties of the T-H heterophase junction when molybdenum vacancy, $V_{Mo}$, and vacancy complexes $V_{Mo+3S}$ and $V_{Mo+6S}$ are present at the interface. The LDOS of the interface is shown in Fig. 5.7 at Bias = $0.00\,V$ and Bias = $1.40\,V$. Here, the applied bias has shifted the energies. The electronic structure of the interfaces with a single Mo vacancy varies more than that of a single sulfur vacancy. In the case of larger point defects, i.e. $V_{Mo+6S}$, the electronic structure shows several resonant states around the Fermi level which are mainly formed by Mo $4d$ states. The defect-induced changes in the electronic structure affect the carrier injection through the junction. The transmission function (Fig. 5.8b&c) at the top of the valance band shows a significant enhancement when vacancies are introduced into the interfaces. Accordingly, the current is increased by up to three orders of magnitude in comparison to the perfect interface. This is due to an enhancement of carrier occupations near the Fermi level, which leads to an increase in the transmission spectrum. The projected local density of states (shown in Fig. B.4 of supplementary information) also indicates more electronic states at the interface with Mo vacancy, generating a strong electron transmission at energies around -0.5 eV. This leads to an increase in the electron conduction within the corresponding bias window (Fig. 5.8b&c). A similar effect was recently reported on the dependence of transmission on the geometry of interface in $MoS_2$ based heterojunctions [245]. The interfaces with $V_{Mo+6S}$ vacancy demonstrate a threshold voltage of $\approx$ 0.5 V, half of that for a perfect interface.

To further investigate the transport behaviour at the interface, we also plot the vector current for perfect systems and devices with $V_{Mo}$ at both interfaces (Fig. B.2). Vector current displays the direction and the amount of current, coming from the left or right electrode, projected on each atom and at a specific energy channel. While the perfect interface shows dominant current scattering at the T-H boundary for low bias voltages, e.g. V=-0.5 V, the currents are delocalized in the channel region with $V_{Mo}$ at the interface, suggesting that electrons have been well transmitted from electrodes to the channel region.

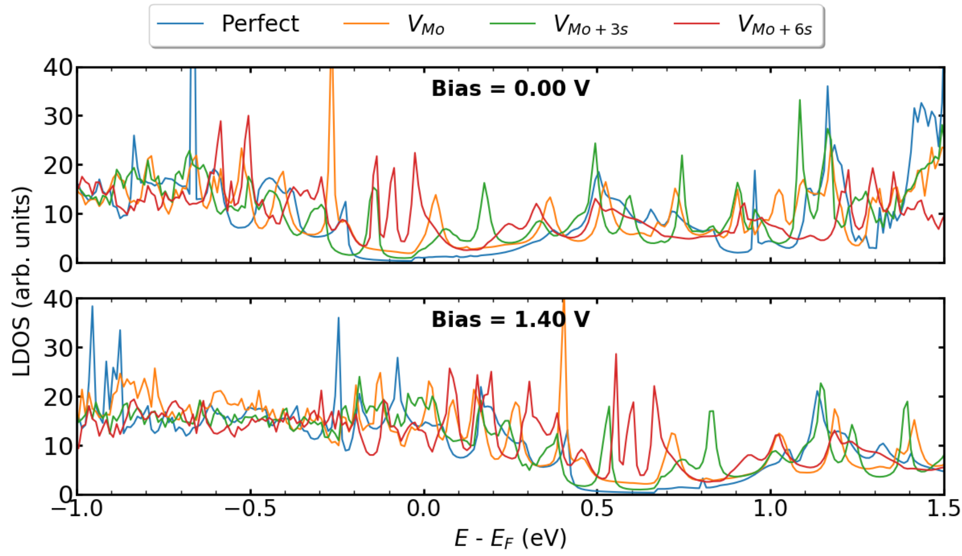


Figure 5.7: (Color online) LDOS at the left interface for devices without defects (Perfect) and with molybdenum vacancy, $V_{Mo}$, and vacancy complexes as $V_{Mo+3S}$, $V_{Mo+6S}$, are plotted at Bias equal to $0.00\,V$ and $1.40\,V$. Energies are shifted with respect to their corresponding Fermi energy. These defects strongly modify the LDOS around the Fermi energy, leading to a significant improvement in the IV characteristics.

We have also studied the influence of defect concentrations on the transport properties through the interfaces. Here, , we fixed the length of the channel but varied its width, including the interfaces with a single $V_{Mo}$. Fig. 5.9 shows the difference in the conductance through devices ($\Delta G = G_{defect} - G_{perfect}$) as a function of the devices' areas. It is evident that the conductance reduces with decreasing the defect concentration approaching the value of the perfect interface for zero-defect density. Variation of channel widths has two different effects on the transport properties: On one hand, the number of transport channels increases with the width of the channel. On the other hand, for a constant number of defect sites, increasing the channel width leads to a decrease in the carrier densities around the Fermi Level. The former effect is canceled out by subtracting the conductivity of the system from the corresponding one with the pristine interface. As a result, for wider channels (lower concentrations), the increase in electrical conductivity is linearly reduced.

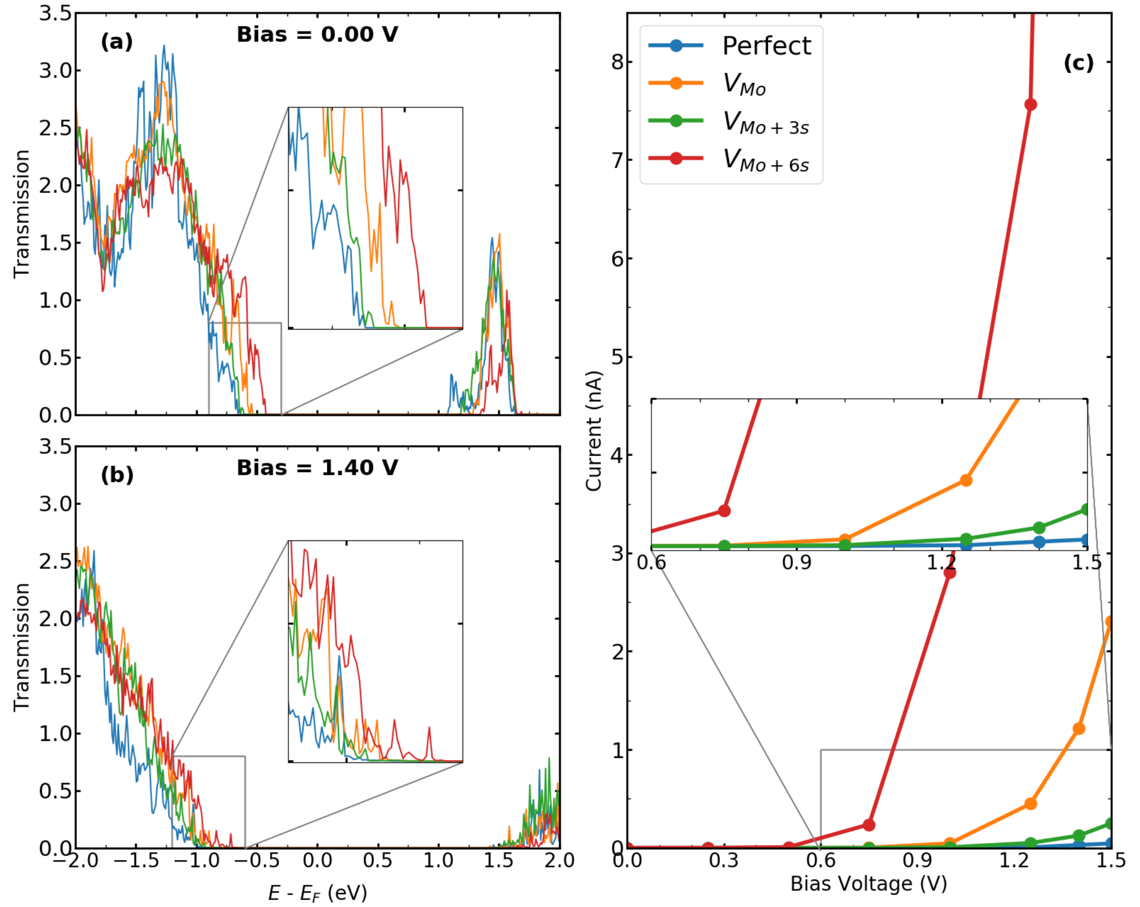


Figure 5.8: (Color online) Transmission spectra for T-H heterophase junction of $MoS_2$ monolayer containing molybdenum vacancy, $V_{Mo}$, and vacancy complexes as $V_{Mo+3S}$ and $V_{Mo+6S}$ at both interfaces at a) Bias $= 0.00\,V$ and b) Bias $= 1.40\,V$. Energies are shifted with respect to their corresponding Fermi energy. The insets show how the electronic transmission channels change at the top of the valance band. c) I-V characteristics for the same devices. The inset shows the current around the threshold voltage. When such point defects are present at the devices interfaces, the current has been enhanced by up to three orders of magnitude.

### 5.4.3 Antisites

Because vacancy and antisite are both high electron-scattering centers, their presence in TMDs can impair sample mobility [195]. We further investigate the influence of antisites defects, such as $Mo_S$, $Mo_{2S-top}$, $S_{Mo}$, and $2S-top_{Mo}$, at the interfaces of T-H heterophase junctions. Among all the considered antisites, the situation where molybdenum vacancy is substituted with two sulfurs ($2S-top_{Mo}$) provides the most pronounced defect associated states at the valence band edge (Fig. 5.10).

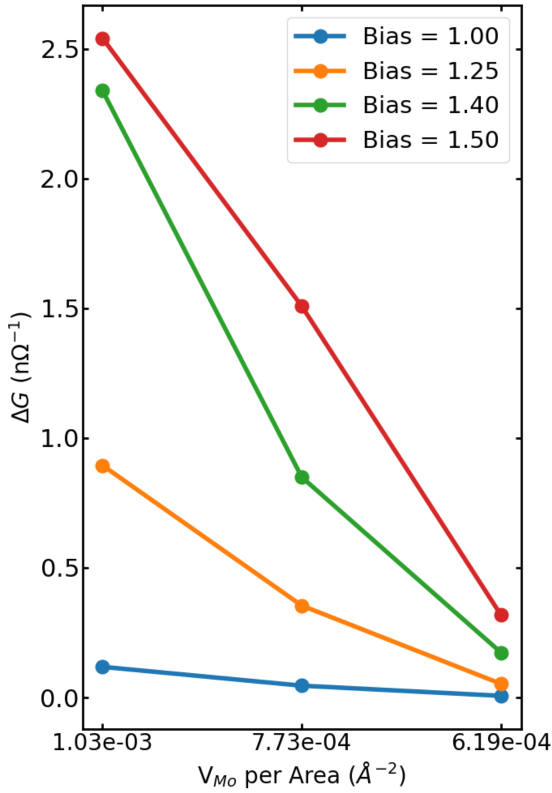


Figure 5.9: (Color online) Difference in the conductance through perfect systems and device with $V_{Mo}$ ($\Delta G = G_{defect} - G_{perfect}$) as function of the device's area at different bias voltages. Since number of vacancies is the same for all cases, it is also a function of the defect density. It is true that more transport channels are added to wider devices, however, at the same time defect density is reduced, hence, decreasing the current through defective devices. Thus, conductance difference is approaching to zero, as the system gets wider.

When compared with the Mo vacancy, the defect states are more localized and originated mainly from hybridization between the $Mo_d$-$S_p$ orbitals. The contributing orbitals to the LDOS at the left interface are shown in Fig. B.3 in the supplementary information.

In Fig. 5.11a,b, transmission spectra for phase-engineered devices based on MLs $MoS_2$, containing various substitutions, are displayed at Bias $= 0.00\,\&\,1.40\,V$. Fig. 5.11c shows the corresponding IV characteristics as a function of bias voltages up to $1.50V$. When vacancies are substituted with sulfur or molybdenum atoms, the current stays in the same order as for the device with perfect interfaces. Only for the case of $2S - top_{Mo}$, current has been slightly increased due to the presence of midgap defect states observed in LDOS and the enhancement in the transmission probabilities. It's also worth noting that, in contrast to the case of perfect interfaces, the presence of antisite defects inevitably results in more phonon scattering channels, which may be beneficial in lowering lattice thermal conductivity.

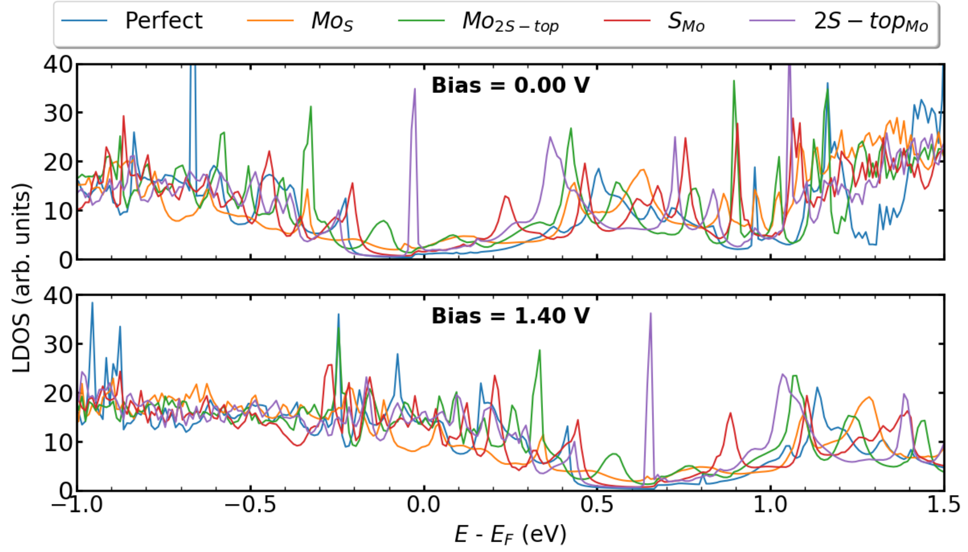


Figure 5.10: (Color online) LDOS at the left interface for devices without defects (Perfect) and with substitutions; $Mo_S$, $Mo_{2S-top}$, $S_{Mo}$, $2S-top_{Mo}$, are plotted at Bias equal to $0.00\,V$ and $1.40\,V$. Energies are shifted with respect to their corresponding Fermi energy. These defects, except the case of $2S-top_{Mo}$, have slightly affected the LDOS around the Fermi energy.

## 5.5 Conclusions

We have investigated the transport properties of charge carriers through devices based on metallic (1T) and Semiconductor (2H) phases of $MoS_2$ monolayers. Various point defects are present at both interfaces: $V_S$, $V_{2S-top}$, $V_{2S-par}$, $V_{Mo}$, $V_{Mo+3S}$, $V_{Mo+6S}$, $Mo_S$, $Mo_{2S-top}$, $S_{Mo}$, and $2S-top_{Mo}$. The first-principles simulations and NEGF technique are used to compute the LDOS, transmission curves, and IV characteristics of perfect and defective devices under bias in the range of $0.00\,V$ till $1.50\,V$. Our systematic study shows that defects at the interfaces provide the opportunity for further improvement of the transport properties of such devices. More notably, we found that transport properties are enhanced in the presence of energetically favorable intrinsic point defects. In contrast to the scattering character of defects in 2H-phase $MoS_2$, at the interface, they lead to emergence of resonant states close to the Fermi level, thereby giving rise to the enhanced current flow. In particular, creating a molybdenum vacancy induces defect midgap states in the LDOS and improves the transport characteristics, which, in turn, leads to an increase

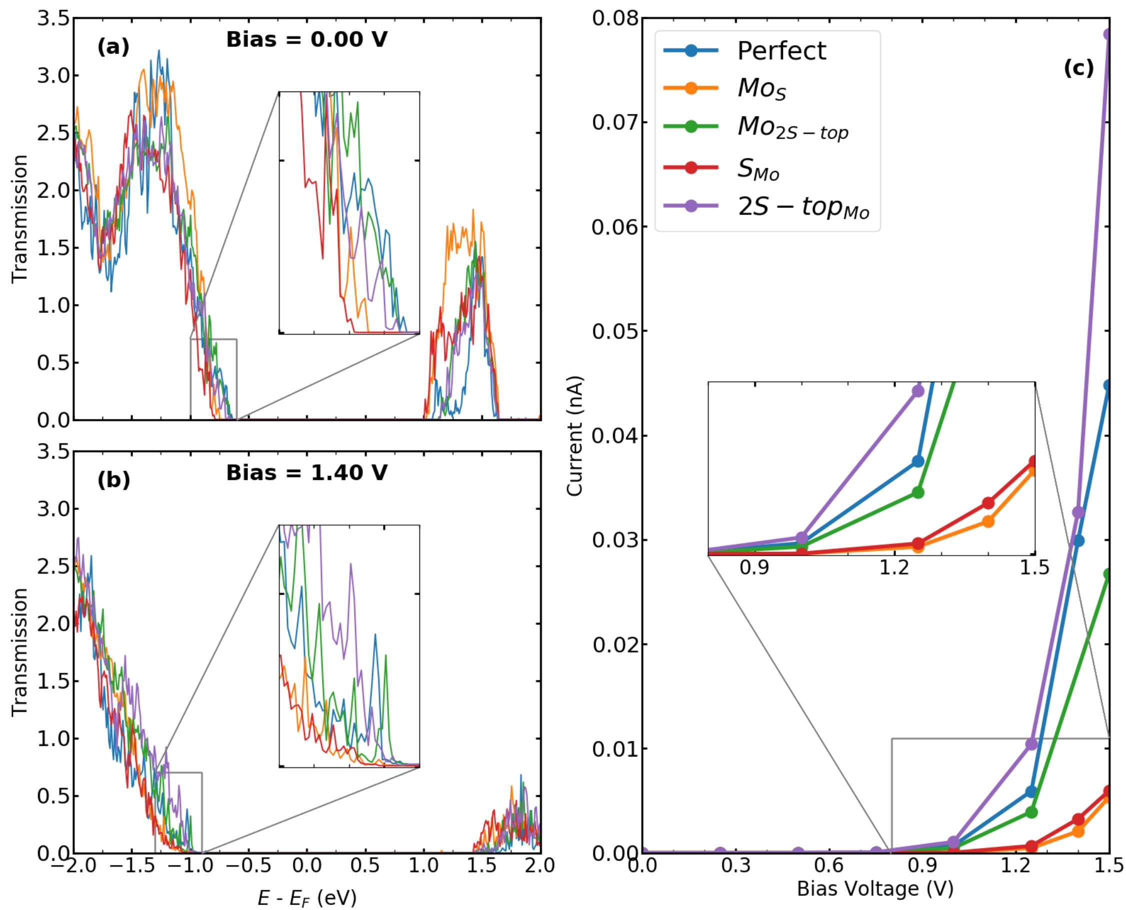


Figure 5.11: (Color online) Transmission spectra for T-H heterophase junction of $MoS_2$ monolayer containing various substitutions; $Mo_S$, $Mo_{2S-top}$, $S_{Mo}$, $2S-top_{Mo}$, at both interfaces at a) Bias = $0.00\,V$ and b) Bias = $1.40\,V$. Energies are shifted with respect to their corresponding Fermi energy. The insets show the change in the electronic transmission channels at the top of the valance band. c) I-V characteristics for the same devices. The inset shows the current around the threshold voltage. In defective systems, currents are in the same range as or even smaller than the current in the device with perfect interfaces.

in the current up to two orders of magnitude. The knowledge developed in this study could pave the way for the promising applications of lateral heterojunctions of 1T/2H $MoS_2$ monolayers in field effect devices.

# Chapter 6

# Concluding Remarks

## 6.1 Summary

The objective of the work presented in this thesis was on the one side to scrutinize the effect of mechanical deformations on the electronic and optical properties of the defective TMDs monolayers. On the other hand, we studied the transport properties of charge carriers through the 1T/2H-$MoS_2$ heterojunctions in the existence of point vacancies and antisite vacancies.

In chapter 3, using first-principles calculations, we have scrutinized the influence of four different compressive and tensile strains on the electronic and energetic properties of MLs $MoS_2$ with point defects: $V_S$, $V_{2S-top}$, $V_{2S-par}$, $V_{Mo}$, $V_{Mo+3S}$, and $V_{Mo+6S}$. We have shown that applying strain is a simple yet powerful tool to tune defect properties in such monolayers, e.g. changing significantly the formation energies. As an example, strain reduced the energy of formation for $V_{Mo}$ and $V_{Mo+3S}$ vacancies. In addition, shear T1 strains lowered the formation of all the point defects. Breaking the symmetry of the monolayers lead to considerable degeneracy splitting of the DLs, ranging from a few meV to more than 400 meV, depending on the vacancy and type of strain. These could be used as a noninvasive method to identify the type of defect. Since MLs $MoS_2$ are robust to mechanical deformations, such splittings could be used as switches in devices. It also allows for a measurement of strain via optical means. We observed stepwise shifts in the localized energy lev-

els of $MoS_2$ monolayers with Mo vacancies under strain. These shifts are shown to originate from the transition of the charge overlaps between neighboring atoms. The localized DLs, acting as trapping sites for photo-excited charge carriers. Hence, we concluded that the observed tunability of the properties of the photodetector devices via strain could stem from the shift in these DLs under the applied deformation. Therefore, for flexible optoelectronic devices, the effect of strain on the localized DLs position needs to be considered.

Chapter 4 discussed the investigation of the optical properties of MLs $MoS_2$ and MLs $WSe_2$ containing point vacancies; $V_M$ and $V_{M+3X}$. The optical spectra were calculated using DFT and within the linear response regime. At zero strain, we show that DDTs are visible in the in-plane spectra for $V_W$ in MLs $WSe_2$ in contrast to the case of MLs $MoS_2$ with $V_{Mo}$. According to our study, dipole matrix elements of peaks originated from DDTs are significantly larger for the vacancy complexes than the simple vacancies. In this chapter, the effect of two uniaxial and an inhomogeneous shear T1 strain on the optical properties of defective TMDs monolayers was also studied. Interestingly, DDTs in MLs $MoS_2$ with $V_{Mo}$ become visible in the in-plane spectra as mechanical deformations are applied. We have traced this behavior back to the change in the hybridization of atomic orbitals surrounding the vacancy at the defect site. Depending on the type of strain, the absorption strength of MLs TMDs with vacancy complexes has been reduced by a factor of two to three. Thus, the brightness of the spectra from samples with point vacancies could be reduced via strain.

In chapter 5, we studied the charge transport properties of devices based on metallic and Semiconductor phases of $MoS_2$ monlayers. Systems with various point defects at both interfaces of the 1T/2H-$MoS_2$ heterojunctions were investigated: $V_S$, $V_{2S-top}$, $V_{2S-par}$, $V_{Mo}$, $V_{Mo+3S}$, $V_{Mo+6S}$, $Mo_S$, $Mo_{2S-top}$, $S_{Mo}$, and $2S-top_{Mo}$. The first-principles simulations and NEGF technique were used to compute the LDOS, transmission curves, and IV characteristics of perfect and defective devices under bias in the range of $0.00\,V$ till $1.50\,V$. Our systematic study showed that defects at the interfaces improve the transport properties of such devices. More notably, we

have found that transport properties are enhanced in the presence of energetically favorable intrinsic point defects. In contrast to the scattering character of defects in 2H-phase $MoS_2$, at the interface, they led to emergence of resonant states close to the Fermi level, thereby giving rise to the enhancement of the current flow. In particular, creating a molybdenum vacancy induced defect midgap states in the LDOS and improved the transport characteristics, which, in turn, led to an increase in the current up to two orders of magnitude.

## 6.2 Outlook

Applying strain allows to tune the electronic, energetic, and optical properties of monolayers in a controllable way. Besides, due to the analogy of the properties and geometries of various compounds in the TMD family, we expect a similar response to strain from the intrinsic defects inside their monolayers. As the properties of the TMDs monolayers containing defects are very much affected by the applied deformations, a possible approach is to take a closer look at the change in their exitonic effects under different strain situations. The knowledge developed in this study could also pave the way for the promising applications of lateral heterojunctions of 1T-2H $MoS_2$ monlayers in field effect devices. The next step would be applying strain to such lateral heterojunctions-based devices. Hence, developing our method and analysis towards the better understanding of the response from defects within photodetectors under the mechanical deformations. Moreover, transport properties of these two dimensional defective devices could be investigated when gate voltage is applied or coulomb engineering techniques are used to manipulate the electronic states.

These findings should stimulate further experimental investigations on strain and defect engineering of TMDs monolayers and will be beneficial to their potential application in self-powered nanosystems, electromechanical sensors, photovoltaic, piezoelectric, and flexible devices. The exploitation of these phenomena may also allow to build blocks for new electronic and optoelectronic devices with minimal sizes and performances surpassing present technologies. Thus, it is our belief that

the knowledge we obtained from this thesis can provide new perspectives for the future applications of nanoelectronic devices based on TMDs monolayers.

# Bibliography

[1] B.M. Nichols, A.L. Mazzoni, M.L. Chin, P.B. Shah, S. Najmaei, R.A. Burke, and M. Dubey. Advances in 2D Materials for Electronic Devices. *Semiconductors and Semimetals*, 95:221–277, jan 2016. (cit. on pp. 1, 2, and 37)

[2] Chaoliang Tan, Xiehong Cao, Xue-Jun Wu, Qiyuan He, Jian Yang, Xiao Zhang, Junze Chen, Wei Zhao, Shikui Han, Gwang-Hyeon Nam, Melinda Sindoro, and Hua Zhang. Recent Advances in Ultrathin Two-Dimensional Nanomaterials. *Chemical Reviews*, 117(9):6225–6331, 2017. (cit. on pp. 1 and 2)

[3] Zhong Lin, Yu Lei, Shruti Subramanian, Natalie Briggs, Yuanxi Wang, Chun Li Lo, Eilam Yalon, David Lloyd, Sanfeng Wu, Kristie Koski, Richard Clark, Saptarshi Das, Robert M. Wallace, Thomas Kuech, Joseph Scott Bunch, Xiaoqin Li, Zhihong Chen, Eric Pop, Vincent H. Crespi, Joshua A. Robinson, and Mauricio Terrones. Research Update: Recent progress on 2D materials beyond graphene: From ripples, defects, intercalation, and valley dynamics to straintronics and power dissipation. *APL Materials*, 6(8):080701, aug 2018. (cit. on pp. 1, 2, 4, 5, 58, and 59)

[4] Seba Varghese, Saino Varghese, Sundaram Swaminathan, Krishna Singh, and Vikas Mittal. Two-Dimensional Materials for Sensing: Graphene and Beyond. *Electronics*, 4(3):651–687, sep 2015. (cit. on pp. 1 and 2)

[5] Dehui Deng, K. S. Novoselov, Qiang Fu, Nanfeng Zheng, Zhongqun Tian, and Xinhe Bao. Catalysis with two-dimensional materials and their heterostructures, mar 2016. (cit. on p. 1)

[6] Andreas Pospischil and Thomas Mueller. Optoelectronic Devices Based on Atomically Thin Transition Metal Dichalcogenides. *Applied Sciences*, 6(3):78, mar 2016. (cit. on pp. 1 and 4)

[7] Hengcong Tao, Qun Fan, Tao Ma, Shizhen Liu, Henry Gysling, John Texter, Fen Guo, and Zhenyu Sun. Two-dimensional materials for energy conversion and storage. *Progress in Materials Science*, page 100637, jan 2020. (cit. on pp. 1 and 2)

[8] Gianluca Fiori, Francesco Bonaccorso, Giuseppe Iannaccone, Tomás Palacios, Daniel Neumaier, Alan Seabaugh, Sanjay K. Banerjee, and Luigi Colombo. Electronics based on two-dimensional materials. *Nature Nanotechnology*, 9(10):768–779, oct 2014. (cit. on pp. 1, 2, and 37)

[9] Manish Chhowalla, Debdeep Jena, and Hua Zhang. Two-dimensional semiconductors for transistors, aug 2016. (cit. on pp. 1 and 2)

[10] Hanyu Zhu, Yuan Wang, Jun Xiao, Ming Liu, Shaomin Xiong, Zi Jing Wong, Ziliang Ye, Yu Ye, Xiaobo Yin, and Xiang Zhang. Observation of piezoelectricity in free-standing monolayer MoS2. *Nature Nanotechnology*, 10(2):151–155, 2015. (cit. on pp. 1, 7, 37, and 49)

[11] Patricia Gant, Peng Huang, David Pérez de Lara, Dan Guo, Riccardo Frisenda, and Andres Castellanos-Gomez. A strain tunable single-layer MoS 2 photodetector. *Materials Today*, may 2019. (cit. on pp. 1, 4, 7, 8, and 49)

[12] Hannu-Pekka Komsa and Arkady V Krasheninnikov. Effects of confinement and environment on the electronic structure and exciton binding energy of MoS2 from first principles. *Physical Review B*, 8622, 2012. (cit. on pp. 1, 6, and 41)

[13] C. Steinke, D. Mourad, M. Rösner, M. Lorke, C. Gies, F. Jahnke, G. Czycholl, and T. O. Wehling. Noninvasive control of excitons in two-dimensional materials. *Physical Review B*, 96(4):045431, jul 2017. (cit. on pp. 1 and 2)

[14] A K Geim. Graphene: Status and prospects, jun 2009. (cit. on p. 1)

[15] Chaoliang Tan, Zhengdong Liu, Wei Huang, and Hua Zhang. Non-volatile resistive memory devices based on solution-processed ultrathin two-dimensional nanomaterials, may 2015. (cit. on pp. 1, 2, and 6)

[16] Tae Young Kim, Jewook Ha, Kyungjune Cho, Jinsu Pak, Jiseok Seo, Jongjang Park, Jae Keun Kim, Seungjun Chung, Yongtaek Hong, and Takhee Lee. Transparent Large-Area MoS2 Phototransistors with Inkjet-Printed Components on Flexible Platforms. *ACS Nano*, 11(10):10273–10280, oct 2017. (cit. on pp. 2, 6, 7, 37, and 49)

[17] Zhong Lin, Bruno R Carvalho, Ethan Kahn, Ruitao Lv, Rahul Rao, Humberto Terrones, Marcos A Pimenta, and Mauricio Terrones. Defect engineering of two-dimensional transition metal dichalcogenides, apr 2016. (cit. on pp. 2, 6, 37, 44, 59, 61, 75, 81, and 82)

[18] Damien Voiry, Aditya Mohite, and Manish Chhowalla. Phase engineering of transition metal dichalcogenides, may 2015. (cit. on pp. 2 and 4)

[19] Saptarshi Das, Richard Gulotty, Anirudha V. Sumant, and Andreas Roelofs. All two-dimensional, flexible, transparent, and thinnest thin film transistor. *Nano Letters*, 14(5):2861–2866, 2014. (cit. on p. 2)

[20] Sajedeh Manzeli, Dmitry Ovchinnikov, Diego Pasquier, Oleg V. Yazyev, and Andras Kis. 2D transition metal dichalcogenides, jun 2017. (cit. on pp. 2 and 3)

[21] Kin Fai Mak, Changgu Lee, James Hone, Jie Shan, and Tony F. Heinz. Atomically Thin MoS2 : A New Direct-Gap Semiconductor. *Physical Review Letters*, 105(13):136805, sep 2010. (cit. on pp. 2, 4, 37, 40, and 58)

[22] Andrea Splendiani, Liang Sun, Yuanbo Zhang, Tianshu Li, Jonghwan Kim, Chi Yung Chim, Giulia Galli, and Feng Wang. Emerging photoluminescence

in monolayer MoS2. *Nano Letters*, 10(4):1271–1275, 2010. (cit. on pp. 2, 5, 37, and 40)

[23] B. Radisavljevic, A. Radenovic, J. Brivio, V. Giacometti, and A. Kis. Single-layer MoS2 transistors. *Nature Nanotechnology*, 6(3):147–150, mar 2011. (cit. on pp. 2, 6, 37, 43, and 75)

[24] Qing Hua Wang, Kourosh Kalantar-Zadeh, Andras Kis, Jonathan N. Coleman, and Michael S. Strano. Electronics and optoelectronics of two-dimensional transition metal dichalcogenides, nov 2012. (cit. on pp. 3, 5, 37, 58, and 59)

[25] Rafael Roldán, Jose A. Silva-Guillén, M. Pilar López-Sancho, Francisco Guinea, Emmanuele Cappelluti, and Pablo Ordejón. Electronic properties of single-layer and multilayer transition metal dichalcogenides MX2 (M = Mo, W and X = S, Se), oct 2014. (cit. on pp. 3, 4, 37, 40, 41, and 77)

[26] N. David Mermin Neil W. Ashcroft. Solid State Physics, 1976. (cit. on pp. 3 and 25)

[27] Charles Kittel. Introduction to Solid State Physics Solution Manual, 8th Edition. *Wiley*, 2004. (cit. on pp. 3, 12, and 17)

[28] Rafael Roldán, Luca Chirolli, Elsa Prada, Jose Angel Silva-Guillén, Pablo San-Jose, and Francisco Guinea. Theory of 2D crystals: Graphene and beyond, jul 2017. (cit. on pp. 4 and 37)

[29] Thomas Heine. Transition metal chalcogenides: Ultrathin inorganic materials with tunable electronic properties. *Accounts of Chemical Research*, 48(1):65–72, jan 2015. (cit. on p. 4)

[30] Minseok Choi. Strain-Enhanced p Doping in Monolayer MoS2. *Physical Review Applied*, 9(2):024009, feb 2018. (cit. on pp. 4 and 49)

[31] Karel Alexander N. Duerloo, Yao Li, and Evan J. Reed. Structural phase transitions in two-dimensional Mo-and W-dichalcogenide monolayers. *Nature Communications*, 5(1):1–9, jul 2014. (cit. on p. 4)

[32] Xiaoyan Guo, Guohui Yang, Junfeng Zhang, and Xiaohong Xu. Structural, mechanical and electronic properties of in-plane 1T/2H phase interface of MoS2 heterostructures. *AIP Advances*, 5(9), sep 2015. (cit. on p. 4)

[33] Ganesh Sivaraman, Fábio A.L. De Souza, Rodrigo G. Amorim, Wanderlã L. Scopel, Maria Fyta, and Ralph H. Scheicher. Electronic Transport along Hybrid MoS2 Monolayers. *Journal of Physical Chemistry C*, 120(41):23389–23396, oct 2016. (cit. on pp. 4, 5, 75, and 78)

[34] Rajesh Kappera, Damien Voiry, Sibel Ebru Yalcin, Brittany Branch, Gautam Gupta, Aditya D. Mohite, and Manish Chhowalla. Phase-engineered low-resistance contacts for ultrathin MoS2 transistors. *Nature Materials*, 13(12):1128–1134, dec 2014. (cit. on pp. 4, 5, and 74)

[35] Zhi Qiang Fan, Xiang Wei Jiang, Jun Wei Luo, Li Ying Jiao, Ru Huang, Shu Shen Li, and Lin Wang Wang. In-plane Schottky-barrier field-effect transistors based on 1 T /2 H heterojunctions of transition-metal dichalcogenides. *Physical Review B*, 96(16):165402, oct 2017. (cit. on pp. 4 and 75)

[36] Yung Chang Lin, Dumitru O. Dumcenco, Ying Sheng Huang, and Kazu Suenaga. Atomic mechanism of the semiconducting-to-metallic phase transition in single-layered MoS 2. *Nature Nanotechnology*, 9(5):391–396, apr 2014. (cit. on pp. 4 and 74)

[37] Goki Eda, Hisato Yamaguchi, Damien Voiry, Takeshi Fujita, Mingwei Chen, and Manish Chhowalla. Photoluminescence from chemically exfoliated MoS 2. *Nano Letters*, 11(12):5111–5116, dec 2011. (cit. on p. 4)

[38] Jaehyuck Jung, Hunyoung Bark, Doyoung Byun, Changgu Lee, and Dae Hyun Cho. Mechanical characterization of phase-changed single-layer MoS2 sheets. *2D Materials*, 6(2), feb 2019. (cit. on p. 4)

[39] Branimir Radisavljevic and Andras Kis. Mobility engineering and a metal-insulator transition in monolayer MoS 2. *Nature Materials*, 12(9):815–820, jun 2013. (cit. on p. 4)

[40] M. Kan, J. Y. Wang, X. W. Li, S. H. Zhang, Y. W. Li, Y. Kawazoe, Q. Sun, and P. Jena. Structures and phase transition of a MoS2 monolayer. *Journal of Physical Chemistry C*, 118(3):1515–1522, jan 2014. (cit. on p. 4)

[41] Goki Eda, Takeshi Fujita, Hisato Yamaguchi, Damien Voiry, Mingwei Chen, and Manish Chhowalla. Coherent atomic and electronic heterostructures of single-layer MoS 2. *ACS Nano*, 6(8):7311–7317, aug 2012. (cit. on pp. 4 and 75)

[42] Y. Katagiri, T. Nakamura, A. Ishii, C. Ohata, M. Hasegawa, S. Katsumoto, T. Cusati, A. Fortunelli, G. Iannaccone, G. Fiori, S. Roche, and J. Haruyama. Gate-tunable atomically thin lateral MoS2 Schottky junction patterned by electron beam. *Nano Letters*, 16(6):3788–3794, jun 2016. (cit. on p. 4)

[43] Amirhasan Nourbakhsh, Ahmad Zubair, Redwan N. Sajjad, Tavakkoli K.G. Amir, Wei Chen, Shiang Fang, Xi Ling, Jing Kong, Mildred S. Dresselhaus, Efthimios Kaxiras, Karl K. Berggren, Dimitri Antoniadis, and Tomás Palacios. MoS2 Field-Effect Transistor with Sub-10 nm Channel Length. *Nano Letters*, 16(12):7798–7806, dec 2016. (cit. on pp. 4 and 74)

[44] Ziyu Hu, Shengli Zhang, Yan Ning Zhang, Da Wang, Haibo Zeng, and Li Min Liu. Modulating the phase transition between metallic and semiconducting single-layer MoS2 and WS2 through size effects. *Physical Chemistry Chemical Physics*, 17(2):1099–1105, jan 2015. (cit. on pp. 4, 5, 75, and 78)

[45] Yierpan Aierken, Cem Sevik, Ouz Gülseren, François M. Peeters, and Deniz Çakir. In pursuit of barrierless transition metal dichalcogenides lateral heterojunctions. *Nanotechnology*, 29(29), may 2018. (cit. on pp. 4, 5, 75, and 78)

[46] Andrew J. Mannix, Brian Kiraly, Mark C. Hersam, and Nathan P. Guisinger. Synthesis and chemistry of elemental 2D materials, jan 2017. (cit. on p. 5)

[47] J. Klein, M. Lorke, M. Florian, F. Sigger, L. Sigl, S. Rey, J. Wierzbowski, J. Cerne, K. Müller, E. Mitterreiter, P. Zimmermann, T. Taniguchi, K. Watanabe, U. Wurstbauer, M. Kaniber, M. Knap, R. Schmidt, J. J. Finley, and A. W.

Holleitner. Site-selectively generated photon emitters in monolayer MoS2 via local helium ion irradiation. *Nature Communications*, 10(1):2755, dec 2019. (cit. on pp. 5, 6, 43, 44, 46, 59, 61, 62, 63, 69, 75, and 80)

[48] Ali Zavabeti, Azmira Jannat, Li Zhong, Azhar Ali Haidry, Zhengjun Yao, and Jian Zhen Ou. Two-Dimensional Materials in Large-Areas: Synthesis, Properties and Applications, feb 2020. (cit. on pp. 5 and 6)

[49] Claudia Backes, Amr M Abdelkader, Concepción Alonso, Amandine Andrieux-Ledier, Raul Arenal, Jon Azpeitia, Nilanthy Balakrishnan, Luca Banszerus, Julien Barjon, Ruben Bartali, Sebastiano Bellani, Claire Berger, Reinhard Berger, M. M.Bernal Ortega, Carlo Bernard, Peter H Beton, André Beyer, Alberto Bianco, Peter Bøggild, Francesco Bonaccorso, Gabriela Borin Barin, Cristina Botas, Rebeca A Bueno, Daniel Carriazo, Andres Castellanos-Gomez, Meganne Christian, Artur Ciesielski, Tymoteusz Ciuk, Matthew T Cole, Jonathan Coleman, Camilla Coletti, Luigi Crema, Huanyao Cun, Daniela Dasler, Domenico De Fazio, Noel Díez, Simon Drieschner, Georg S Duesberg, Roman Fasel, Xinliang Feng, Alberto Fina, Stiven Forti, Costas Galiotis, Giovanni Garberoglio, Jorge M García, Jose Antonio Garrido, Marco Gibertini, Armin Gölzhäuser, Julio Gómez, Thomas Greber, Frank Hauke, Adrian Hemmi, Irene Hernandez-Rodriguez, Andreas Hirsch, Stephen A Hodge, Yves Huttel, Peter U Jepsen, Ignacio Jimenez, Ute Kaiser, Tommi Kaplas, Ho Kwon Kim, Andras Kis, Konstantinos Papagelis, Kostas Kostarelos, Aleksandra Krajewska, Kangho Lee, Changfeng Li, Harri Lipsanen, Andrea Liscio, Martin R Lohe, Annick Loiseau, Lucia Lombardi, Maria Francisca López, Oliver Martin, Cristina Martín, Lidia Martínez, Jose Angel Martin-Gago, José Ignacio Martínez, Nicola Marzari, Álvaro Mayoral, John McManus, Manuela Melucci, Javier Méndez, Cesar Merino, Pablo Merino, Andreas P Meyer, Elisa Miniussi, Vaidotas Miseikis, Neeraj Mishra, Vittorio Morandi, Carmen Munuera, Roberto Muñoz, Hugo Nolan, Luca Ortolani, Anna K Ott, Irene Palacio, Vincenzo Palermo, John Parthenios, Iwona Pasternak, Amalia Patane, Maurizio Prato, Henri Prevost, Vladimir Prudkovskiy, Nicola Pugno,

Teófilo Rojo, Antonio Rossi, Pascal Ruffieux, Paolo Samorì, Léonard Schué, Eki Setijadi, Thomas Seyller, Giorgio Speranza, Christoph Stampfer, Ingrid Stenger, Wlodek Strupinski, Yuri Svirko, Simone Taioli, Kenneth B.K. Teo, Matteo Testi, Flavia Tomarchio, Mauro Tortello, Emanuele Treossi, Andrey Turchanin, Ester Vazquez, Elvira Villaro, Patrick R Whelan, Zhenyuan Xia, Rositza Yakimova, Sheng Yang, G Reza Yazdi, Chanyoung Yim, Duhee Yoon, Xianghui Zhang, Xiaodong Zhuang, Luigi Colombo, Andrea C Ferrari, and Mar Garcia-Hernandez. Production and processing of graphene and related materials. *2D Materials*, 7(2):022001, jan 2020. (cit. on pp. 5 and 6)

[50] Simone Bertolazzi, Jacopo Brivio, and Andras Kis. Stretching and Breaking of Ultrathin MoS2. *ACS Nano*, 5(12):9703–9709, dec 2011. (cit. on pp. 5, 7, 8, 33, 42, 45, 49, 58, and 61)

[51] A. K. Geim and I. V. Grigorieva. Van der Waals heterostructures, jul 2013. (cit. on p. 5)

[52] Ronan J. Smith, Paul J. King, Mustafa Lotya, Christian Wirtz, Umar Khan, Sukanta De, Arlene O'Neill, Georg S. Duesberg, Jaime C. Grunlan, Gregory Moriarty, Jun Chen, Jiazhao Wang, Andrew I. Minett, Valeria Nicolosi, and Jonathan N. Coleman. Large-scale exfoliation of inorganic layered compounds in aqueous surfactant solutions. *Advanced Materials*, 23(34):3944–3948, sep 2011. (cit. on p. 6)

[53] Yongjie Zhan, Zheng Liu, Sina Najmaei, Pulickel M. Ajayan, and Jun Lou. Large-area vapor-phase growth and characterization of MoS 2 atomic layers on a SiO 2 substrate. *Small*, 8(7):966–971, apr 2012. (cit. on p. 6)

[54] Yumeng Shi, Wu Zhou, Ang Yu Lu, Wenjing Fang, Yi Hsien Lee, Allen Long Hsu, Soo Min Kim, Ki Kang Kim, Hui Ying Yang, Lain Jong Li, Juan Carlos Idrobo, and Jing Kong. Van der Waals epitaxy of MoS 2 layers using graphene as growth templates. *Nano Letters*, 12(6):2784–2791, jun 2012. (cit. on p. 6)

[55] Yi Hsien Lee, Xin Quan Zhang, Wenjing Zhang, Mu Tung Chang, Cheng Te Lin, Kai Di Chang, Ya Chu Yu, Jacob Tse Wei Wang, Chia Seng Chang, Lain Jong Li, and Tsung Wu Lin. Synthesis of large-area MoS 2 atomic layers with chemical vapor deposition. *Advanced Materials*, 24(17):2320–2325, may 2012. (cit. on pp. 6, 43, and 75)

[56] Jing Yu, Xiaozong Hu, Huiqiao Li, Xing Zhou, and Tianyou Zhai. Large-scale synthesis of 2D metal dichalcogenides, may 2018. (cit. on p. 6)

[57] Changyong Lan, Ziyao Zhou, Zhifei Zhou, Chun Li, Lei Shu, Lifan Shen, Dapan Li, Ruoting Dong, Sen Po Yip, and Johnny C. Ho. Wafer-scale synthesis of monolayer WS2 for high-performance flexible photodetectors by enhanced chemical vapor deposition. *Nano Research*, 11(6):3371–3384, jun 2018. (cit. on p. 6)

[58] Paul Masih Das, Jothi Priyanka Thiruraman, Yung Chien Chou, Gopinath Danda, and Marija Drndić. Centimeter-Scale Nanoporous 2D Membranes and Ion Transport: Porous MoS 2 Monolayers in a Few-Layer Matrix. *Nano Letters*, 19(1):392–399, jan 2019. (cit. on p. 6)

[59] S. Mathew, K. Gopinadhan, T. K. Chan, X. J. Yu, D. Zhan, L. Cao, A. Rusydi, M. B.H. Breese, S. Dhar, Z. X. Shen, T. Venkatesan, and John T.L. Thong. Magnetism in MoS 2 induced by proton irradiation. *Applied Physics Letters*, 101(10):102103, sep 2012. (cit. on p. 6)

[60] Sefaattin Tongay, Joonki Suh, Can Ataca, Wen Fan, Alexander Luce, Jeong Seuk Kang, Jonathan Liu, Changhyun Ko, Rajamani Raghunathanan, Jian Zhou, Frank Ogletree, Jingbo Li, Jeffrey C. Grossman, and Junqiao Wu. Defects activated photoluminescence in two-dimensional semiconductors: interplay between bound, charged and free excitons. *Scientific Reports*, 3(1):2657, dec 2013. (cit. on pp. 6, 47, 52, and 75)

[61] Wu Zhou, Xiaolong Zou, Sina Najmaei, Zheng Liu, Yumeng Shi, Jing Kong, Jun Lou, Pulickel M Ajayan, Boris I Yakobson, and Juan Carlos Idrobo. In-

trinsic structural defects in monolayer molybdenum disulfide. *Nano Letters*, 13(6):2615–2622, 2013. (cit. on pp. 6, 44, 45, 58, 61, 63, 75, and 80)

[62] Arend M. Van Der Zande, Pinshane Y. Huang, Daniel A. Chenet, Timothy C. Berkelbach, Yumeng You, Gwan Hyoung Lee, Tony F. Heinz, David R. Reichman, David A. Muller, and James C. Hone. Grains and grain boundaries in highly crystalline monolayer molybdenum disulphide. *Nature Materials*, 12(6):554–561, jun 2013. (cit. on pp. 6 and 58)

[63] Zhuangzhi Wu, Baizeng Fang, Zhiping Wang, Changlong Wang, Zhihong Liu, Fangyang Liu, Wei Wang, Akram Alfantazi, Dezhi Wang, and David P. Wilkinson. MoS2 nanosheets: A designed structure with high active site density for the hydrogen evolution reaction. *ACS Catalysis*, 3(9):2101–2107, sep 2013. (cit. on p. 6)

[64] Joonki Suh, Tae Eon Park, Der Yuh Lin, Deyi Fu, Joonsuk Park, Hee Joon Jung, Yabin Chen, Changhyun Ko, Chaun Jang, Yinghui Sun, Robert Sinclair, Joonyeon Chang, Sefaattin Tongay, and Junqiao Wu. Doping against the native propensity of MoS2: Degenerate hole doping by cation substitution. *Nano Letters*, 14(12):6976–6982, dec 2014. (cit. on p. 6)

[65] Stephen McDonnell, Rafik Addou, Creighton Buie, Robert M. Wallace, and Christopher L. Hinkle. Defect-Dominated Doping and Contact Resistance in MoS2. *ACS Nano*, 8(3):2880–2888, mar 2014. (cit. on pp. 6, 7, and 43)

[66] Marcos A. Pimenta, Elena Del Corro, Bruno R. Carvalho, Cristiano Fantini, and Leandro M. Malard. Comparative study of raman spectroscopy in graphene and MoS2-type transition metal dichalcogenides. *Accounts of Chemical Research*, 48(1):41–47, jan 2015. (cit. on p. 6)

[67] Amber McCreary, Ayse Berkdemir, Junjie Wang, Minh An Nguyen, Ana Laura Elías, Néstor Perea-López, Kazunori Fujisawa, Bernd Kabius, Victor Carozo, David A. Cullen, Thomas E. Mallouk, J. Zhu, and Mauricio Terrones. Distinct photoluminescence and Raman spectroscopy signatures for

identifying highly crystalline WS2 monolayers produced by different growth methods. *Journal of Materials Research*, 31(7):931–944, apr 2016. (cit. on p. 6)

[68] Guru P. Neupane, Minh Dao Tran, Seok Joon Yun, Hyun Kim, Changwon Seo, Jubok Lee, Gang Hee Han, A. K. Sood, and Jeongyong Kim. Simple Chemical Treatment to n-Dope Transition-Metal Dichalcogenides and Enhance the Optical and Electrical Characteristics. *ACS Applied Materials and Interfaces*, 9(13):11950–11958, apr 2017. (cit. on p. 6)

[69] Quan Ma, Miguel Isarraraz, Chen S. Wang, Edwin Preciado, Velveth Klee, Sarah Bobek, Koichi Yamaguchi, Emily Li, Patrick Michael Odenthal, Ariana Nguyen, David Barroso, Dezheng Sun, Gretel Von Son Palacio, Michael Gomez, Andrew Nguyen, Duy Le, Greg Pawin, John Mann, Tony F. Heinz, Talat Shahnaz Rahman, and Ludwig Bartels. Postgrowth tuning of the bandgap of single-layer molybdenum disulfide films by sulfur/selenium exchange. *ACS Nano*, 8(5):4672–4677, may 2014. (cit. on p. 6)

[70] Mikai Chen, Hongsuk Nam, Sungjin Wi, Lian Ji, Xin Ren, Lifeng Bian, Shulong Lu, and Xiaogan Liang. Stable few-layer MoS2 rectifying diodes formed by plasma-assisted doping. *Applied Physics Letters*, 103(14):142110, sep 2013. (cit. on p. 6)

[71] Haiyan Nan, Renwu Zhou, Xiaofeng Gu, Shaoqing Xiao, and Kostya Ken Ostrikov. Recent advances in plasma modification of 2D transition metal dichalcogenides, nov 2019. (cit. on p. 6)

[72] Hao Qiu, Lijia Pan, Zongni Yao, Junjie Li, Yi Shi, and Xinran Wang. Electrical characterization of back-gated bi-layer MoS 2 field-effect transistors and the effect of ambient on their performances. *Applied Physics Letters*, 100(12):123104, mar 2012. (cit. on p. 6)

[73] Hao Qiu, Tao Xu, Zilu Wang, Wei Ren, Haiyan Nan, Zhenhua Ni, Qian Chen, Shijun Yuan, Feng Miao, Fengqi Song, Gen Long, Yi Shi, Litao Sun, Jinlan

Wang, and Xinran Wang. Hopping transport through defect-induced localized states in molybdenum disulphide. *Nature Communications*, 4, 2013. (cit. on p. 6)

[74] Hui Zhu, Qingxiao Wang, Lanxia Cheng, Rafik Addou, Jiyoung Kim, Moon J. Kim, and Robert M. Wallace. Defects and Surface Structural Stability of MoTe2 under Vacuum Annealing. *ACS Nano*, 11(11):11005–11014, nov 2017. (cit. on p. 6)

[75] Mahdi Ghorbani-Asl, Silvan Kretschmer, Douglas E Spearot, and Arkady V Krasheninnikov. Two-dimensional MoS2 under ion irradiation: from controlled defect production to electronic structure engineering. *2D Materials*, 4(2):025078, apr 2017. (cit. on pp. 6, 44, 61, 63, 69, and 75)

[76] Zuyun He, Ran Zhao, Xiaofei Chen, Huijun Chen, Yunmin Zhu, Huimin Su, Shengxi Huang, Jianming Xue, Junfeng Dai, Shuang Cheng, Meilin Liu, Xinwei Wang, and Yan Chen. Defect Engineering in Single-Layer MoS 2 Using Heavy Ion Irradiation. *ACS Applied Materials and Interfaces*, 10(49):42524–42533, dec 2018. (cit. on p. 6)

[77] J Klein, A Kuc, A Nolinder, M Altzschner, J Wierzbowski, F Sigger, F Kreupl, J J Finley, U Wurstbauer, A W Holleitner, and M Kaniber. Robust valley polarization of helium ion modified atomically thin MoS2. *2D Materials*, 5(1):011007, nov 2018. (cit. on pp. 6, 48, and 62)

[78] Chih Pin Lu, Guohong Li, Jinhai Mao, Li Min Wang, and Eva Y. Andrei. Bandgap, mid-gap states, and gating effects in MoS2. *Nano Letters*, 14(8):4628–4633, aug 2014. (cit. on p. 6)

[79] Sang Wook Han, Youngsin Park, Young Hun Hwang, Soyoung Jekal, Manil Kang, Wang G. Lee, Woochul Yang, Gun Do Lee, and Soon Cheol Hong. Electron beam-formed ferromagnetic defects on MoS2 surface along 1 T phase transition. *Scientific Reports*, 6(1):1–8, dec 2016. (cit. on pp. 6, 75, and 80)

[80] Silvan Kretschmer, Tibor Lehnert, Ute Kaiser, and Arkady V. Krasheninnikov. Formation of Defects in Two-Dimensional MoS2 in the Transmission Electron Microscope at Electron Energies below the Knock-on Threshold: The Role of Electronic Excitations. *Nano Letters*, 20(4):2865–2870, apr 2020. (cit. on p. 6)

[81] K S Novoselov, D Jiang, F Schedin, T J Booth, V V Khotkevich, S V Morozov, and A K Geim. Two-dimensional atomic crystals. *Proceedings of the National Academy of Sciences*, 102(30):10451–10453, jul 2005. (cit. on pp. 6, 43, and 75)

[82] L. Ma, Y. Tan, M. Ghorbani-Asl, R. Boettger, S. Kretschmer, S. Zhou, Z. Huang, A. V. Krasheninnikov, and F. Chen. Tailoring the optical properties of atomically-thin WS 2 : Via ion irradiation. *Nanoscale*, 9(31):11027–11034, aug 2017. (cit. on pp. 6, 44, 61, 63, 75, and 80)

[83] Kin Fai Mak and Jie Shan. Photonics and optoelectronics of 2D semiconductor transition metal dichalcogenides, 2016. (cit. on pp. 6, 43, 58, and 59)

[84] R S Sundaram, M Engel, A Lombardo, R Krupke, A C Ferrari, Ph Avouris, and M Steiner. Electroluminescence in single layer MoS2. *Nano Letters*, 13(4):1416–1421, 2013. (cit. on pp. 6 and 43)

[85] Yu Ming He, Genevieve Clark, John R Schaibley, Yu He, Ming Cheng Chen, Yu Jia Wei, Xing Ding, Qiang Zhang, Wang Yao, Xiaodong Xu, Chao Yang Lu, and Jian Wei Pan. Single quantum emitters in monolayer semiconductors. *Nature Nanotechnology*, 10(6):497–502, 2015. (cit. on pp. 6, 43, and 59)

[86] Shanshan Wang, Gun-Do Lee, Sungwoo Lee, Euijoon Yoon, and Jamie H. Warner. Detailed Atomic Reconstruction of Extended Line Defects in Monolayer MoS2. *ACS Nano*, 10(5):5419–5430, may 2016. (cit. on pp. 6 and 43)

[87] Marco M. Furchi, Dmitry K. Polyushkin, Andreas Pospischil, and Thomas Mueller. Mechanisms of photoconductivity in atomically thin MoS2. *Nano Letters*, 14(11):6165–6170, nov 2014. (cit. on pp. 7 and 43)

[88] Iddo Amit, Tobias J. Octon, Nicola J. Townsend, Francesco Reale, C. David Wright, Cecilia Mattevi, Monica F. Craciun, and Saverio Russo. Role of Charge Traps in the Performance of Atomically Thin Transistors. *Advanced Materials*, 29(19):1605598, may 2017. (cit. on pp. 7, 43, and 59)

[89] Mohan Kumar Ghimire, Hyunjin Ji, Hamza Zad Gul, Hojoon Yi, Jinbao Jiang, and Seong Chu Lim. Defect-Affected Photocurrent in MoTe 2 FETs. *ACS Applied Materials and Interfaces*, 11(10):10068–10073, mar 2019. (cit. on pp. 7, 43, and 59)

[90] Jie Su, Ning Li, Yingying Zhang, Liping Feng, and Zhengtang Liu. Role of vacancies in tuning the electronic properties of Au-MoS 2 contact. *AIP Advances*, 5(7):077182, jul 2015. (cit. on pp. 7 and 43)

[91] Li Ping Feng, Jie Su, and Zheng Tang Liu. Effect of vacancies in monolayer MoS2 on electronic properties of Mo-MoS 2 contacts. *RSC Advances*, 5(26):20538–20544, feb 2015. (cit. on pp. 7, 43, and 75)

[92] Li Ping Feng, Jie Su, Da Peng Li, and Zheng Tang Liu. Tuning the electronic properties of Ti-MoS 2 contacts through introducing vacancies in monolayer MoS 2. *Physical Chemistry Chemical Physics*, 17(10):6700–6704, feb 2015. (cit. on pp. 7 and 43)

[93] Jie Su, Liping Feng, Yan Zhang, and Zhengtang Liu. Defect induced gap states in monolayer MoS2 control the Schottky barriers of Pt-mMoS2 interfaces. *Applied Physics Letters*, 110(16):161604, apr 2017. (cit. on pp. 7 and 43)

[94] Hong Li, Charlie Tsai, Ai Leen Koh, Lili Cai, Alex W. Contryman, Alex H. Fragapane, Jiheng Zhao, Hyun Soon Han, Hari C. Manoharan, Frank Abild-Pedersen, Jens K. Nørskov, and Xiaolin Zheng. Activating and optimizing MoS2 basal planes for hydrogen evolution through the formation of strained sulphur vacancies. *Nature Materials*, 15(1):48–53, jan 2016. (cit. on p. 7)

[95] Ying Yin, Jiecai Han, Yumin Zhang, Xinghong Zhang, Ping Xu, Quan Yuan, Leith Samad, Xianjie Wang, Yi Wang, Zhihua Zhang, Peng Zhang, Xingzhong

Cao, Bo Song, and Song Jin. Contributions of Phase, Sulfur Vacancies, and Edges to the Hydrogen Evolution Reaction Catalytic Activity of Porous Molybdenum Disulfide Nanosheets. *Journal of the American Chemical Society*, 138(25):7965–7972, jun 2016. (cit. on p. 7)

[96] Andres Castellanos-Gomez, Menno Poot, Gary A. Steele, Herre S J Van Der Zant, Nicols Agrat, and Gabino Rubio-Bollinger. Elastic properties of freely suspended MoS2 nanosheets. *Advanced Materials*, 24(6):772–775, feb 2012. (cit. on pp. 7, 8, 33, and 58)

[97] Andres Castellanos-Gomez, Vibhor Singh, Herre S.J. Van Der Zant, and Gary A. Steele. Mechanics of freely-suspended ultrathin layered materials, jan 2015. (cit. on pp. 7 and 58)

[98] J. Munguía, G. Bremond, J. M. Bluet, J. M. Hartmann, and M. Mermoux. Strain dependence of indirect band gap for strained silicon on insulator wafers. *Applied Physics Letters*, 93(10):102101, sep 2008. (cit. on p. 7)

[99] Rafael Roldán, Andrés Castellanos-Gomez, Emmanuele Cappelluti, and Francisco Guinea. Strain engineering in semiconducting two-dimensional crystals, aug 2015. (cit. on pp. 7, 8, 33, 42, 45, 58, and 59)

[100] M. Ghorbani-Asl, S. Borini, A. Kuc, and T. Heine. Strain-dependent modulation of conductivity in single-layer transition-metal dichalcogenides. *Physical Review B*, 87(23):235434, jun 2013. (cit. on pp. 7, 42, 45, and 58)

[101] David Lloyd, Xinghui Liu, Jason W Christopher, Lauren Cantley, Anubhav Wadehra, Brian L Kim, Bennett B Goldberg, Anna K Swan, and J Scott Bunch. Band Gap Engineering with Ultralarge Biaxial Strains in Suspended Monolayer MoS2. *Nano Letters*, 16(9):5836–5841, 2016. (cit. on pp. 7 and 58)

[102] Jason W. Christopher, Mounika Vutukuru, David Lloyd, J. Scott Bunch, Bennett B. Goldberg, David J. Bishop, and Anna K. Swan. Monolayer $MoS_2$ Strained to 1.3% with a Microelectromechanical System. *Journal of Microelectromechanical Systems*, pages 1–10, 2019. (cit. on p. 7)

[103] Li Gao. Flexible Device Applications of 2D Semiconductors. *Small*, 13(35):1603994, sep 2017. (cit. on pp. 7, 37, and 49)

[104] Ji Feng, Xiaofeng Qian, Cheng Wei Huang, and Ju Li. Strain-engineered artificial atom as a broad-spectrum solar energy funnel. *Nature Photonics*, 6(12):866–872, 2012. (cit. on pp. 7 and 49)

[105] G. Plechinger, F.-X. Schrettenbrunner, J. Eroms, D. Weiss, C. Schüller, and T. Korn. Low-temperature photoluminescence of oxide-covered single-layer MoS2. *physica status solidi (RRL) - Rapid Research Letters*, 6(3):126–128, mar 2012. (cit. on pp. 8 and 33)

[106] Gerd Plechinger, Andres Castellanos-Gomez, Michele Buscema, Herre S.J. Van Der Zant, Gary A Steele, Agnieszka Kuc, Thomas Heine, Christian Schüller, and Tobias Korn. Control of biaxial strain in single-layer molybdenite using local thermal expansion of the substrate. *2D Materials*, 2(1):015006, mar 2015. (cit. on pp. 8 and 33)

[107] Yeung Yu Hui, Xiaofei Liu, Wenjing Jie, Ngai Yui Chan, Jianhua Hao, Yu Te Hsu, Lain Jong Li, Wanlin Guo, and Shu Ping Lau. Exceptional tunability of band energy in a compressively strained trilayer MoS2 sheet. *ACS Nano*, 7(8):7126–7131, aug 2013. (cit. on pp. 8 and 33)

[108] Mingyuan Huang, Hugen Yan, Tony F. Heinz, and James Hone. Probing strain-induced electronic structure change in graphene by Raman spectroscopy. *Nano Letters*, 10(10):4074–4079, oct 2010. (cit. on pp. 8 and 33)

[109] Hiram J. Conley, Bin Wang, Jed I. Ziegler, Richard F. Haglund, Sokrates T. Pantelides, and Kirill I. Bolotin. Bandgap engineering of strained monolayer and bilayer MoS2. *Nano Letters*, 13(8):3626–3630, aug 2013. (cit. on pp. 8 and 33)

[110] Yanlong Wang, Chunxiao Cong, Weihuang Yang, Jingzhi Shang, Namphung Peimyoo, Yu Chen, Junyong Kang, Jianpu Wang, Wei Huang, and Ting Yu.

Strain-induced directindirect bandgap transition and phonon modulation in monolayer WS2. *Nano Research*, 8(8):2562–2572, aug 2015. (cit. on pp. 8 and 33)

[111] Shengxue Yang, Cong Wang, Hasan Sahin, Hui Chen, Yan Li, Shu Shen Li, Aslihan Suslu, Francois M. Peeters, Qian Liu, Jingbo Li, and Sefaattin Tongay. Tuning the optical, magnetic, and electrical properties of ReSe2 by nanoscale strain engineering. *Nano Letters*, 15(3):1660–1666, mar 2015. (cit. on pp. 8 and 33)

[112] Andres Castellanos-Gomez, Rafael Roldán, Emmanuele Cappelluti, Michele Buscema, Francisco Guinea, Herre S.J. Van Der Zant, and Gary A. Steele. Local strain engineering in atomically thin MoS2. *Nano Letters*, 13(11):5361–5366, nov 2013. (cit. on pp. 8 and 33)

[113] A. A. Griffits. VI. The phenomena of rupture and flow in solids. *Philosophical Transactions of the Royal Society of London. Series A, Containing Papers of a Mathematical or Physical Character*, 221(582-593):163–198, jan 1921. (cit. on p. 8)

[114] Ryan C. Cooper, Changgu Lee, Chris A. Marianetti, Xiaoding Wei, James Hone, and Jeffrey W. Kysar. Nonlinear elastic behavior of two-dimensional molybdenum disulfide. *Physical Review B - Condensed Matter and Materials Physics*, 87(3):035423, jan 2013. (cit. on p. 8)

[115] Richard M. Martin. Electronic Structure Basic Theory and Practical Methods. apr 2004. (cit. on pp. 12 and 17)

[116] Robert G. Parr and Weitao. Yang. *Density-functional theory of atoms and molecules*. Oxford University Press, 1989. (cit. on pp. 12 and 17)

[117] M. Born and R. Oppenheimer. Zur Quantentheorie der Molekeln. *Annalen der Physik*, 389(20):457–484, jan 1927. (cit. on pp. 12 and 14)

[118] D. R. Hartree. The Wave Mechanics of an Atom with a Non-Coulomb Central Field Part I Theory and Methods. *Mathematical Proceedings of the Cambridge Philosophical Society*, 24(1):89–110, 1928. (cit. on p. 14)

[119] V. Fock. Näherungsmethode zur Lösung des quantenmechanischen Mehrkörperproblems. *Zeitschrift für Physik*, 61(1-2):126–148, jan 1930. (cit. on p. 14)

[120] P. Hohenberg and W. Kohn. Inhomogeneous electron gas. *Physical Review*, 136(3B):B864, nov 1964. (cit. on p. 15)

[121] W. Kohn and L. J. Sham. Self-consistent equations including exchange and correlation effects. *Physical Review*, 140(4A):A1133, nov 1965. (cit. on pp. 16 and 17)

[122] Ralf Stowasser and Roald Hoffmann. What do the Kohn-Sham orbitals and eigenvalues mean?, apr 1999. (cit. on p. 16)

[123] Jorge Kohanoff. frontmatter. In *Book*, number May, page 348. Cambridge University Press, 2006. (cit. on p. 17)

[124] Roberto Peverati and Donald G. Truhlar. Quest for a universal density functional: The accuracy of density functionals across a broad spectrum of databases in chemistry and physics, mar 2014. (cit. on p. 17)

[125] J. P. Perdew and Alex Zunger. Self-interaction correction to density-functional approximations for many-electron systems. *Physical Review B*, 23(10):5048–5079, may 1981. (cit. on pp. 17 and 18)

[126] John P. Perdew, Kieron Burke, and Matthias Ernzerhof. Generalized gradient approximation made simple. *Physical Review Letters*, 77(18):3865–3868, oct 1996. (cit. on pp. 17, 18, 38, 60, and 76)

[127] P. A.M. Dirac. Note on Exchange Phenomena in the Thomas Atom. *Mathematical Proceedings of the Cambridge Philosophical Society*, 26(3):376–385, 1930. (cit. on p. 18)

[128] D. M. Ceperley and B. J. Alder. Ground state of the electron gas by a stochastic method. *Physical Review Letters*, 45(7):566–569, aug 1980. (cit. on p. 18)

[129] John P. Perdew and Yue Wang. Accurate and simple analytic representation of the electron-gas correlation energy. *Physical Review B*, 45(23):13244–13249, jun 1992. (cit. on p. 18)

[130] Axel D. Becke. Perspective: Fifty years of density-functional theory in chemical physics. *Journal of Chemical Physics*, 140(18):18A301, may 2014. (cit. on p. 18)

[131] John P. Perdew and Wang Yue. Accurate and simple density functional for the electronic exchange energy: Generalized gradient approximation. *Physical Review B*, 33(12):8800–8802, jun 1986. (cit. on p. 18)

[132] A. D. Becke. Density-functional exchange-energy approximation with correct asymptotic behavior. *Physical Review A*, 38(6):3098–3100, sep 1988. (cit. on p. 18)

[133] Chengteh Lee, Weitao Yang, and Robert G. Parr. Development of the Colle-Salvetti correlation-energy formula into a functional of the electron density. *Physical Review B*, 37(2):785–789, jan 1988. (cit. on p. 18)

[134] José M Soler, Emilio Artacho, Julian D Gale, Alberto García, Javier Junquera, Pablo Ordejón, and Daniel Sánchez-Portal. The SIESTA method for ab initio order-N materials simulation. *Journal of Physics Condensed Matter*, 14(11):2745–2779, mar 2002. (cit. on pp. 19, 38, 59, and 76)

[135] SIESTA. Siesta in Launchpad. (cit. on p. 19)

[136] G. Kresse and J. Furthmüller. Efficient iterative schemes for ab initio total-energy calculations using a plane-wave basis set. *Physical Review B - Condensed Matter and Materials Physics*, 54(16):11169–11186, oct 1996. (cit. on p. 19)

[137] Stewart J. Clark, Matthew D. Segall, Chris J. Pickard, Phil J. Hasnip, Matt I.J. Probert, Keith Refson, and Mike C. Payne. First principles methods using CASTEP. *Zeitschrift fur Kristallographie*, 220(5-6):567–570, 2005. (cit. on p. 19)

[138] J. J. Mortensen, L. B. Hansen, and K. W. Jacobsen. Real-space grid implementation of the projector augmented wave method. *Physical Review B - Condensed Matter and Materials Physics*, 71(3):035109, jan 2005. (cit. on p. 19)

[139] Paolo Giannozzi, Stefano Baroni, Nicola Bonini, Matteo Calandra, Roberto Car, Carlo Cavazzoni, Davide Ceresoli, Guido L. Chiarotti, Matteo Cococcioni, Ismaila Dabo, Andrea Dal Corso, Stefano De Gironcoli, Stefano Fabris, Guido Fratesi, Ralph Gebauer, Uwe Gerstmann, Christos Gougoussis, Anton Kokalj, Michele Lazzeri, Layla Martin-Samos, Nicola Marzari, Francesco Mauri, Riccardo Mazzarello, Stefano Paolini, Alfredo Pasquarello, Lorenzo Paulatto, Carlo Sbraccia, Sandro Scandolo, Gabriele Sclauzero, Ari P. Seitsonen, Alexander Smogunov, Paolo Umari, and Renata M. Wentzcovitch. QUANTUM ESPRESSO: A modular and open-source software project for quantum simulations of materials. *Journal of Physics Condensed Matter*, 21(39):395502, sep 2009. (cit. on p. 19)

[140] X. Gonze, J. M. Beuken, R. Caracas, F. Detraux, M. Fuchs, G. M. Rignanese, L. Sindic, M. Verstraete, G. Zerah, F. Jollet, M. Torrent, A. Roy, M. Mikami, Ph Ghosez, J. Y. Raty, and D. C. Allan. First-principles computation of material properties: The ABINIT software project. *Computational Materials Science*, 25(3):478–492, nov 2002. (cit. on p. 19)

[141] R. S. Mulliken. Electronic population analysis on LCAO-MO molecular wave functions. II. Overlap populations, bond orders, and covalent bond energies. *The Journal of Chemical Physics*, 23(10):1841–1846, 1955. (cit. on p. 21)

[142] Célia Fonseca Guerra, Jan Willem Handgraaf, Evert Jan Baerends, and F. Matthias Bickelhaupt. Voronoi Deformation Density (VDD) Charges: As-

sessment of the Mulliken, Bader, Hirshfeld, Weinhold, and VDD Methods for Charge Analysis. *Journal of Computational Chemistry*, 25(2):189–210, jan 2004. (cit. on p. 22)

[143] M. Soriano and J. J. Palacios. Theory of projections with nonorthogonal basis sets: Partitioning techniques and effective Hamiltonians. *Physical Review B - Condensed Matter and Materials Physics*, 90(7):075128, aug 2014. (cit. on p. 22)

[144] Rolf Landauer. Electrical resistance of disordered one-dimensional lattices. *Philosophical Magazine*, 21(172):863–867, 1970. (cit. on pp. 23, 32, and 77)

[145] M. Bttiker, Y. Imry, R. Landauer, and S. Pinhas. Generalized many-channel conductance formula with application to small rings. *Physical Review B*, 31(10):6207–6215, may 1985. (cit. on pp. 23 and 32)

[146] Paul C. Martin and Julian Schwinger. Theory of many-particle systems. I. *Physical Review*, 115(6):1342–1373, sep 1959. (cit. on p. 26)

[147] Roger Lake and Supriyo Datta. Nonequilibrium Greens-function method applied to double-barrier resonant-tunneling diodes. *Physical Review B*, 45(12):6670–6685, mar 1992. (cit. on p. 26)

[148] Yigal Meir and Ned S. Wingreen. Landauer formula for the current through an interacting electron region. *Physical Review Letters*, 68(16):2512–2515, apr 1992. (cit. on p. 26)

[149] Michael Wimmer. *Quantum transport in nanostructures: From computational concepts to spintronics in graphene and magnetic tunnel junctions*, volume 1. 2008. (cit. on p. 26)

[150] C Naud. Quantum transport in nanostructures. *Annales De Physique*, 27(5):1–135,137–140, aug 2002. (cit. on p. 26)

[151] Supriyo Datta. *Quantum transport: Atom to transistor*, volume 9780521631. Cambridge University Press, jan 2005. (cit. on p. 26)

[152] Aldo Di Carlo, Marieta Gheorghe, Alessandro Bolognesi, Paolo Lugli, Michael Sternberg, Gotthard Seifert, and Thomas Frauenheim. Molecular Devices Simulations Based on Density Functional Tight-Binding. *Journal of Computational Electronics*, 1(1-2):109–112, jul 2002. (cit. on p. 26)

[153] Mads Brandbyge, José Luis Mozos, Pablo Ordejón, Jeremy Taylor, and Kurt Stokbro. Density-functional method for nonequilibrium electron transport. *Physical Review B - Condensed Matter and Materials Physics*, 65(16):1654011–16540117, apr 2002. (cit. on pp. 26 and 77)

[154] Nick Papior, Nicolás Lorente, Thomas Frederiksen, Alberto García, and Mads Brandbyge. Improvements on non-equilibrium and transport Green function techniques: The next-generation TRANSIESTA. *Computer Physics Communications*, 212:8–24, mar 2017. (cit. on pp. 26 and 77)

[155] M. P. Lopez Sancho, J. M. Lopez Sancho, and J Rubio. Quick iterative scheme for the calculation of transfer matrices: Application to Mo (100). *Journal of Physics F: Metal Physics*, 14(5):1205–1215, 1984. (cit. on p. 29)

[156] M. P. Lopez Sancho, J. M. Lopez Sancho, and J Rubio. Highly convergent schemes for the calculation of bulk and surface Green functions. *Journal of Physics F: Metal Physics*, 15(4):851–858, 1985. (cit. on p. 29)

[157] D. H. Lee and J. D. Joannopoulos. Simple scheme for surface-band calculations. II. the Green's function. *Physical Review B*, 23(10):4997–5004, may 1981. (cit. on p. 29)

[158] D. H. Lee and J. D. Joannopoulos. Simple scheme for surface-band calculations. I. *Physical Review B*, 23(10):4988–4996, may 1981. (cit. on p. 29)

[159] Daniel S. Fisher and Patrick A. Lee. Relation between conductivity and transmission matrix, jun 1981. (cit. on p. 32)

[160] S. B. Zhang and John E. Northrup. Chemical potential dependence of defect formation energies in GaAs: Application to Ga self-diffusion. *Physical Review Letters*, 67(17):2339–2342, oct 1991. (cit. on p. 34)

[161] Karsten Reuter and Matthias Scheffler. Composition, structure, and stability of (formula presented) as a function of oxygen pressure. *Physical Review B - Condensed Matter and Materials Physics*, 65(3):1–11, dec 2002. (cit. on p. 34)

[162] Chris G. Van De Walle and Jörg Neugebauer. First-principles calculations for defects and impurities: Applications to III-nitrides, apr 2004. (cit. on p. 34)

[163] Christoph Freysoldt, Blazej Grabowski, Tilmann Hickel, Jörg Neugebauer, Georg Kresse, Anderson Janotti, and Chris G. Van De Walle. First-principles calculations for point defects in solids. *Reviews of Modern Physics*, 86(1):253–305, mar 2014. (cit. on p. 34)

[164] Hannu-Pekka Komsa and Arkady V Krasheninnikov. Native defects in bulk and monolayer MoS 2 from first principles. *Physical Review B*, 91(125304), 2015. (cit. on pp. 34, 35, 40, 41, 44, 45, 46, 58, 61, 63, 69, 77, and 81)

[165] M Chase. NIST-JANAF Thermochemical Tables, 4th Edition, 1998. (cit. on p. 34)

[166] Mohammad Bahmani, Mahdi Faghihnasiri, Michael Lorke, Agnieszka Beata Kuc, and Thomas Frauenheim. Electronic Properties of Defective MoS2 Monolayers Subject to Mechanical Deformations: A First-Principles Approach. *Physica Status Solidi (B) Basic Research*, page 1900541, mar 2020. (cit. on pp. 37, 58, 59, 63, 66, 69, 75, 81, and 82)

[167] Sheneve Z. Butler, Shawna M. Hollen, Linyou Cao, Yi Cui, Jay A. Gupta, Humberto R. Gutiérrez, Tony F. Heinz, Seung Sae Hong, Jiaxing Huang, Ariel F. Ismach, Ezekiel Johnston-Halperin, Masaru Kuno, Vladimir V. Plashnitsa, Richard D. Robinson, Rodney S. Ruoff, Sayeef Salahuddin, Jie Shan, Li Shi, Michael G. Spencer, Mauricio Terrones, Wolfgang Windl, and Joshua E.

Goldberger. Progress, Challenges, and Opportunities in Two-Dimensional Materials Beyond Graphene. *ACS Nano*, 7(4):2898–2926, apr 2013. (cit. on pp. 37 and 58)

[168] Sumanta Bhandary, Gabriele Penazzi, Jonas Fransson, Thomas Frauenheim, Olle Eriksson, and Biplab Sanyal. Controlling Electronic Structure and Transport Properties of Zigzag Graphene Nanoribbons by Edge Functionalization with Fluorine. *The Journal of Physical Chemistry C*, 119(36):21227–21233, sep 2015. (cit. on p. 37)

[169] Deep Jariwala, Vinod K Sangwan, Lincoln J Lauhon, Tobin J Marks, and Mark C Hersam. Emerging device applications for semiconducting two-dimensional transition metal dichalcogenides, 2014. (cit. on p. 37)

[170] Xiaonian Yang, Qiang Li, Guofeng Hu, Zegao Wang, Zhenyu Yang, Xingqiang Liu, Mingdong Dong, and Caofeng Pan. Controlled synthesis of high-quality crystals of monolayer MoS2 for nanoelectronic device application. *Science China Materials*, 59(3):182–190, mar 2016. (cit. on pp. 37, 75, and 80)

[171] Shengjun Yuan, Rafael Roldán, M. I. Katsnelson, and Francisco Guinea. Effect of point defects on the optical and transport properties of MoS2 and WS2. *Physical Review B - Condensed Matter and Materials Physics*, 90(4):041402, jul 2014. (cit. on pp. 37 and 59)

[172] Geun Ho Ahn, Matin Amani, Haider Rasool, Der-Hsien Lien, James P. Mastandrea, Joel W. Ager III, Madan Dubey, Daryl C. Chrzan, Andrew M. Minor, and Ali Javey. Strain-engineered growth of two-dimensional materials. *Nature Communications*, 8(1):608, dec 2017. (cit. on pp. 37, 49, 66, and 69)

[173] Christian Carmesin, Michael Lorke, Matthias Florian, Daniel Erben, Alexander Schulz, Tim O. Wehling, and Frank Jahnke. Quantum-Dot-Like States in Molybdenum Disulfide Nanostructures Due to the Interplay of Local Surface Wrinkling, Strain, and Dielectric Confinement. *Nano Letters*, 19(5):3182–3186, may 2019. (cit. on p. 37)

[174] Pablo Ordejon, Emilio Artacho, and Jose M. Soler. Selfconsistent order-N density-functional calculations for very large systems. *Physical Review B*, 53(16):R10441–R10444, apr 1996. (cit. on pp. 38, 59, and 76)

[175] N. Troullier and José Luriaas Martins. Efficient pseudopotentials for plane-wave calculations. *Physical Review B*, 43(3):1993–2006, jan 1991. (cit. on pp. 38, 60, and 76)

[176] N. Troullier and José Luriaas Martins. Efficient pseudopotentials for plane-wave calculations. II. Operators for fast iterative diagonalization. *Physical Review B*, 43(11):8861–8869, apr 1991. (cit. on pp. 38, 60, and 76)

[177] Won Seok Yun and J. D. Lee. Strain-induced magnetism in single-layer MoS2: Origin and manipulation. *Journal of Physical Chemistry C*, 119(5):2822–2827, feb 2015. (cit. on pp. 39 and 60)

[178] Sivan Refaely-Abramson, Diana Y Qiu, Steven G Louie, and Jeffrey B Neaton. Defect-Induced Modification of Low-Lying Excitons and Valley Selectivity in Monolayer Transition Metal Dichalcogenides. *Physical Review Letters*, 121(16), 2018. (cit. on pp. 39, 46, 60, 61, and 78)

[179] Mit H. Naik and Manish Jain. Substrate screening effects on the quasiparticle band gap and defect charge transition levels in MoS2. *Physical Review Materials*, 2(8):084002, aug 2018. (cit. on pp. 39, 46, 47, 60, 61, and 78)

[180] Bruno Schuler, Diana Y. Qiu, Sivan Refaely-Abramson, Christoph Kastl, Christopher T. Chen, Sara Barja, Roland J. Koch, D. Frank Ogletree, Shaul Aloni, Adam M. Schwartzberg, Jeffrey B. Neaton, Steven G. Louie, and Alexander Weber-Bargioni. Large Spin-Orbit Splitting of Deep In-Gap Defect States of Engineered Sulfur Vacancies in Monolayer WS2. *Physical Review Letters*, 123(7):076801, aug 2019. (cit. on pp. 39, 46, 60, 61, and 78)

[181] J. A. Wilson and A. D. Yoffe. The transition metal dichalcogenides discussion and interpretation of the observed optical, electrical and structural properties. *Advances in Physics*, 18(73):193–335, 1969. (cit. on p. 40)

[182] L. F. Mattheiss. Band structures of transition-metal-dichalcogenide layer compounds. *Physical Review B*, 8(8):3719–3740, oct 1973. (cit. on p. 40)

[183] Priya Johari and Vivek B. Shenoy. Tunable dielectric properties of transition metal dichalcogenides. In *ACS Nano*, volume 5, pages 5903–5908. American Chemical Society, jul 2011. (cit. on p. 40)

[184] Agnieszka Kuc, Nourdine Zibouche, and Thomas Heine. How does quantum confinement influence the electronic structure of transition metal sulfides TmS2. *Physical Review B*, 83(24):245213, jun 2011. (cit. on pp. 40 and 41)

[185] Ashok Kumar and P. K. Ahluwalia. A first principle Comparative study of electronic and optical properties of 1H - MoS2and 2H - MoS2. *Materials Chemistry and Physics*, 135(2-3):755–761, aug 2012. (cit. on pp. 40 and 41)

[186] Nourdine Zibouche, Agnieszka Kuc, Janice Musfeldt, and Thomas Heine. Transition-metal dichalcogenides for spintronic applications. *Annalen der Physik*, 526(9-10):395–401, oct 2014. (cit. on pp. 40 and 41)

[187] E. Cappelluti, R. Roldán, J. A. Silva-Guillén, P. Ordejón, and F. Guinea. Tight-binding model and direct-gap/indirect-gap transition in single-layer and multilayer MoS2. *Physical Review B - Condensed Matter and Materials Physics*, 88(7):075409, aug 2013. (cit. on pp. 41 and 64)

[188] C González, B Biel, and Y J Dappe. Theoretical characterisation of point defects on a MoS 2 monolayer by scanning tunnelling microscopy. *Nanotechnology*, 27(10):105702, mar 2016. (cit. on pp. 41, 45, 48, 64, and 69)

[189] A. Steinhoff, M. Rösner, F. Jahnke, T. O. Wehling, and C. Gies. Influence of excited carriers on the optical and electronic properties of MoS2. *Nano Letters*, 14(7):3743–3748, jul 2014. (cit. on p. 41)

[190] Priya Johari and Vivek B. Shenoy. Tuning the electronic properties of semiconducting transition metal dichalcogenides by applying mechanical strains. *ACS Nano*, 6(6):5449–5456, jun 2012. (cit. on p. 42)

[191] Santosh Kc, Roberto C Longo, Rafik Addou, Robert M Wallace, and Kyeongjae Cho. Impact of intrinsic atomic defects on the electronic structure of MoS2monolayers. *Nanotechnology*, 25(37):375703, sep 2014. (cit. on p. 44)

[192] Michael G. Stanford, Yu-Chuan Lin, Maria Gabriela Sales, Anna N. Hoffman, Christopher T. Nelson, Kai Xiao, Stephen McDonnell, and Philip D. Rack. Lithographically patterned metallic conduction in single-layer MoS2 via plasma processing. *npj 2D Materials and Applications*, 3(1):13, dec 2019. (cit. on pp. 44, 61, 63, and 80)

[193] Mehmet Gokhan Sensoy, Dmitry Vinichenko, Wei Chen, Cynthia M Friend, and Efthimios Kaxiras. Strain effects on the behavior of isolated and paired sulfur vacancy defects in monolayer MoS2. *Physical Review B*, 95, 2017. (cit. on pp. 45, 66, and 69)

[194] Mohnish Pandey, Filip A. Rasmussen, Korina Kuhar, Thomas Olsen, Karsten W. Jacobsen, and Kristian S. Thygesen. Defect-Tolerant Monolayer Transition Metal Dichalcogenides. *Nano Letters*, 16(4):2234–2239, apr 2016. (cit. on pp. 47, 58, 63, 64, 75, and 82)

[195] Jinhua Hong, Zhixin Hu, Matt Probert, Kun Li, Danhui Lv, Xinan Yang, Lin Gu, Nannan Mao, Qingliang Feng, Liming Xie, Jin Zhang, Dianzhong Wu, Zhiyong Zhang, Chuanhong Jin, Wei Ji, Xixiang Zhang, Jun Yuan, and Ze Zhang. Exploring atomic defects in molybdenum disulphide monolayers. *Nature Communications*, 6(1):6293, may 2015. (cit. on pp. 47 and 86)

[196] Francesco Tumino, Carlo Spartaco Casari, Andrea Li Bassi, and Sergio Tosoni. Nature of Point Defects in Single-Layer MoS2Supported on Au(111). *Journal of Physical Chemistry C*, 124(23):12424–12431, jun 2020. (cit. on p. 48)

[197] Pranjal Kumar Gogoi, Zhenliang Hu, Qixing Wang, Alexandra Carvalho, Daniel Schmidt, Xinmao Yin, Yung Huang Chang, Lain Jong Li, Chorng Haur Sow, A. H.Castro Neto, Mark B.H. Breese, Andrivo Rusydi, and Andrew T.S.

Wee. Oxygen Passivation Mediated Tunability of Trion and Excitons in MoS2. *Physical Review Letters*, 119(7):077402, aug 2017. (cit. on p. 52)

[198] Xiaoyan Zhang, Saifeng Zhang, Yafeng Xie, Jiawei Huang, Lei Wang, Yun Cui, and Jun Wang. Tailoring the nonlinear optical performance of two-dimensional MoS2 nanofilms: Via defect engineering. *Nanoscale*, 10(37):17924–17932, sep 2018. (cit. on p. 52)

[199] Mohammad Bahmani, Michael Lorke, Mahdi Faghihnasiri, and Thomas Frauenheim. Reversibly Tuning the Optical Properties of Defective Transition-Metal Dichalcogenide Monolayers. *Physica Status Solidi (B) Basic Research*, 258(12):2000524, oct 2021. (cit. on p. 58)

[200] A. Steinhoff, J. H. Kim, F. Jahnke, M. Rösner, D. S. Kim, C. Lee, G. H. Han, M. S. Jeong, T. O. Wehling, and C. Gies. Efficient Excitonic Photoluminescence in Direct and Indirect Band Gap Monolayer MoS2. *Nano Letters*, 15(10):6841–6847, oct 2015. (cit. on p. 58)

[201] Riccardo Frisenda, Matthias Drüppel, Robert Schmidt, Steffen Michaelis De Vasconcellos, David Perez De Lara, Rudolf Bratschitsch, Michael Rohlfing, and Andres Castellanos-Gomez. Biaxial strain tuning of the optical properties of single-layer transition metal dichalcogenides. *npj 2D Materials and Applications*, 1(10), 2017. (cit. on p. 58)

[202] Oriol Lopez-Sanchez, Dominik Lembke, Metin Kayci, Aleksandra Radenovic, and Andras Kis. Ultrasensitive photodetectors based on monolayer MoS2. *Nature Nanotechnology*, 8(7):497–501, jul 2013. (cit. on p. 58)

[203] F. Withers, O. Del Pozo-Zamudio, A. Mishchenko, A. P. Rooney, A. Gholinia, K. Watanabe, T. Taniguchi, S. J. Haigh, A. K. Geim, A. I. Tartakovskii, and K. S. Novoselov. Light-emitting diodes by band-structure engineering in van der Waals heterostructures. *Nature Materials*, 14(3):301–306, mar 2015. (cit. on pp. 58 and 59)

[204] M. A. Khan, Mikhail Erementchouk, Joshua Hendrickson, and Michael N. Leuenberger. Electronic and optical properties of vacancy defects in single-layer transition metal dichalcogenides. *Physical Review B*, 95(24):245435, jun 2017. (cit. on p. 58)

[205] Soumyajyoti Haldar, Hakkim Vovusha, Manoj Kumar Yadav, Olle Eriksson, and Biplab Sanyal. A systematic study of structural, electronic and optical properties of atomic scale defects in 2D transition metal dichalcogenides $MX_2$ (M = Mo,W; X = S, Se, Te). *Physical Review B*, 92(23):235408, dec 2015. (cit. on pp. 58 and 63)

[206] Haiyan Nan, Zilu Wang, Wenhui Wang, Zheng Liang, Yan Lu, Qian Chen, Daowei He, Pingheng Tan, Feng Miao, Xinran Wang, Jinlan Wang, and Zhenhua Ni. Strong photoluminescence enhancement of MoS2 through defect engineering and oxygen bonding. *ACS Nano*, 8(6):5738–5745, jun 2014. (cit. on p. 59)

[207] Sanfeng Wu, Sonia Buckley, John R. Schaibley, Liefeng Feng, Jiaqiang Yan, David G. Mandrus, Fariba Hatami, Wang Yao, Jelena Vučković, Arka Majumdar, and Xiaodong Xu. Monolayer semiconductor nanocavity lasers with ultralow thresholds. *Nature*, 520(7545):69–72, apr 2015. (cit. on p. 59)

[208] M Koperski, K Nogajewski, A Arora, V Cherkez, P Mallet, J. Y. Veuillen, J Marcus, P Kossacki, and M Potemski. Single photon emitters in exfoliated WSe2 structures. *Nature Nanotechnology*, 10(6):503–506, 2015. (cit. on p. 59)

[209] Laxmi Narayan Tripathi, Oliver Iff, Simon Betzold, Łukasz Dusanowski, Monika Emmerling, Kihwan Moon, Young Jin Lee, Soon Hong Kwon, Sven Höfling, and Christian Schneider. Spontaneous Emission Enhancement in Strain-Induced WSe2 Monolayer-Based Quantum Light Sources on Metallic Surfaces. *ACS Photonics*, 5(5):1919–1926, may 2018. (cit. on p. 59)

[210] Néstor Perea-López, Zhong Lin, Nihar R Pradhan, Agustín Iñiguez-Rábago, Ana Laura Elías, Amber McCreary, Jun Lou, Pulickel M Ajayan, Humberto

Terrones, Luis Balicas, and Mauricio Terrones. CVD-grown monolayered MoS2 as an effective photosensor operating at low-voltage. *2D Materials*, 1(1):011004, apr 2014. (cit. on p. 59)

[211] Ursula Wurstbauer, Bastian Miller, Eric Parzinger, and Alexander W. Holleitner. Light-matter interaction in transition metal dichalcogenides and their heterostructures, 2017. (cit. on p. 59)

[212] Peng Tao, Huaihong Guo, Teng Yang, and Zhidong Zhang. Strain-induced magnetism in MoS2 monolayer with defects. *Journal of Applied Physics*, 1151(10):44311–173105, feb 2014. (cit. on p. 60)

[213] Huiling Zheng, Baishun Yang, Dingdi Wang, Ruilin Han, Xiaobo Du, and Yu Yan. Tuning magnetism of monolayer MoS 2 by doping vacancy and applying strain Strain-induced magnetism in MoS 2 monolayer with defects Tuning magnetism of monolayer MoS 2 by doping vacancy and applying strain. *Applied Physics Letters*, 1041(10):132403–44311, mar 2014. (cit. on p. 60)

[214] Aolin Li, Jiangling Pan, Zhixiong Yang, Lin Zhou, Xiang Xiong, and Fangping Ouyang. Charge and strain induced magnetism in monolayer MoS2 with S vacancy. *Journal of Magnetism and Magnetic Materials*, 451:520–525, apr 2018. (cit. on p. 60)

[215] William Humphrey, Andrew Dalke, and Klaus Schulten. VMD – Visual Molecular Dynamics. *Journal of Molecular Graphics*, 14:33–38, 1996. (cit. on p. 61)

[216] Peter Y. Yu, Manuel Cardona, Peter Y. Yu, and Manuel Cardona. Introduction. In *Fundamentals of Semiconductors*, pages 1–11. Springer, Berlin, Heidelberg, 2013. (cit. on p. 62)

[217] K. Barthelmi, J. Klein, A. Hötger, L. Sigl, F. Sigger, E. Mitterreiter, S. Rey, S. Gyger, M. Lorke, M. Florian, F. Jahnke, T. Taniguchi, K. Watanabe, V. Zwiller, K. D. Jöns, U. Wurstbauer, C. Kastl, A. Weber-Bargioni, J. J. Finley, K. Müller, and A. W. Holleitner. Atomistic defects as single-photon emitters in atomically thin MoS2, aug 2020. (cit. on pp. 62 and 75)

[218] Elmar Mitterreiter, Bruno Schuler, Katja Barthelmi, Katherine Cochrane, Jonas Kiemle, Florian Sigger, Julian Klein, Ed Wong, Edward Barnard, Sivan Refaely-Abramson, Diana Qiu, Michael Lorke, Frank Jahnke, Jonathan Finley, T U Muenchen, and Adam Schwartzberg. The role of chalcogen vacancies for atomic defect emission in MoS2. nov 2020. (cit. on pp. 62 and 75)

[219] Mohammad Bahmani, Mahdi Ghorbani-Asl, and Thomas Frauenheim. Effect of interfacial defects on the electronic properties of MoS 2 based lateral TH heterophase junctions. *RSC Advances*, 11(60):37995–38002, nov 2021. (cit. on p. 74)

[220] O. Ávalos-Ovando, D. Mastrogiuseppe, and S. E. Ulloa. Lateral heterostructures and one-dimensional interfaces in 2D transition metal dichalcogenides, mar 2019. (cit. on p. 74)

[221] Jianwei Wang, Zhiqiang Li, Haiyuan Chen, Guangwei Deng, and Xiaobin Niu. Recent Advances in 2D Lateral Heterostructures, dec 2019. (cit. on p. 74)

[222] Michel Houssa, Ruishen Meng, Valery Afanas'ev, and André Stesmans. First-principles study of the contact resistance at 2D metal/2D semiconductor heterojunctions, apr 2020. (cit. on p. 74)

[223] Manish Chhowalla, Hyeon Suk Shin, Goki Eda, Lain Jong Li, Kian Ping Loh, and Hua Zhang. The chemistry of two-dimensional layered transition metal dichalcogenide nanosheets, apr 2013. (cit. on p. 74)

[224] D. Marian, E. Dib, T. Cusati, A. Fortunelli, G. Iannaccone, and G. Fiori. Two-dimensional transistors based on MoS2 lateral heterostructures. In *Technical Digest - International Electron Devices Meeting, IEDM*, pages 14.1.1–14.1.4. IEEE, dec 2017. (cit. on pp. 74 and 77)

[225] Jiahao Kang, Wei Liu, Deblina Sarkar, Debdeep Jena, and Kaustav Banerjee. Computational study of metal contacts to monolayer transition-metal dichalcogenide semiconductors, jul 2014. (cit. on pp. 74 and 75)

[226] M. Luisier, A. Szabo, C. Stieger, C. Klinkert, S. Bruck, A. Jain, and L. Novotny. First-principles simulations of 2-D semiconductor devices: Mobility, I-V characteristics, and contact resistance. In *Technical Digest - International Electron Devices Meeting, IEDM*, pages 5.4.1–5.4.4. Institute of Electrical and Electronics Engineers Inc., jan 2017. (cit. on p. 74)

[227] Daniel S. Schulman, Andrew J. Arnold, and Saptarshi Das. Contact engineering for 2D materials and devices, may 2018. (cit. on p. 74)

[228] Áron Szabó, Achint Jain, Markus Parzefall, Lukas Novotny, and Mathieu Luisier. Electron Transport through Metal/MoS2 Interfaces: Edge- or Area-Dependent Process? *Nano Letters*, 19(6):3641–3647, jun 2019. (cit. on p. 74)

[229] Suyeon Cho, Sera Kim, Jung Ho Kim, Jiong Zhao, Jinbong Seok, Dong Hoon Keum, Jaeyoon Baik, Duk Hyun Choe, K. J. Chang, Kazu Suenaga, Sung Wng Kim, Young Hee Lee, and Heejun Yang. Phase patterning for ohmic homojunction contact in MoTe2. *Science*, 349(6248):625–628, aug 2015. (cit. on p. 74)

[230] Zhi Qiang Fan, Xiang Wei Jiang, Jiezhi Chen, and Jun Wei Luo. Improving Performances of In-Plane Transition-Metal Dichalcogenide Schottky Barrier Field-Effect Transistors. *ACS Applied Materials and Interfaces*, 10(22):19271–19277, jun 2018. (cit. on p. 75)

[231] Xiang Zhang, Zehua Jin, Luqing Wang, Jordan A. Hachtel, Eduardo Villarreal, Zixing Wang, Teresa Ha, Yusuke Nakanishi, Chandra Sekhar Tiwary, Jiawei Lai, Liangliang Dong, Jihui Yang, Robert Vajtai, Emilie Ringe, Juan Carlos Idrobo, Boris I. Yakobson, Jun Lou, Vincent Gambin, Rachel Koltun, and Pulickel M. Ajayan. Low Contact Barrier in 2H/1T MoTe 2 In-Plane Heterostructure Synthesized by Chemical Vapor Deposition. *ACS Applied Materials and Interfaces*, 11(13):12777–12785, apr 2019. (cit. on p. 75)

[232] Adam L. Friedman, F. Keith Perkins, Aubrey T. Hanbicki, James C. Culbertson, and Paul M. Campbell. Dynamics of chemical vapor sensing with MoS

2 using 1T/2H phase contacts/channel. *Nanoscale*, 8(22):11445–11453, jun 2016. (cit. on p. 75)

[233] Damiano Marian, Elias Dib, Teresa Cusati, Enrique G. Marin, Alessandro Fortunelli, Giuseppe Iannaccone, and Gianluca Fiori. Transistor Concepts Based on Lateral Heterostructures of Metallic and Semiconducting Phases of MoS 2. *Physical Review Applied*, 8(5):054047, nov 2017. (cit. on p. 75)

[234] Yipeng An, Mengjun Zhang, Dapeng Wu, Zhaoming Fu, and Kun Wang. The electronic transport properties of transition-metal dichalcogenide lateral heterojunctions. *Journal of Materials Chemistry C*, 4(46):10962–10966, nov 2016. (cit. on p. 75)

[235] Mahdi Ghorbani-Asl, Andrey N Enyashin, Agnieszka Kuc, Gotthard Seifert, and Thomas Heine. Defect-induced conductivity anisotropy in MoS2 monolayers. *Physical Review B*, 8820, 2013. (cit. on pp. 75 and 82)

[236] Hannu-Pekka Komsa, Simon Kurasch, Ossi Lehtinen, Ute Kaiser, and Arkady V Krasheninnikov. From point to extended defects in two-dimensional MoS2 : Evolution of atomic structure under electron irradiation. *Physical Review B*, 88(035301), 2013. (cit. on pp. 75 and 81)

[237] Silvan Kretschmer, Hannu Pekka Komsa, Peter Bøggild, and Arkady V Krasheninnikov. Structural Transformations in Two-Dimensional Transition-Metal Dichalcogenide MoS2under an Electron Beam: Insights from First-Principles Calculations. *Journal of Physical Chemistry Letters*, 8(13):3061–3067, 2017. (cit. on p. 75)

[238] Jianqi Zhu, Zhichang Wang, Hua Yu, Na Li, Jing Zhang, JianLing Meng, Mengzhou Liao, Jing Zhao, Xiaobo Lu, Luojun Du, Rong Yang, Dongxia Shi, Ying Jiang, and Guangyu Zhang. Argon Plasma Induced Phase Transition in Monolayer MoS2. *Journal of the American Chemical Society*, 139(30):10216–10219, aug 2017. (cit. on p. 75)

[239] Kian Soon Yong, Diana M. Otalvaro, Ivan Duchemin, Mark Saeys, and Christian Joachim. Calculation of the conductance of a finite atomic line of sulfur vacancies created on a molybdenum disulfide surface. *Physical Review B - Condensed Matter and Materials Physics*, 77(20):205429, may 2008. (cit. on p. 76)

[240] Dipankar Saha and Santanu Mahapatra. Atomistic modeling of the metallic-to-semiconducting phase boundaries in monolayer MoS2. *Applied Physics Letters*, 108(25), jun 2016. (cit. on p. 77)

[241] Chithra H. Sharma, Ananthu P. Surendran, Abin Varghese, and Madhu Thalakulam. Stable and scalable 1T MoS2 with low temperature-coefficient of resistance. *Scientific Reports*, 8(1):12463, dec 2018. (cit. on p. 77)

[242] C. Ataca and S. Ciraci. Functionalization of Single-Layer MoS2 Honeycomb Structures. *The Journal of Physical Chemistry C*, 115(27):13303–13311, jul 2011. (cit. on p. 77)

[243] Mahdi Ghorbani-Asl, Paul D. Bristowe, and Krzysztof Koziol. A computational study of the quantum transport properties of a Cu-CNT composite. *Physical Chemistry Chemical Physics*, 17(28):18273–18277, jul 2015. (cit. on p. 80)

[244] Frederick Aryeetey, Tetyana Ignatova, and Shyam Aravamudhan. Quantification of defects engineered in single layer MoS2. *RSC Advances*, 10(39):22996–23001, jun 2020. (cit. on p. 81)

[245] Yipeng An, Yusheng Hou, Kun Wang, Shijing Gong, Chunlan Ma, Chuanxi Zhao, Tianxing Wang, Zhaoyong Jiao, Heyan Wang, and Ruqian Wu. Multifunctional Lateral Transition-Metal Disulfides Heterojunctions. *Advanced Functional Materials*, 30(32):2002939, aug 2020. (cit. on p. 85)

# Appendix A

# Defective $MoS_2$ Monolayers under strain

## A.1 $V_S$ vacancy

In Figs. A.1(a)–(d), studying the ML $MoS_2$ with $V_S$, we display the evolution of the band edges and DLs of a sulfur vacancy, $V_S$, under four types of strain. The black lines are band edges and the green dashed-line displays the Fermi level's position. The colored lines indicate the states DL1, DL2, and DL3. Here, we are only interested in the double-degenerate empty states close to the Fermi level. In the unstrained monolayer, DL2 and DL3 are mostly composed of $d_{xy}$ and $d_{x^2-y^2}$ orbitals of the neighboring molybdenums, respectively, as shown in Fig. A.2. Their degeneracy is lifted under uniaxial and shear T1 strains since the hexagonal symmetry is removed. Besides, isotropic biaxial strain does not split the degenerate levels and just move them closer to the CBM. The uniaxial strain in X-direction tunes DL2 more than DL3, but strain in Y-direction shifts DL3 more than DL2. In addition, shear T1 strain makes a mixture of contributions $d_{xy}$ and $d_{x^2-y^2}$ orbitals to DL2 and DL3. As shown in Figs. A.1(d),(e), shear T1 does not influence much the band edges though degeneracy splitting is noticeable. However, in all the cases, the position of the occupied shallow level stays almost unchanged. Fig. A.1(e) illustrates the amount of degenerate levels' separation in the same interval of strain for four

types of strains. Even a small quantity, around ±2%, of uniaxial or shear T1 strain enhances the level separation to around 60 or 110 meV, respectively. Further increasing the tensile shear T1 strain splits the levels up to almost 260 meV at +5%.

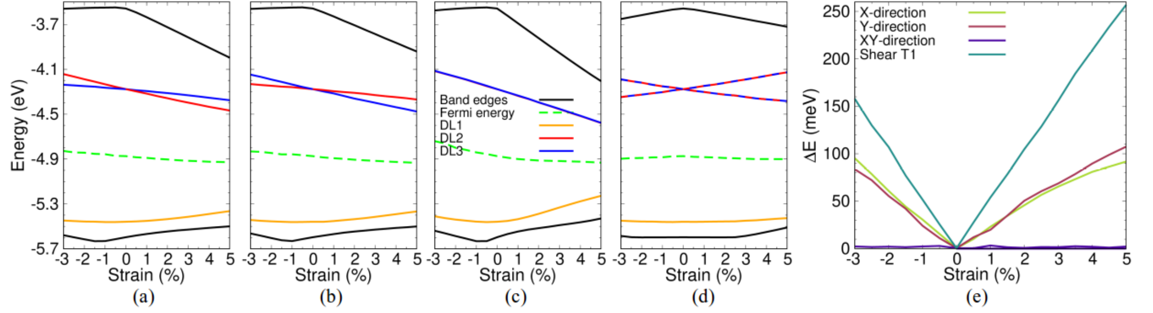


Figure A.1: (Color online) Evolution of the band edges along with the DLs of the $MoS_2$ ML with $V_S$ under strain in a) X-direction, b) Y-direction, c) XY-direction, and d) shear T1. The Fermi level and band edges are indicated with green dashed-line and black lines, respectively. The defect states, DL1–DL5, are shown with orange, red, blue, gray, and magenta line, respectively. e) The amount of degeneracy splitting of the deep DLs is plotted in the same interval for all four strains.

## A.2 Orbital Characteristics

### $V_S$ vacancy

Fig. A.2 displays the orbital characteristics of vacancy states for $V_S$ in ML $MoS_2$ as a function of strain along X-direction, Y-direction, and shear T1. In these images, blue and red orbitals, plotted at isosurface of 0.2 $\AA^{-3}$, corresponds to the lower and higher energy DLs at the zero strain, respectively. The orbitals' color of each band stay the same for all the strain cases except shear T1 which mixes the orbital components. Under uniaxial strain, the localized defect states are displayed with similar coloring. However, the defect levels are shown with cyan and magenta orbitals for compression and tensile shear T1 strains due to their orbital mixing.

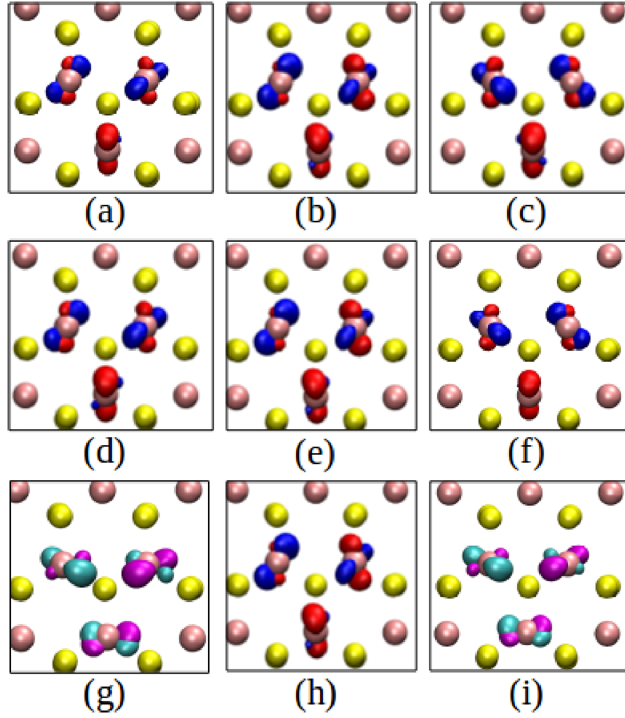


Figure A.2: (Color online) Orbital characteristics of unoccupied deep DLs of $V_S$ in ML $MoS_2$ at a) -3.0%, b) 0.0%, and c) +3.0% strain in X-direction, and d) -3.0%, e) 0.0%, and f) +3.0% strain in Y-direction, and g) -1.5%, h) 0.0%, and i) +1.0% shear T1 strain. The red and blue orbitals, plotted at isosurface of 0.2 $Å^{-3}$, are indicating the DLs at zero strain, respectively, which also label the localized states of the monolayers under strain in X- and Y-direction. In the case of shear T1 strain, DLs are displayed with cyan and magenta orbitals due to their orbital mixing.

### $V_{2S-top}$ vacancy

In Fig. A.3, we show the orbital characteristics of deep DLs close to the Fermi energy for $V_{2S-top}$ in ML $MoS_2$ as a function of strain along X-direction, Y-direction, and shear T1 strain. In these images, blue and red orbitals, plotted at isosurface of 0.2 $Å^{-3}$, corresponds to the lower and higher energy DLs at the zero strain, respectively. The orbitals' color of each band stay the same for all the strain cases except shear T1 which mixes the orbital components. Under uniaxial strain, the localized defect states are displayed with similar coloring. However, under compression and tensile shear T1 strains, the DLs are shown with cyan and magenta orbitals due to their orbital mixing.

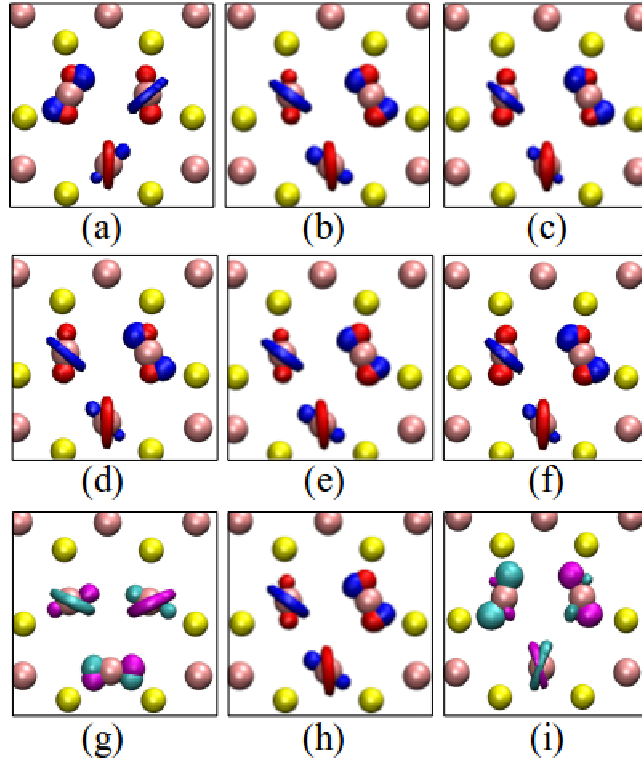


Figure A.3: (Color online) Orbital characteristics of unoccupied deep DLs of $V_{2S-top}$ in Ml $MoS_2$ at a) -3.0%, b) 0.0%, and c) +5.0% strain in X-direction, and d) -3.0%, e) 0.0%, and f) +3.0% strain in Y-direction, and g) -1.0%, h) 0.0%, and i) +1.0% shear T1 strain. The red and blue orbitals, plotted at isosurface of 0.2 $\AA^{-3}$, are indicating the DLs at zero strain, respectively, which also label the localized states of the monolayers under strain in X- and Y-direction. In the case of shear T1 strain, DLs are displayed with cyan and magenta orbitals.

### $V_{2S-par}$ vacancy

We display the orbital characteristics of $V_{2S-par}$ in ML $MoS_2$ for strain along X-direction, Y-direction, and shear T1 strain, as depicted in Fig. A.4. In these images, blue and red orbitals, plotted at isosurface of 0.2 $\AA^{-3}$, corresponds to the lower and higher energy DLs at the zero strain, respectively. The orbitals' color of each band stay the same for all the strain cases except shear T1 which mixes the orbital components. Under uniaxial strain, the localized defect states are displayed with similar coloring. However, under compression and tensile shear T1 strains, the DLs are shown with cyan and magenta orbitals due to their orbital mixing. strains.

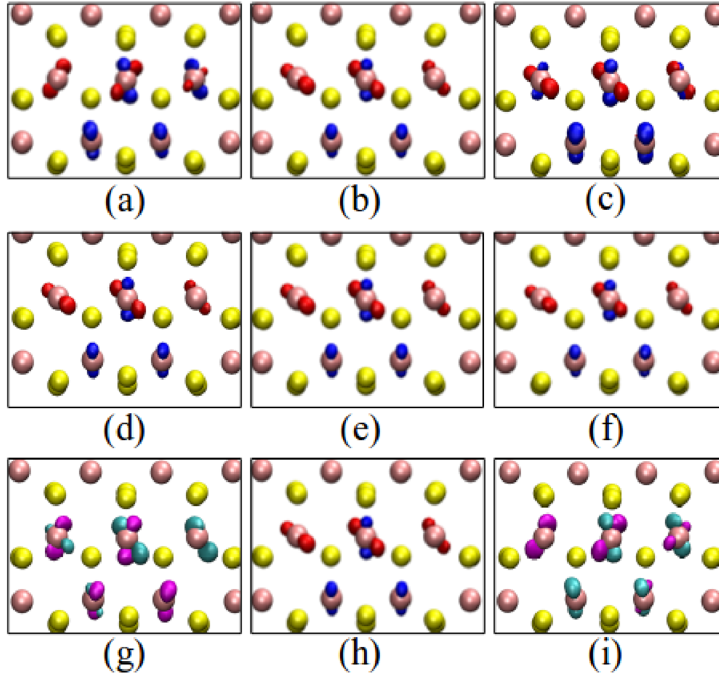


Figure A.4: (Color online) Orbital characteristics of unoccupied deep DLs of $V_{2S-par}$ in ML $MoS_2$ at a) +1.0%, b) 0.0%, and c) +3.0% strain in X-direction, and d) -1.5%, e) 0.0%, and f) +3.0% strain in Y-direction, and g) -1.0%, h) 0.0%, and i) +1.0% shear T1 strain. The red and blue orbitals, plotted at isosurface of 0.2 $\mathring{A}^{-3}$, are indicating the DLs at zero strain, respectively, which also label the localized states of the monolayers under strain in X- and Y-direction. In the case of shear T1 strain, DLs are displayed with cyan and magenta orbitals.

## $V_{Mo}$ vacancy

In Fig. A.5, we illustrate the orbital characteristics of deep DLs close to the Fermi energy for ML $MoS_2$ with $V_{Mo}$ as a function of strain along X-direction, Y-direction, and shear T1 strain. The orbitals are plotted at isosurface of 0.2 $\mathring{A}^{-3}$ and colored based on their energies, from the lowest to the highest, their color is blue, red, gray, orange, cyan, and magenta, respectively. These strains change the CBM, below which introduce an empty shallow DL. This band is constituted of $d_{x^2-y^2}$ and $d_{xy}$ in case of compression in X-direction and $d_{x^2-y^2}$, $d_{xy}$, and a small portion of $p_x$ for compression and tensile in Y-direction.

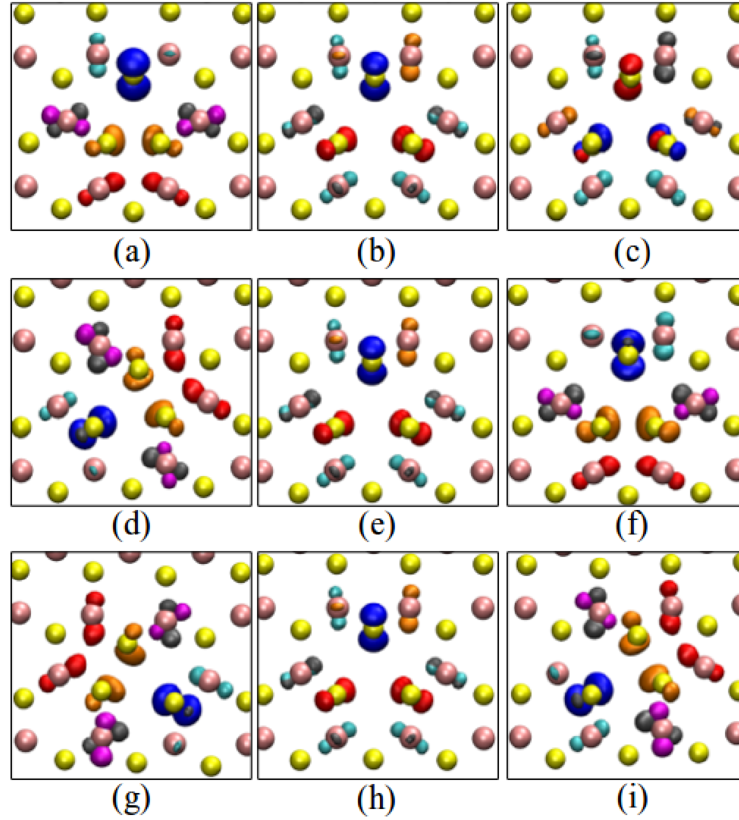


Figure A.5: (Color online) Orbital characteristics of unoccupied deep DLs of $V_{Mo}$ in ML $MoS_2$ at a) -1.0%, b) 0.0%, and c) +1.0% strain in X-direction, and d) -1.5%, e) 0.0%, and f) +2.0% strain in Y-direction, and g) -1.0%, h) 0.0%, and i) +1.0% shear T1 strain. The orbitals are plotted at isosurface of 0.2 $\mathring{A}^{-3}$ and colored based on their energies, from the lowest to the highest, their color is blue, red, gray, orange, cyan, and magenta, respectively.

## A.3 Geometry modifications for MLs $MoS_2$ with $V_{Mo}$

In Fig. A.6, we show the change in the position of the neighboring atoms around a Mo vacancy inside ML $MoS_2$, under different strains. The dramatic modification of the monolayers is depicted which leads to the breaking of the "$C_{3v}$" symmetry.

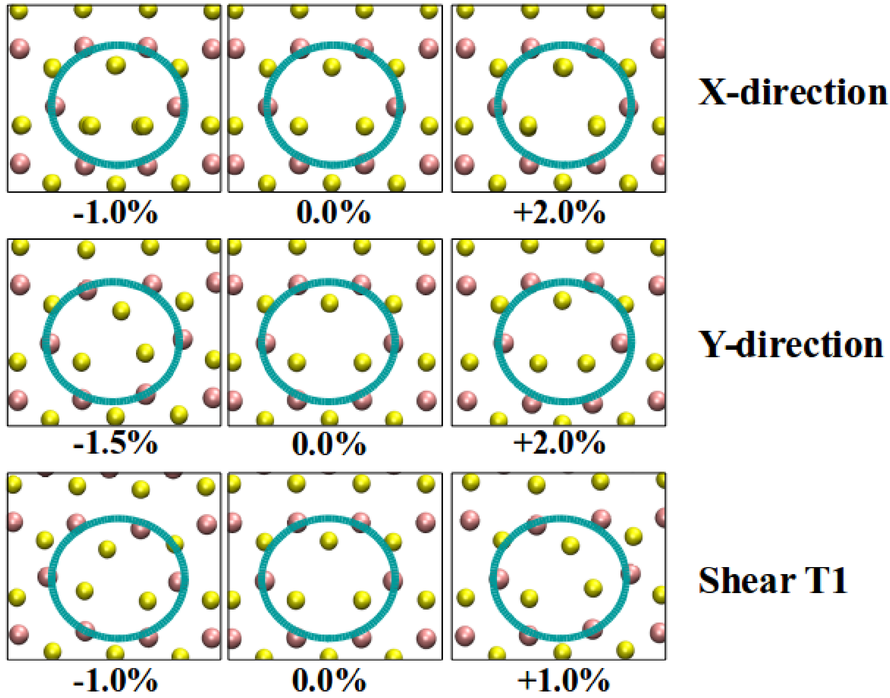


Figure A.6: (Color online) The change in the position of the atoms surrounding $V_{Mo}$ in ML $MoS_2$ at first row) -1.0%, 0.0%, +2.0% strain in X-direction, and second row) -1.5%, 0.0%, and +2.0% strain in Y-direction, and third row) -1.0%, 0.0%, and +1.0% shear T1 strain. The position of the vacancy and its neighboring sulfurs are highlighted with a cyan circle.

## A.4 $V_{Mo+3S}$ and $V_{Mo+6S}$ vacancies

The evolution of the band edges and localized DLs of $V_{Mo+3S}$ and $V_{Mo+6S}$ are demonstrated in Figs. A.7 and A.8, respectively. The black lines are band edges and the green dashed-line displays the Fermi levels position. The colored lines indicate the states DL1–DL8. As it can be seen, the change in geometry and hybridization of the orbital components result in the modification and mixing of the defect bands. However, it can still be observed that compressive and tensile uniaxial and biaxial strains shift the CBM but not the VBM. In both cases, shear T1 strain does not modify the band edges.

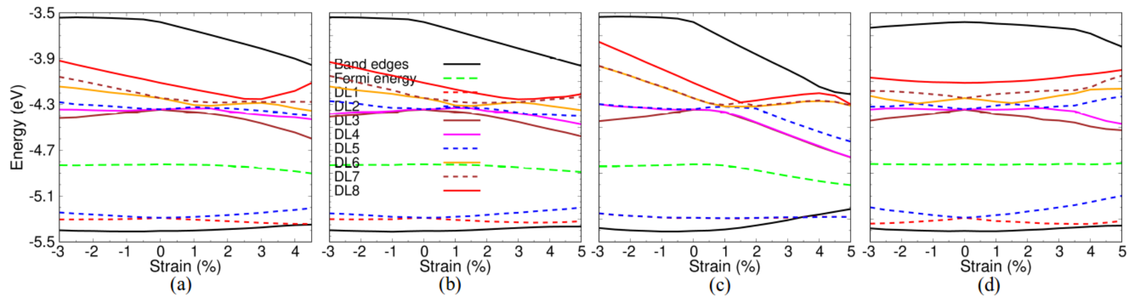


Figure A.7: (Color online) Evolution of the band edges along with the DLs of ML $MoS_2$ with $V_{Mo+3S}$ under strain in a) X-direction, b) Y-direction, c) XY-direction, and d) shear T1. In all the plots, Fermi level and band edges are indicated with green dashed-line and black lines, respectively. Other colored lines represent DLs.

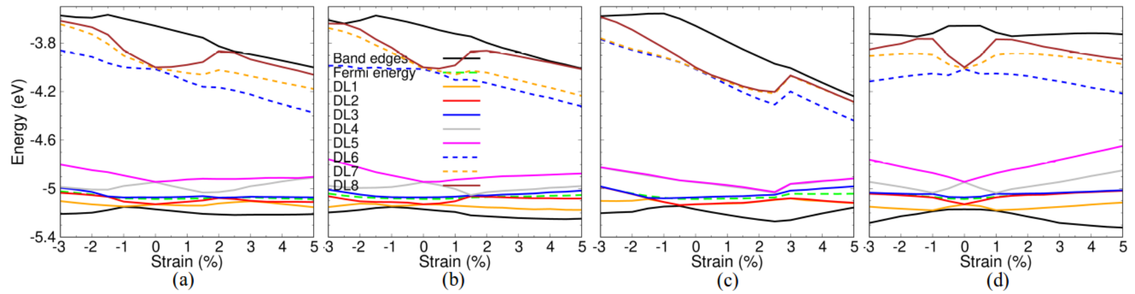


Figure A.8: (Color online) Evolution of the band edges along with the DLs of ML $MoS_2$ with $V_{Mo+6S}$ under strain in a) X-direction, b) Y-direction, c) XY-direction, and d) shear T1. In all the plots, Fermi level and band edges are indicated with green dashed-line and black lines, respectively. Other colored lines represent DLs.

## A.5 Input parameters for the self-generated pseudopotentials

The set of pseudopotentials used in these studies are self-generated by means of *"atom"* tool which is provided by SIESTA's developers along with the source code. The tool and an instruction of how to generate the pseudopotentials can be found under the *"/Util/Gen-basis/"* directory. Here are the input parameters which we used to produce:

**Pseudopotential for Mo:**

```
%define NEW_CC
   pe         Molybdenum
        tm2
```

```
   Mo   pbr
     0.000     0.000     0.000     0.000     0.000     0.000
    8    4
    5    0     1.000     0.000    #5s
    5    1     0.000     0.000    #5p
    4    2     5.000     0.000    #4d
    4    3     0.000     0.000    #4f
    2.50000   3.00000   1.40000   2.20000   0.00000   2.55000  Core corrs

#234567890123456789012345678901234567890123456789012345678901      Ruler
```

**Pseudopotential for S:**

```
%define NEW_CC
   pe    Sulphur
        tm2     2.08
    S   pbr
       0.00     0.00     0.00     0.00     0.00     0.00
    3    4
    3    0      2.00      0.00
    3    1      4.00      0.00
    3    2      0.00      0.00
    4    3      0.00      0.00
   1.78      1.94      2.29      2.29      0.00     1.51

#2345678901234567890123456789012345678901234567890      Ruler
```

# Appendix B

# 1T/2H $MoS_2$ Based Lateral Heterojunctions

## B.1 Structure of the devices containing point defects

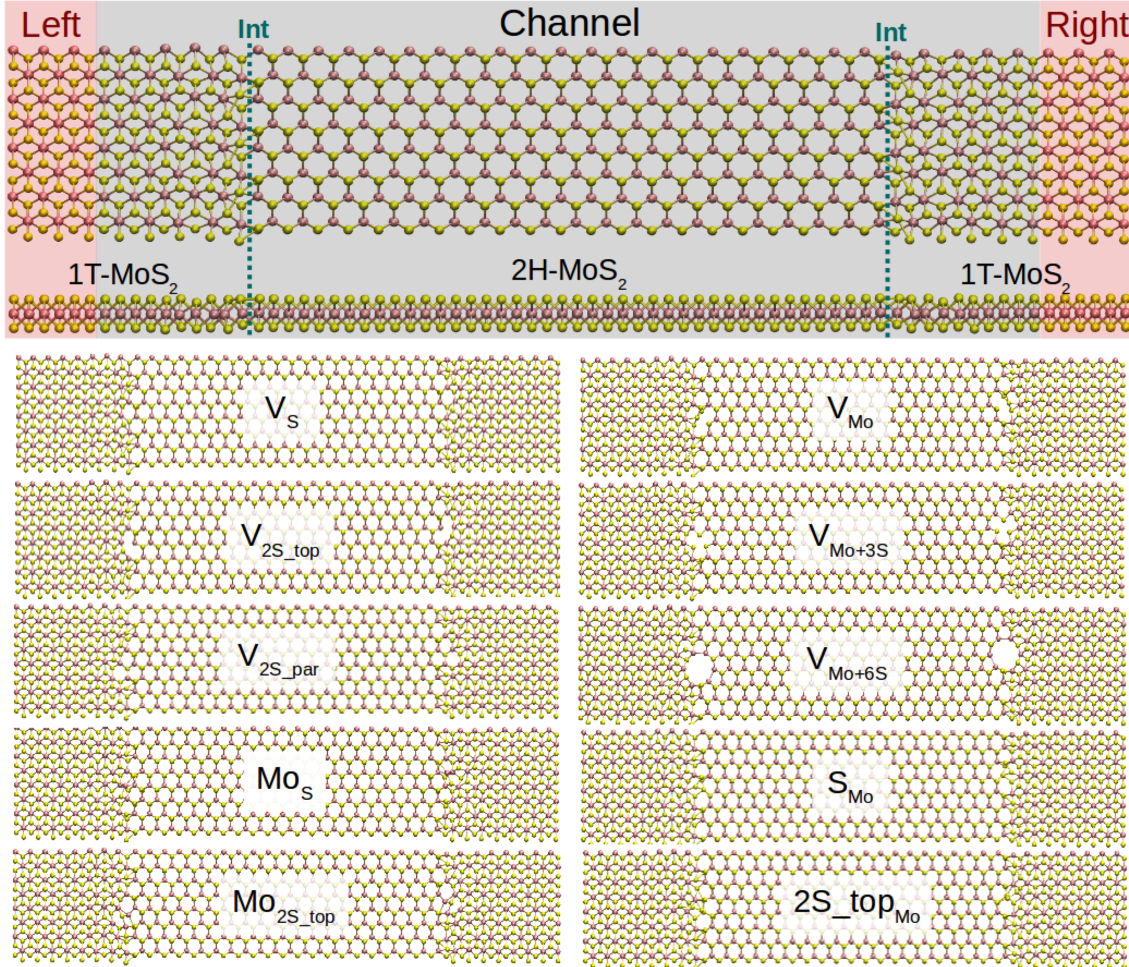


Figure B.1: **Top)** Schematic of the device based on metallic (1T) and Semiconductor (2H) phases of $MoS_2$ monolayers is shown. Electrodes (only 1T-$MoS_2$) and channel region (a combination of 1T- and 2H-$MoS_2$) are highlighted with shaded red and black, respectively. The interfaces are indicated with green dashed-lines. All the structures are considered periodic along the axis transverse to the transport direction. **Down)** Optimized defective structures with point defects at both interfaces of the devices.

## B.2 Vector Current - $V_{Mo}$

Shown in Fig. B.2, vector currents are plotted for perfect systems and devices with $V_{Mo}$ at both interfaces. Vector current displays the direction and the amount of current (size of the arrows) projected on each atom and at specific energy channel ($E_{ch}$), that comes from left (blue) or right (red) electrode. It can be clearly seen that the presence of the vacancy at the interfaces opens up further energy channels for the charge carriers to move.

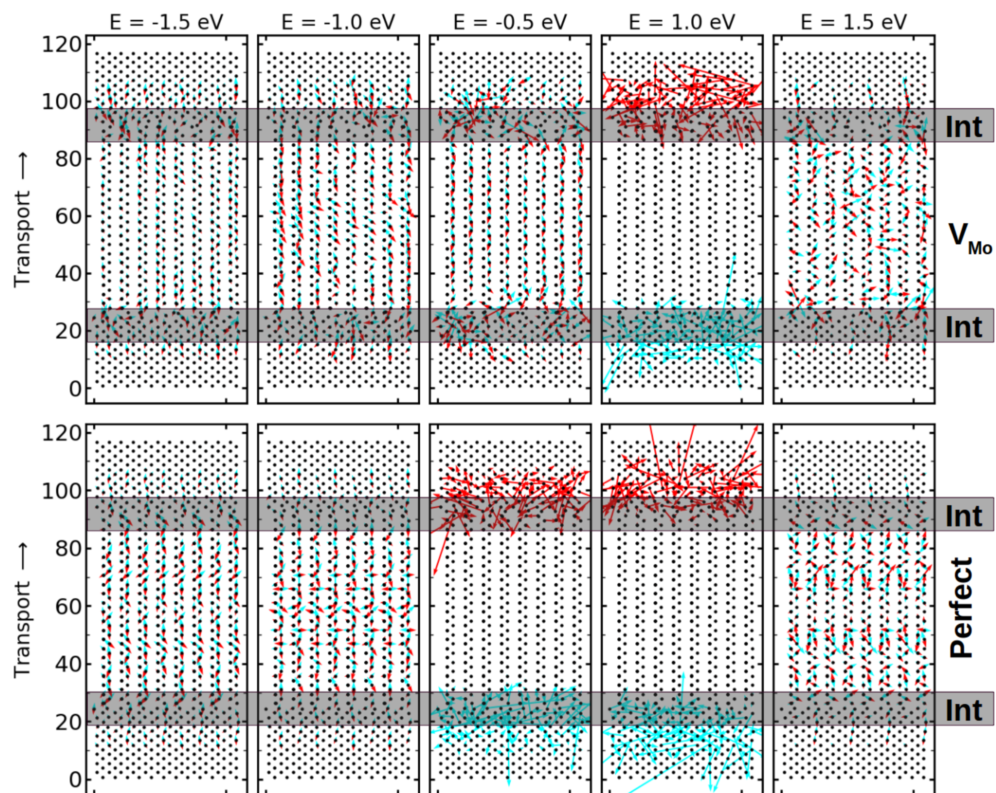


Figure B.2: (Color online) Vector currents are shown for devices with perfect interfaces and where molybdenum vacancy, $V_{Mo}$, are present at both interfaces. They are plotted at zero bias and specific energy channels, namely E= $-1.5$, $-1.0$, $-0.5$, $1.0$, $1.5eV$. Blue and red arrows display the current at each atom that comes from left and right electrode, respectively. The length of the arrow indicates the current magnitude. It can be clearly seen that the presence of the vacancy at the interfaces opens up further energy channels for the charge carriers to move.

## B.3 Local Density of States (LDOS) projected on atoms and orbitals

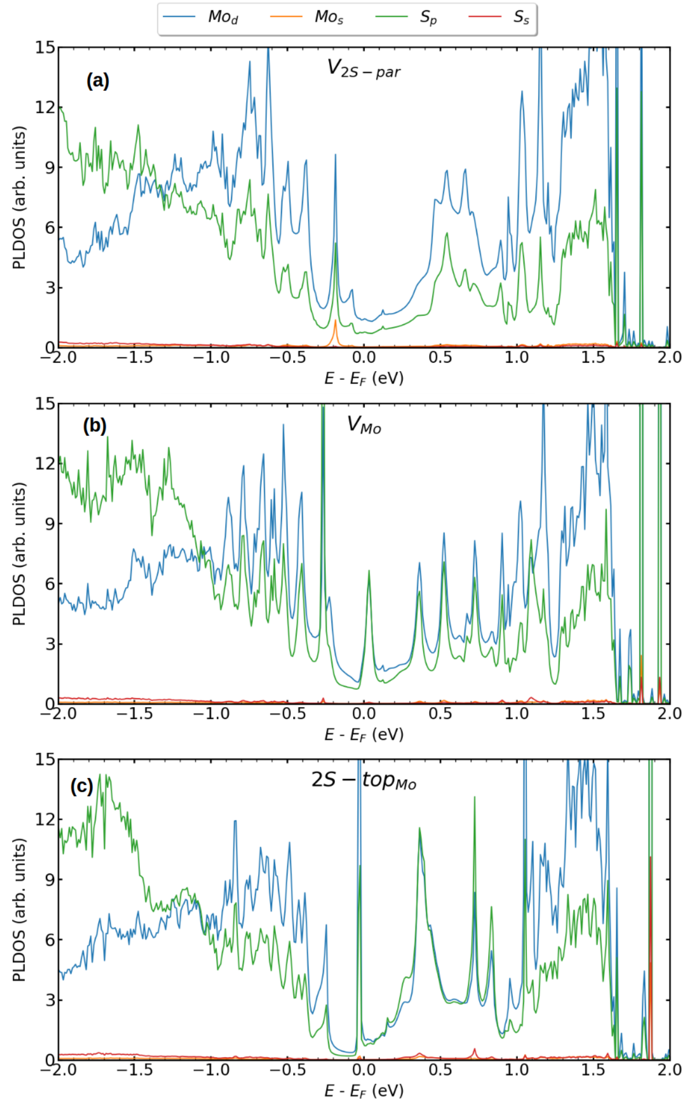


Figure B.3: (Color online) Density of states of the Molybdenum and Sulfur atoms at the left interface projected (LDOS) onto the orbitals contributing to the total DOS for devices containing **a)** $V_{2S-par}$, **b)** $V_{Mo}$, **c)** $2S - top_{Mo}$, at both interfaces. It clearly shows that the most contributions come from the $Mo_d$ and $S_p$ orbitals.

## B.4 Calculated BandGap vs. other methods

| Method | This paper | PBE-GGA[a] | HSE[b] | GW[b] |
|---|---|---|---|---|
| BandGap (eV) | 1.76 | 1.715 | 2.21 | 2.78 |

Table B.1: Band gaps of 2H-$MoS_2$ monolayer calculated at different levels of theory. a) Rafael Roldn, et. al Annalen der Physik 526(9-10), 347357 (2014), b. H.-P. Komsa and A. V. Krasheninnikov, Physical Review B,2015, 91, c. C. Ataca and S. Ciraci, The Journal of Physical Chemistry C, 2011, 115, 1330313311

## B.5 Projected Local Density of States (PLDOS)

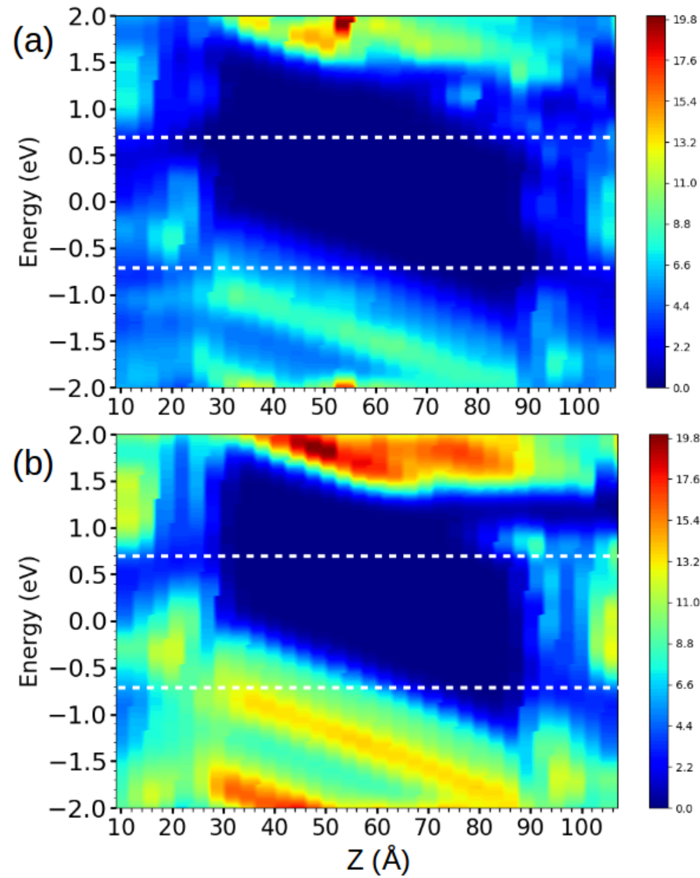


Figure B.4: (Color online) Projected local density of states (PLDOS) of devices based on T-H heterophase junction of $MoS_2$ monolayer under the biases with a) perfect interface and b) containing molybdenum vacancy. The white dotted lines indicate the bias window.